PNL-10764
UC-721

Tank Waste Treatment Science Task Quarterly Report for April - June 1995

J. P. LaFemina (Task Leader)

July 1995

Prepared for the U.S. Department of Energy
under Contract DE-AC06-76RLO 1830

Pacific Northwest Laboratory
Operated for the U.S. Department of Energy
by Battelle Memorial Institute

Battelle

PNL-10764

DISCLAIMER

PACIFIC NORTHWEST LABORATORY
operated by
BATTELLE MEMORIAL INSTITUTE
for the
UNITED STATES DEPARTMENT OF ENERGY
under Contract DE-AC06-76RLO 1830

PNL-10764
UC-721

Tank Waste Treatment Science Task Quarterly Report for April - June 1995

J. P. LaFemina (Task Leader)

D. L. Blanchard
P. J. Bruinsma
B. C. Bunker
I. E. Burgeson
Y. L. Chen
N. G. Colton
S. D. Conradson
J. Craig Hutton
A. R. Felmy
R. L. Gordon
N. G. Gotts
G. L. Graff
N. J. Hess
C. R. Hymas
M. M. Lamoureux
X. S. Li
J. Liu
G. J. Lumetta
J. R. Phillips
B. M. Rapko
D. R. Rector
J. R. Rustad
S. M. Sterner
P. A. Smith
L. Song
L. E. Thomas
J. M. Tingey
S. M. Tingey
L. Q. Wang
Y. Wang

July 1995

Prepared for
the U.S. Department of Energy
under Contract DE-AC06-76RLO 1830

Pacific Northwest Laboratory
Richland, Washington 99352

DISCLAIMER

Portions of this document may be illegible in electronic image products. Images are produced from the best available original document.

Summary

This report describes the work performed by the Pacific Northwest Laboratory (PNL) during the third quarter of FY 1995 under the Tank Waste Treatment Science Task of the Tank Waste Remediation System (TWRS) Pretreatment Technology Development Project. Work was performed in the following areas: 1) analytical methods development, 2) sludge dissolution modeling, 3) sludge characterization studies, 4) sludge component speciation, 5) pretreatment chemistry evaluation, and 6) colloidal studies for solid-liquid separations. Significant accomplishments during the third quarter are summarized below:

- Several features regarding the utility of the capillary ion analyzer for use in analysis of solutions derived from Hanford tank sludges were clarified during the third quarter.
  - The use of a combination of measurements, one with a chloride-based electrolyte and another with a chromate-based electrolyte, appears to allow detection and quantification of Br^-, Cl^-, SO_4^{2-}, NO_2^-, NO_3^-, F^-, PO_4^{3-}, and CO_3^{2-} in a multicomponent solution of inorganic anions.
  - Examination of detection limits as a function of the concentration of other species with similar retention values indicates that nitrate has an insignificant impact on the quantification of sulfate. Nitrite does have an impact on sulfate detection but only if the nitrite concentrations are appreciably larger than the sulfate concentrations.
  - In general, sub-ppm levels are detectable and quantifiable for most analytes in these multicomponent samples. However, routine, automated identification and analysis of multicomponent mixtures may not be possible with the capillary ion analyzer because of how the peaks shift as a function of the sample's concentration.
- Experimental data were used to fit parameters for the Environmental Simulation Program (ESP) electrolyte model. When revised parameters, fit from binary data on high ionic strength systems, are incorporated into the model, ESP accurately predicts the behavior of the $NaNO_3$-$NaNO_2$-H_2O, $NaNO_3$-NaOH-H_2O, $NaNO_2$-NaOH-H_2O, $NaNO_3$-NaOH-$Al(OH)_3$, $NaNO_2$-NaOH-$Al(OH)_3$, and $NaNO_3$-NaOH-$Cr(OH)_3$ mixed systems.
- Characterization and analysis of sludge samples from Tanks T-111, BX-107, T-104, S-104, and B-111, including washed samples and residual solids, was completed. The techniques used for analysis were transmission electron microscopy (TEM), scanning electron microscopy (SEM), and x-ray diffractometry (XRD). Results are consistent with elemental analysis data and tank history information and support the dissolution and sedimentation behavior that has been observed in particular tank sludges.
- Chromium and manganese x-ray absorption spectroscopy (XAS) spectra for eight tank samples (one untreated and one treated sample for each of Tanks B-111, S-104, T-104, and T-111) were collected at Stanford Synchrotron Radiation Laboratory (SSRL). Preliminary analysis of the XAS data for Cr indicates that for $BiPO_4$ wastes:

- Only Cr(VI) is soluble, and all Cr(VI) is soluble.

- Estimated amounts of soluble chromium, i.e., Cr(VI), are good (even conservative).

- Estimates of the amount of insoluble chromium that will leach are too high, possibly due to incorporation of Cr(III) in other "unleachable" phases typical of $BiPO_4$ wastes.

- If removal of Cr to $\leq$5000 ppm chromium in residual solids is necessary, the effectiveness of enhanced sludge washing is marginal due to poor leaching of Cr(III).

for REDOX wastes:

- All Cr(VI) is soluble.

- More Cr(VI) may be present than estimated.

- If most of the chromium is present as Cr(VI), enhanced sludge washing will remove more chromium than estimated.

- The absence of Cr(III) is unexpected, and may indicate that the core sample tested is not truly representative of REDOX tank wastes.

- Raman spectra of T-104 waste before and after treatment were collected. The spectra are being analyzed to determine the feasibility of using Raman spectroscopy for aluminum, phosphate, and sulfate speciation in tank waste solids.

- The results from a review of available salt cake data and the results from recent washing and leaching experiments were used to project wash and leach factors for aluminum, chromium, and phosphate in the single-shell tank waste inventory.

- The relationships among individual single-shell tank wastes and various waste groups, process streams, and chemical processing campaigns were established and pictorially summarized in order to determine how available experimental information for a limited number of tank wastes might translate into dissolution information for all wastes.

- A series of solutions, prepared using boehmite and colloidal silica as aluminum and silicon sources, have been characterized using x-ray and solid-state nuclear magnetic resonance (NMR) techniques. The results from this effort will serve to identify which aluminosilicate phases form as a function of solution compositions that might be encountered in waste processing and the conditions that could lead to cement formation during retrieval and pretreatment processing of wastes.

- Sedimentation models were developed to describe existing data. These models show promise for allowing engineers to predict both sedimentation rates and final sediment densities as a function of parameters, such as solids loading and the height of the sedimentation container.

- Studies were initiated on how processing parameters, such as heating and stirring, influence agglomeration and studies of agglomeration behavior in two-component particulate systems. These studies showed how the presence of one particle type can dramatically influence the physical properties of suspensions of another particle type by changing agglomeration behavior.

- Sedimentation results from studies performed with tank wastes were analyzed in terms of sedimentation concepts that have been developed by the Colloidal Studies subtask. In addition, sedimentation behavior of tank sludges was compared with the behavior of simple simulants.

- Existing equipment for colloidal characterization of actual tank waste samples has been identified, and a plan for the establishment of a Hot Colloids Laboratory has been developed.

Contents

Contents (contd)

Figures

Figures (contd)

Figures (contd)

Figures (contd)

Tables

1.0 Introduction

The Pretreatment Technology Development Project is one of seven Tank Waste Remediation System (TWRS) projects being conducted at the Pacific Northwest Laboratory (PNL)[a]. A key objective of this project and of the Tank Waste Treatment Science Task within it is to provide the technical basis and scientific understanding to support TWRS baseline decisions and actions; in particular, TPA Milestone M50-03, the 1998 sludge pretreatment decision regarding the level of pretreatment to be incorporated into the tank waste process flowsheets. Work performed by this task during the third quarter of FY 1995 is detailed in this report. Work for the first and second quarter is discussed in *Tank Waste Treatment Science Tasks Quarterly Report for October - December 1994,*[b] *January - March 1995.*[c] The work for this quarter includes:

Analytical Methods Development. To decrease analytical turnaround times; to increase sensitivity of the measurement; and/or to decrease waste volumes associated with obtaining analytical data for pretreatment technology development activities.

Sludge Dissolution Modeling. To provide key thermodynamic data to be used in process flowsheet development models and to provide a bounding case on dissolution reactions via direct experimental data on which tanks sludges will dissolve under specified processing conditions.

Sludge Characterization Studies. To identify the major solid phases in sludge; to determine how radionuclides are partitioned among the observed phases; to characterize the behavior of phases during processing; and to use the resulting database on sludge chemistry to help evaluate pretreatment technologies.

Sludge Component Speciation. To provide data on the chemical speciation of specific components in tank wastes that are important to developing pretreatment options. These data will allow the prediction of how different tank wastes will respond to different pretreatment processes, and will assist in the interpretation of existing pretreatment process chemistry data.

Pretreatment Chemistry Evaluation. To gather, evaluate, and integrate data on the characteristics of tank wastes that are relevant to the pretreatment end function.

Colloidal Studies for Solid-Liquid Separations. To determine how colloidal interactions in tank waste impact the major steps in tank waste processing; in particular, solid-liquid separations, as a function of waste processing conditions.

It is important to note that the scope of activities for the Tank Waste Treatment Science task encompasses all aspects of tank waste processing. It is also important to recognize that there are complementary efforts going on at Hanford and at other U.S. Department of Energy sites as part of the

---

(a) Operated for the U.S. Department of Energy by Battelle Memorial Institute under Contract DE-AC06-76RLO 1830.
(b) PNL-10762.
(c) PNL-10763.

Efficient Separations Processes Cross-Cutting Program and the Tanks Focus Area. To make the most efficient use of our resources, all possible effort is being made, and will continue to be made, to keep the lines of communication open among these activities so as to avoid duplication of effort and, most importantly, create a cooperative, synergistic environment for performing the required technical work.

2.0 Analytical Methods Development

Brian M. Rapko, Scott M. Tingey, Gregg J. Lumetta and Ingrid E. Burgeson

The purpose of this task is to purchase, install, and develop operational procedures for several analytical instruments. Table 2.1 summarizes the instruments to be installed and optimized during FY 1995. These instruments were selected for purposes of decreasing analytical turnaround times and/or increasing the sensitivity of the measurement and/or decreasing the waste volumes associated with obtaining analytical data from other sources. However, these new instruments, which in some cases introduce new analytical methods, require developmental work to 1) determine whether or not suitable performance can be obtained with the complex and unique matrices associated with the TWRS sludge pretreatment project and 2) to develop procedures (and identify the limitations in those procedures) for routine analyses with the complex and unique matrices. In the third quarter, work focused almost exclusively on the capillary ion analyzer.

2.1 Particle Size Analyzer

During the first quarter, National Institute of Science and Technology (NIST)-traceable standards, which covered the operating range (0.015 to 400 μm) were purchased and tested with the instrument. Good agreement between the standards and the instrument's measured values was found. During the second quarter, a procedure for operating the instrument was prepared. Testing the procedure with inexperienced users led to some refinements in the procedure, and the instrument appears ready for general research use. No additional work was performed during the third quarter on this project.

2.2 Capillary Ion Analyzer

During the first quarter, the instrument was installed and its anion separation and detection performance verified using the supplied 60-cm column with a standard solution that contained bromide, chloride, fluoride, phosphate, sulfate, nitrite, carbonate, and nitrate anions, each at a level of 1 to

Table 2.1. Analytical Instruments Associated with the Analytical Methods Development Subtask

Instrument	Analytical Function	Subtask Purpose
Capillary ion analyzer	Anion/cation analysis in dissolved Hanford tank pretreatment matrices	Installation assistance and method optimization
Gamma spectrometer	Identification and quantification of gamma-emitting radionuclides	Installation and method optimization
Particle size analyzer	Determination of particle sizes	Installation assistance and method optimization

2 ppm. With more complex matrices, designed to simulate the composition of actual tank waste-derived solutions, the separation proved unsatisfactory, with nitrate, nitrite, and sulfate being unresolved. By the end of the first quarter, a two-step approach seemed most likely to succeed. The first step would involve detection of all anions with the exception of sulfate, nitrate, and nitrite. The second step would involve a separate measurement under conditions designed to quantify at least two of those three anions, since the third could be determined by difference.

During the second quarter, a chloride-based electrolyte system, using ultraviolet (UV)-detection at 214 nm, was developed and tested by the instrument manufacturer, Waters/Millipore. This system seemed to give good detection and separation of nitrite and nitrate, with poor response for the other ions. However, when combined with the standard chromate-based system with UV-detection at 254 nm, a successful analysis of the simulated tank samples seemed possible. Consequently, a 214-nm lamp/filter assembly was purchased and installed.

A second approach was also initiated that involved the use of longer columns to increase resolution. If resolution of the anions is sufficiently increased, then the original chromate-based system could be maintained and all necessary analytical information obtained in a single run. The primary disadvantage of using longer columns is the increased run time required. However, as the run times for this capillary electrophoresis system were substantially shorter than for ion chromatography, improvement in current analysis time over ion chromatography may still be possible even with these longer columns. At the end of the second quarter, a set of longer columns was purchased, and work in this area was scheduled for the third quarter.

Third quarter efforts focused on two areas: 1) determining detection limits and calibration curves for all species using the chromate-based electrolyte and 2) establishing detection limits and calibration curves for nitrate and nitrate in the chloride-based electrolyte system using the longer, 1-m columns. Figure 2.1 shows a typical chromatogram for the chromate-based system. Good resolution of all anions of interest, such as bromide, chloride, sulfate, nitrite, nitrate, fluoride, phosphate and carbonate, is clearly achievable for values ranging from approximately 10 ppm to <1 ppm. Varying the concentrations of neighboring components allowed determination of the minimum detectable limits (MDL), as well as an estimate of the minimum quantifiable concentration of each individual species. Table 2.2 summarizes these results.

During these detection and quantification measurements, a problem was identified that appears to have the potential for preventing routine identification of any specific signal in an unknown sample. The problem is illustrated in Figure 2.2. The peak positions shift so much as a function of the sample's concentration that identification becomes problematic. For example, in Figure 2.2, an unknown signal at just under 2.6 min could be assigned either to bromide, nitrate, or nitrite. Standard additions might not solve the identification question since the addition of further material will again change the peak positions. Clearly, unless resolved, this problem could become detrimental to using this system for anion detection. Further work is needed on locating an internal standard, sufficiently clear from the retention time of the anions of interest and sufficiently inert to sample concentration changes.

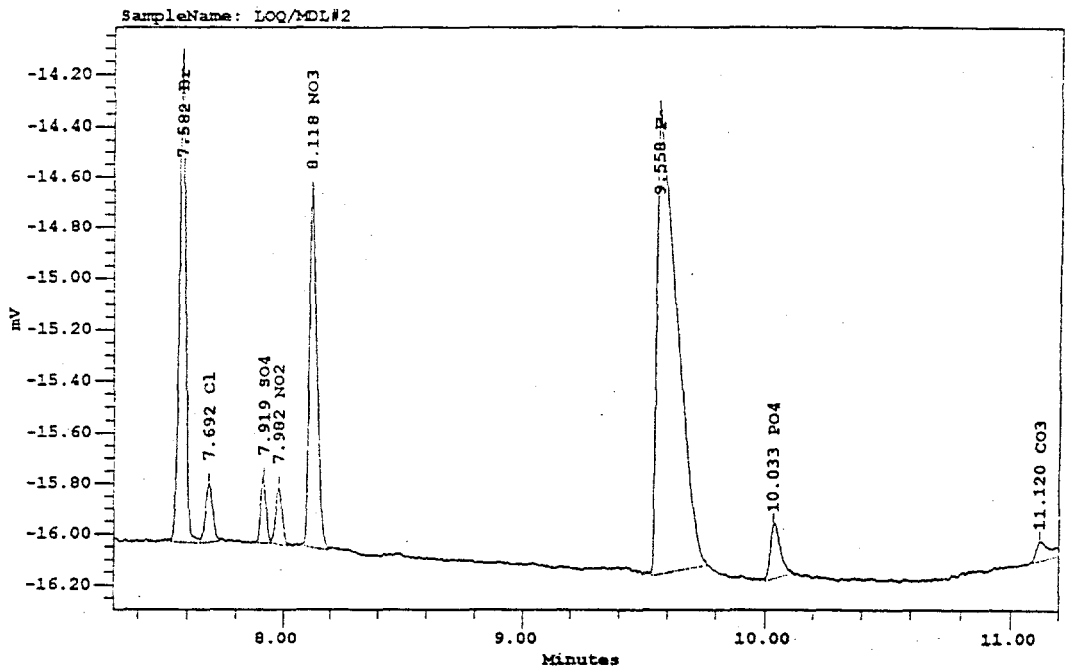

Figure 2.1. Sample Chromatogram from the Capillary Ion Analyzer. Conditions: chromate-based electrolyte, 1-m column. Sample composition: 10 ppm Br, 1 ppm Cl, 1 ppm SO_4, 1 ppm NO_2, 10ppm NO_3, 10 ppm F, 1 ppm PO_4.

Table 2.2. Detection and Quantification Limit Estimates (chromate based electrolyte, 1-m column)

Anion Analyte	Upper limit	Lower limit	Detection limit (3 σ)
Br	>10	<1	0.22
Cl	>10	1	0.22
SO_4	>10	1	0.32
NO_2	(a)	<1	0.1
NO_3	(a)	<1	0.1
F	>10	1	0.14
PO_4	>10	1	0.13
CO_3	(b)	(b)	(b)

(a) Results using a chloride-based electrolyte.
(b) Measurements not performed.

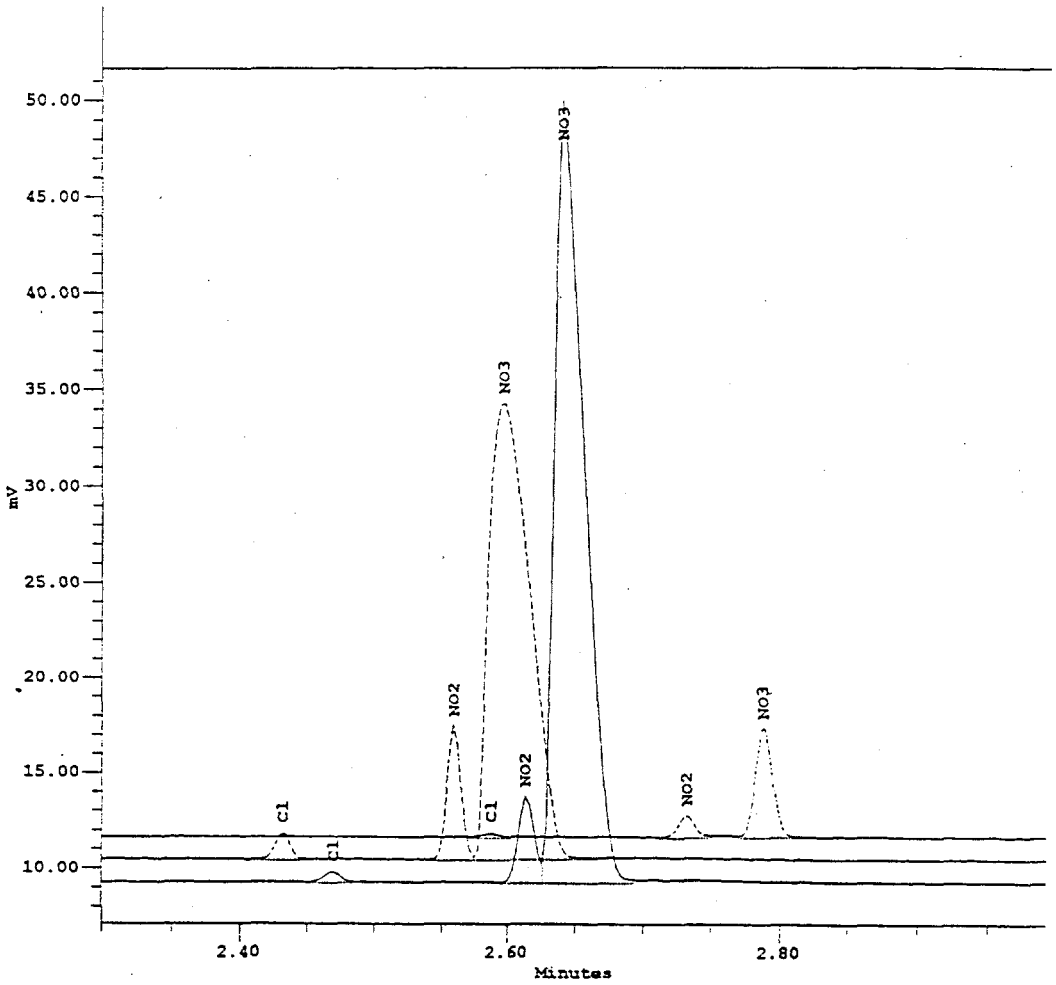

Figure 2.2. Changes in Peak Position as a Function of Anion Concentration. Note that the sample labeled as Cl is actually Br.

Several features regarding the utility of the capillary ion analyzer for analysis of solutions derived from Hanford tank sludges were clarified during the third quarter.

- The use of a combination of measurements, one with a chloride-based electrolyte and another with a chromate-based electrolyte, appears to allow detection and quantification of all components in a multicomponent solution of inorganic anions.

- Examination of detection limits as a function of the concentration of other species with similar retention values indicates that nitrate has an insignificant impact on the quantification of sulfate. Nitrite does have an impact on sulfate detection, but only if the nitrite concentrations are appreciably larger than the sulfate concentrations.

- In general, sub-ppm levels are detectable and quantifiable for most analytes in these multicomponent samples. However, routine, automated identification and analysis of multicomponent mixtures may not be possible with the capillary ion analyzer because of how the peaks shift as a function of the sample's concentration.

2.3 Installation of Gamma Spectrometer

Gamma counting equipment was installed during the first quarter. This equipment is designed for quantitative determination of gamma-emitting isotopes and is used to analyze solutions generated during sludge pretreatment studies. The gamma spectrometer consists of a Princeton Instruments Model IGP 1013 intrinsic germanium detector, which is powered by an EG&G ORTEC Model 659 high voltage bias supply. The output from the detector is routed to an EG&G ORTEC Model 972 spectroscopy amplifier and then to an EG&G ORTEC Model 919 Spectrum Master™ multichannel analyzer, which, in turn, is interfaced to a Gateway 2000® computer. The system is operated through EG&G ORTEC GammaVision™ spectroscopy software.

During the second quarter, an energy calibration was performed using a multinuclide standard source. The gamma spectrum recorded for the standard was included in the second quarter report. The conclusion based on measurement of the standards is that resolution and quantification of these isotopes should be straightforward. During the third quarter, a technical procedure was written for the instrument, and a review process for use began.

3.0 Sludge Dissolution Modeling

Andrew R. Felmy, S. Michael Sterner, and James R. Rustad

Principal activities this quarter were directed toward the development of a thermochemical model for the major electrolytes in Hanford tank wastes that is consistent with the Environmental Simulation Program (ESP) formalism being used by WHC in process simulation. The aqueous thermodynamic model is developed for $Na\text{-}NO_3\text{-}NO_2\text{-}CO_3\text{-}F\text{-}PO_4\text{-}OH\text{-}Al(OH)_4\text{-}Cr(OH)_4\text{-}H_2O$, which are some of the major electrolytes present in tank wastes. The ESP parameters developed here, as well as the previously developed Pitzer parameters, accurately reproduce the binary and ternary experimental data to high ionic strength.

3.1 ESP Parameters

The goal of this particular thermodynamic model is to synthesize the results of isopiestic and solubility experiments in binary or ternary systems within the major tank electrolytes in order to make interpolation of these results into the multicomponent system as reliable as possible. Earlier experimental data on osmotic coefficients and phase equilibria along binary joins, e.g., $NaNO_3$-NaOH, in the tank major electrolyte system, $NaNO_3\text{-}NaNO_2\text{-}NaOH\text{-}Na_3PO_4\text{-}Na_2CO_3\text{-}NaF\text{-}NaAl(OH)_4$, were used to fit parameters for a Pitzer ion-interaction model. This effort resulted in a model which successfully predicted ternary phase equilibria for $NaNO_3\text{-}NaNO_2\text{-}H_2O$, $NaOH\text{-}NaNO_3\text{-}H_2O$, and $NaOH\text{-}NaNO_3\text{-}H_2O$. While this effort was being completed, various process simulators were being tested by engineers at WHC for their suitability in tank waste processing. Through these tests, the WHC engineers determined that the ESP system developed by OLI Systems, Inc., best suited their needs. The parameters in the ESP electrolyte model have not been validated at the extreme ionic strength of tank brines. We have, therefore, refit the experimental data to develop parameters for the ESP electrolyte model. The ESP parameters that are developed in this report are summarized in Table 3.1; the standard chemical potentials of aqueous and solid species are summarized in Table 3.2.

3.2 Experimental Procedures

The experimental studies include measurement of osmotic coefficients of $NaNO_3$, $NaNO_2$, and Na_3PO_4 solutions at 50°C and 100°C. These were carried out using the isopiestic method. Isopiestic measurements are one of the best methods of determining the thermodynamic properties of binary electrolyte solutions at high concentration, owing to both the precision of the measurements and to the large changes in water activity that can occur in these solutions.

The isopiestic apparatus and experimental procedures used in this study are similar to those described in Grojtheim et al. (1988). Briefly, isopiestic equilibrium was established between 12 vitreous carbon cups placed inside a stainless steel container. Measurements on $NaNO_3$ and $NaNO_2$ were conducted simultaneously. Four of the cups contained $NaNO_3$; four cups contained $NaNO_2$; and four cups contained the reference solution $CaCl_2$. The measurements on Na_3PO_4 and NaF were conducted separately with six cups containing either Na_3PO_4 or NaF; four containing the reference salt, in this case KCl; and two cups remaining empty in order to obtain more accurate wafer weight corrections (see below). Each of the cups was weighed empty, with added salt, after placing a silicon rubber gasket on each cup. The stainless steel container was constructed so as to allow the wafers to be sealed on top of the cups before the cups were removed from the stainless steel vessel.

Table 3.1. ESP Parameters Developed in This Report

Interaction	Parameter	a_1	a_b	a_3
Na-OH	b	-5.3089272D-01	3.6293523D-03	-5.4595212D-06
	c	5.6668640D-02	-2.9578351D-04	3.8388123D-07
$Na-NO_3$	b	1.6345726D-01	-2.0680875D-04	
NO_3-NaNO_3	λ	-3.9532920D-02		
$OH-NaNO_3$	λ	2.9681434D-02		
$Na-NO_2$	b	8.0685495D-02		
$Na-NaNO_2$	λ	5.5418675D-02		
$Na-SO_4$	b	-1.3458069D-01	3.6216829D-04	
	c	9.9980593D-03	-2.7884502D-05	
$Na-CO_3$	b	3.4355237D-02	-1.1105747D-04	
	c	-3.0720415D-01	9.8183492D-04	
Na-F	b	-1.4392449D-01	4.9156585D-04	
	c	5.8707784D-03	-1.9266245D-05	
$Na-PO_4$	b	-2.0450466D-02		
$Na-Al(OH)_4$	b	1.4121823D-01	-3.4867426D-04	
$Na-Al(OH)_4$	c	-1.5973193D-03	3.1378411D-06	
$Na-Cr(OH)_4$	b	1.4121823D-01	-3.4867426D-04	
$Na-Cr(OH)_4$	c	-1.5973193D-03	3.1378411D-06	

Equilibration periods generally extended for 4 days to 1 week, depending on the temperature and salt concentration. After equilibration, the cups were sealed inside the vessel and removed for weighing on a five-place balance. After being weighed, the wafers were removed, dried with a paper towel, and reweighed in order to correct for any wafer weight gain during equilibration. The wafer weight gain correction was generally minor at high concentration but became significant at lower concentration when water could condense on the bottom of the wafer following cooling. Therefore, as a way to obtain more accurate wafer weight corrections for the relatively low concentration NaF and Na_3PO_4 solutions, two empty cups were placed inside the apparatus and carried along as blanks for determining wafer weight corrections. Osmotic coefficients were then calculated from the isopiestic molalities and the water activities calculated for the reference salts from the data compiled for $CaCl_2$ by Ananthaswamy and Atkinson (1985). For a detailed description of the isopiestic method, refer to Rard and Platford (1991).

Table 3.2. Standard Chemical Potentials of Aqueous and Solid Species Developed in This Report

Species	a_1	a_2	a_3
Na^+	-1.05651D+02		
OH^-	-6.34350D+01		
NO_3^-	-4.22530D+01		
NO_2^-	-1.29900D+01		
F^-	-1.12460D+02		
CO_3^{2-}	-2.12944D+02		
PO_4^{3-}	-4.10947E+02		
SO_4^{2-}	-3.00386D+02		
$Cr(OH)_4^-(aq)$	-318.987d0		
$Al(OH)_4^-(aq)$	-526.677d0		
$NaNO_3(aq)$	-1.5005298D+02	9.3093910D-03	
$NaNO_2(aq)$	-1.1715195D+02	-1.1444769D-03	
$NaCr(OH)_4(aq)$	-4.2487359D+02		
$NaNO_3(s)$	-1.5026607D+02	1.5574661D-02	
$NaNO_2(s)$	-1.1792963D+02	1.0028728D-02	
$Na_2CO_310H_2O(s)$	-2.1259580D+03	4.1599116D+00	-5.5933084D-03
$Na_2CO_37H_2O(s)$	-1.2375816D+03	4.7902054D-01	
$Na_2CO_31H_2O(s)$	-5.1948073D+02	9.2312957D-04	
$Na_3PO_412H_2O(s)$	-1.8837698D+03		
NaF	-2.1924952D+02		
$Al(OH)_3(s)$[a]	-5.2179482D+02	1.6805732D-01	-1.350097D-04
$Cr(OH)_3(s)$	-.265461000E+03		

(a) The chemical potential expression for $Al(OH)_3$ contains an additional term: 5.2952178D+03/T.

3.3 Thermodynamic Model

The ESP electrolyte model incorporates features from several sources, including data from this task. Fundamental modifications were incorporated into the nonlinear parameter fitting code NONLIN, which enabled considerable simplification of the temperature dependence of model parameters relative to those computed in the earlier study. All parameters reported here have, at most, a quadratic dependence on temperature.

The Debye-Hückel term and the standard chemical potential of H_2O were taken from Møller (1988). The Bromley ESP parameters for NaOH, NaF, and Na_2SO_4 were computed by fitting to osmotic coefficients as predicted by previously derived Pitzer parameters based on data from Pabalan and Pitzer (1978) (NaOH), Pitzer (1991) (NaF), and Greenberg and Møller (1989) (Na_2SO_4). Osmotic data at 25°C are compared with experimental data from Robinson and Stokes (1965) in Figure 3.1 (NaOH), Figure 3.2 (NaF), and Figure 3.3 (Na_2SO_4), respectively.

3.4 Binary Electrolytes

3.4.1 $NaNO_3$

Osmotic data at 25°C (Figure 3.4), 50°C (Figure 3.5), 75°C (Figure 3.6), and 100°C (Figure 3.7) were fit to the ESP model. As in the case of the fit to the Pitzer model in earlier experiments, fitting the ESP model to the osmotic data at all four temperatures required the neutral ion pair $NaNO_3(aq)$. Fitting these data required a $b_{Na\text{-}NO3}$ with linear temperature dependence and a constant $\lambda_{NO3\text{-}NaNO3}$ (Table 3.1).

Solubility data (Linke 1965) were used to fit the chemical potential of solid $NaNO_3$; the results are shown in Figure 3.8. The amount of ion association is shown in Figure 3.8 and is greater than the amount predicted using the Pitzer model, but does show the expected trend of increasing association with temperature and ionic strength. The standard chemical potential of both the $NaNO_3(aq)$ ion pair and $NaNO_3(s)$ is given in Table 3.2.

3.4.2 $NaNO_2$

Osmotic data at 25°C, 50°C, and 100°C are shown in Figures 3.9, through 3.11, respectively. An ion pair $NaNO_2(aq)$ is required to fit the data, and, as was the case in Felmy et al. (1994), a larger amount of ion-pairing is required for $NaNO_2$ than for $NaNO_3$. In the case of $NaNO_2$, we were able to fit the data adequately using a constant b_{NaNO2} and a constant $\lambda_{Na\text{-}NaNO2(aq)}$. These parameters are given in Table 3.1. As in the case of $NaNO_3$, the standard chemical potentials for $NaNO_2(aq)$ and $NaNO_2(s)$ are linearly dependent on temperature. The fit to the solubility data (Linke 1965) is illustrated in Figure 3.12.

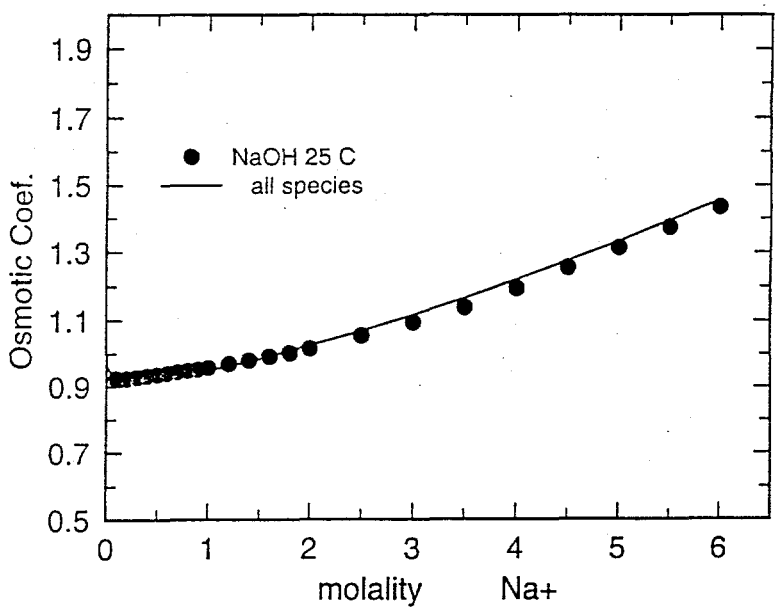

Figure 3.1. Osmotic Coefficient of NaOH-H_2O Solution at 25°C. Solid circles represent experimental data from Robinson and Stokes (1959); solid line represents the fit to these data using ESP parameters derived in this work (Table 3.1).

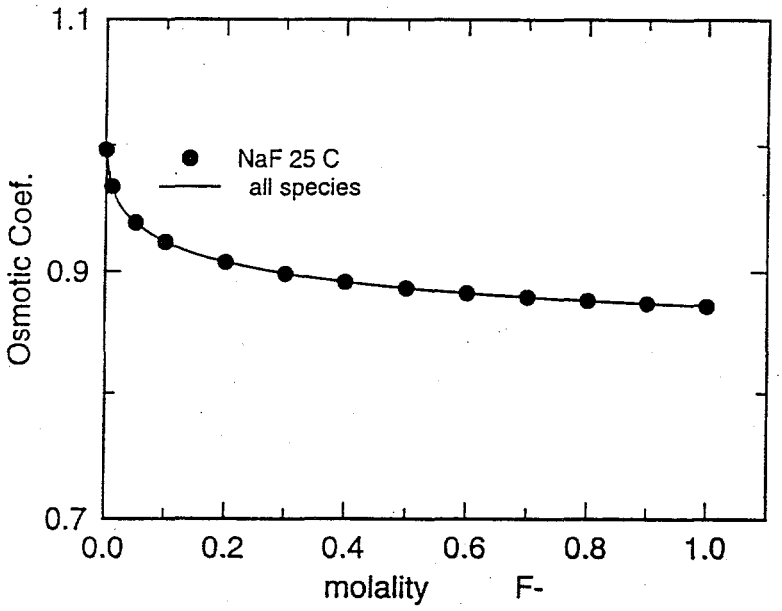

Figure 3.2. Osmotic Coefficient of NaF-H_2O Solution at 25°C. Solid circles represent experimental data from Robinson and Stokes (1959); solid line represents the fit to these data using ESP parameters derived in this work (Table 3.1).

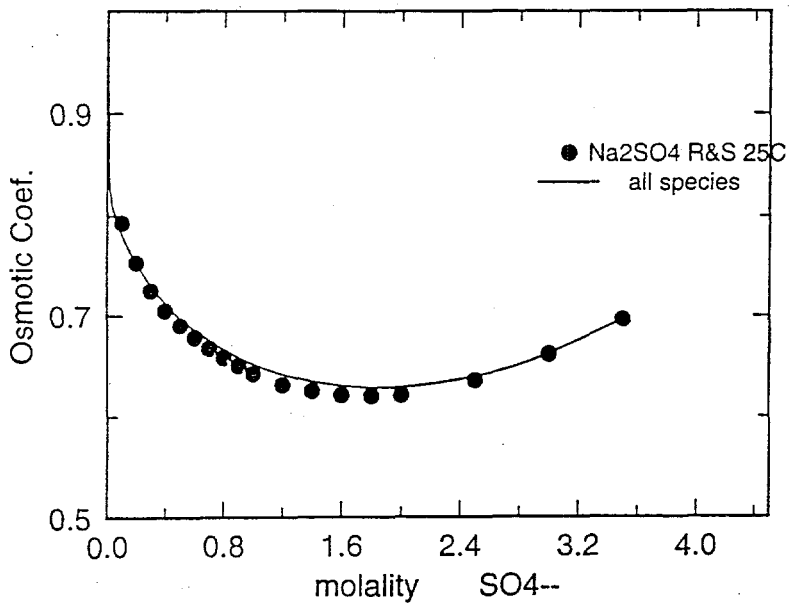

Figure 3.3. Osmotic Coefficient of Na_2SO_4-H_2O Solution at 25°C. Solid circles represent experimental data from Robinson and Stokes (1959); solid line represents the fit to these data using ESP parameters derived in this work (Table 3.1).

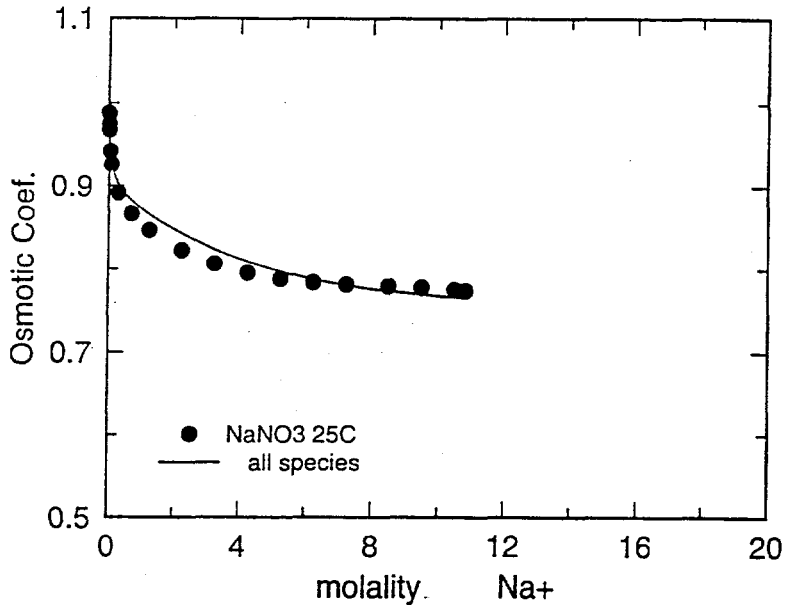

Figure 3.4. Osmotic Coefficient of $NaNO_3$-H_2O Solution at 25°C. Solid circles are taken from Wu and Hamer (1980); solid line is the fit to these data using ESP parameters in Table 3.1 and the chemical potential expression for $NaNO_3$(s) and $NaNO_3$(aq) in Table 3.2.

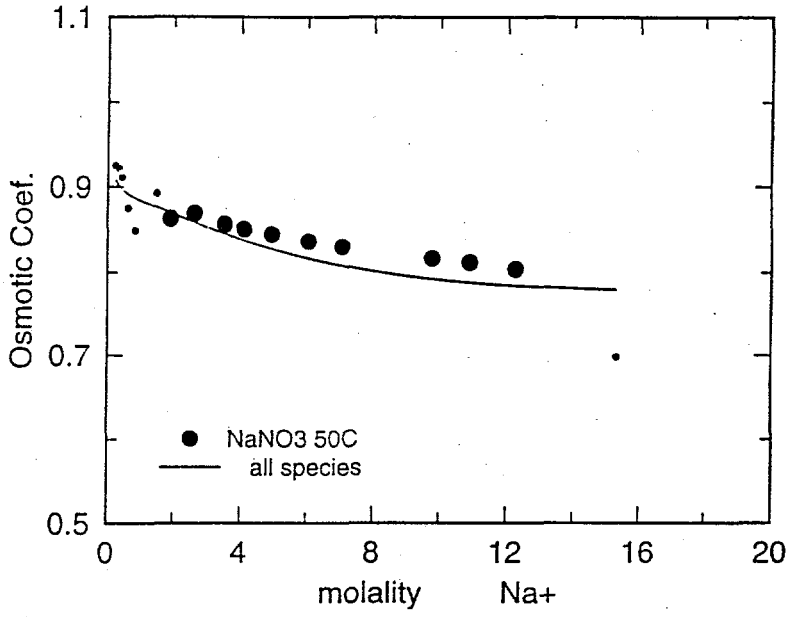

Figure 3.5. Osmotic Coefficient of $NaNO_3$-H_2O Solution at 50°C. Solid circles are earlier experimental data; solid line represents the fit to these data using the ESP parameters in Table 3.1 and the chemical potential expression for $NaNO_3$(s) and $NaNO_3$(aq) in Table 3.2.

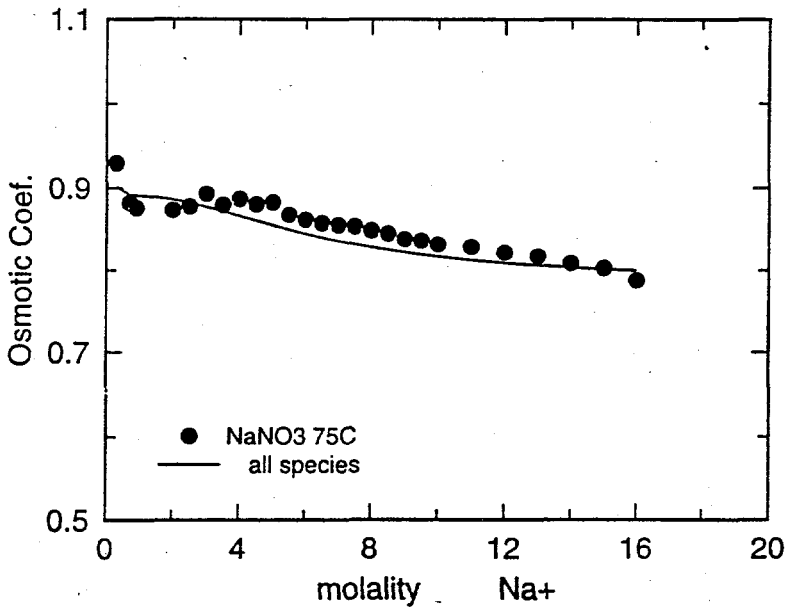

Figure 3.6. Osmotic Coefficient of $NaNO_3$-H_2O Solution at 75°C. Solid circles are experimental data (Shpigel and Mishcenko 1967); solid line represents the fit to these data using the ESP parameters in Table 3.1 and the chemical potential expression for $NaNO_3$(s) and $NaNO_3$(aq) in Table 3.2.

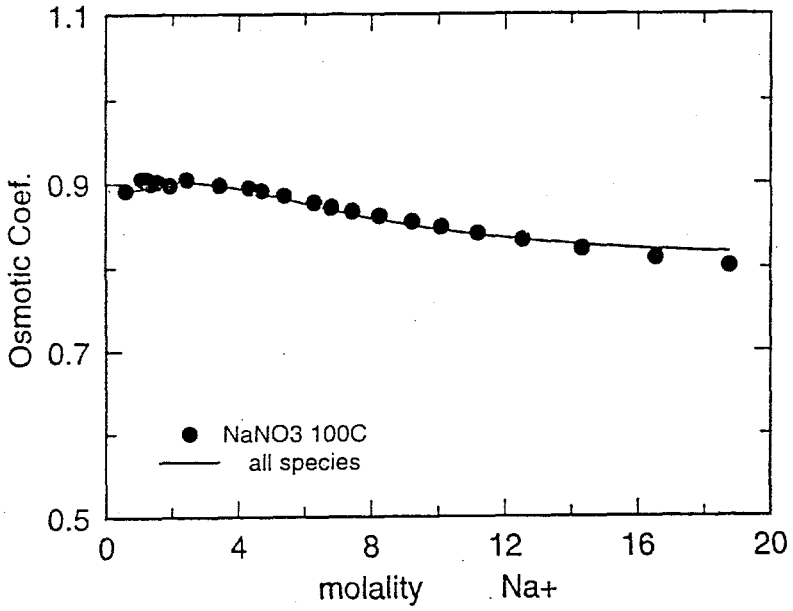

Figure 3.7. Osmotic Coefficient of $NaNO_3$-H_2O Solution at 100°C. Solid circles are earlier experimental data; solid line represents the fit to these data using the ESP parameters in Table 3.1 and the chemical potential expression for $NaNO_3$(s) and $NaNO_3$(aq) in Table 3.2.

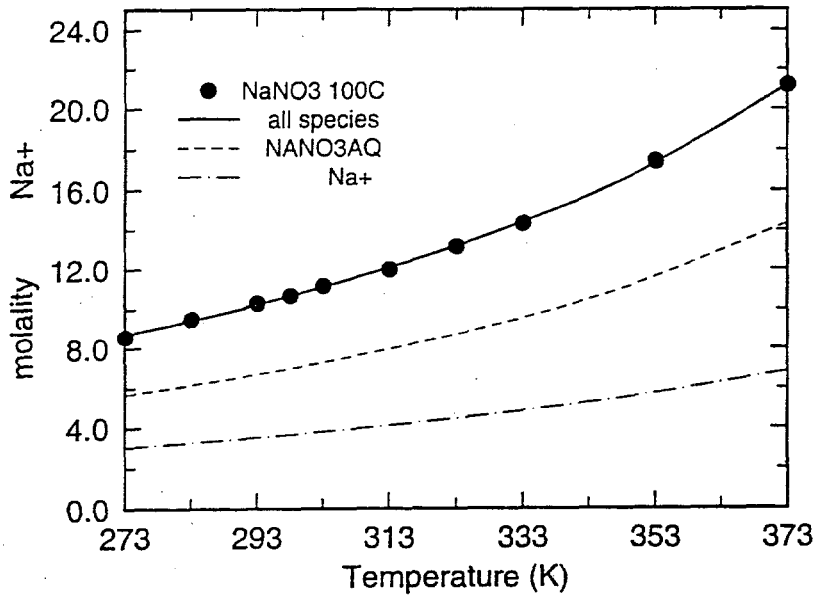

Figure 3.8. $NaNO_3$ Solubility. Solid circles are experimental data from Linke (1965); solid line represents the fit to these data using the ESP parameters in Table 3.1 and the chemical potential expression for $NaNO_3$(s) and $NaNO_3$(aq) in Table 3.2. Dashed line represents the contribution from the ion pair, and the dash-dot line is the contribution from Na^+.

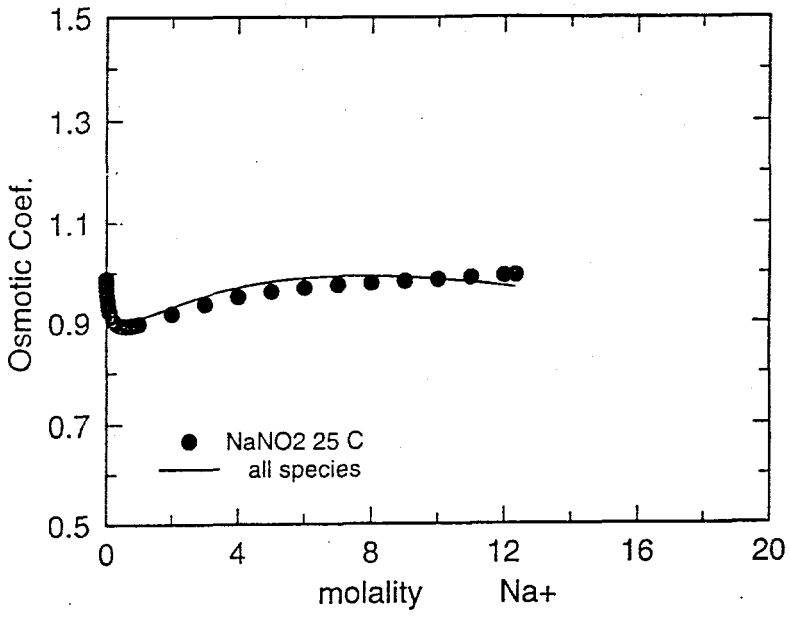

Figure 3.9. Osmotic Coefficient of $NaNO_2$-H_2O Solution at 25°C. Solid circles are taken from Wu and Hamer (1980); solid line is the fit to these data using ESP parameters in Table 3.1 and the chemical potential expression for $NaNO_2$(s) and $NaNO_2$(aq) in Table 3.2.

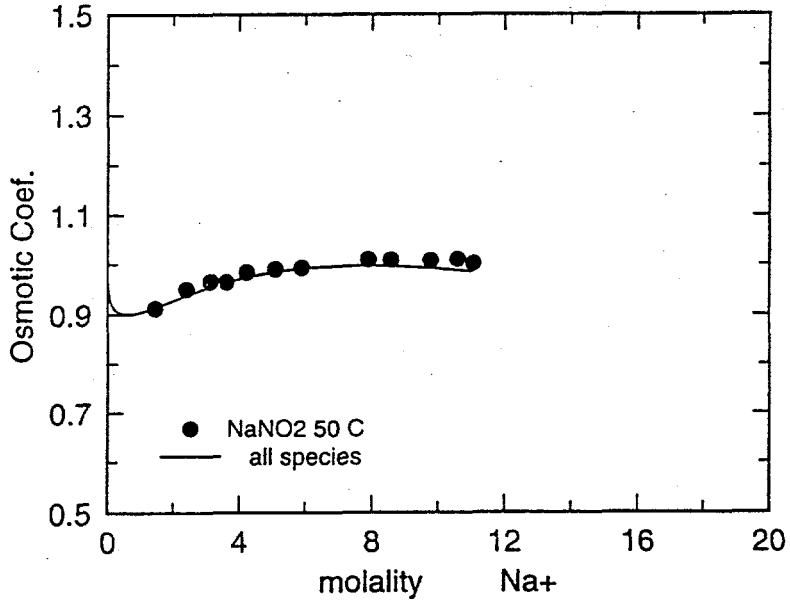

Figure 3.10. Osmotic Coefficient of $NaNO_2$-H_2O Solution at 50°C. Solid circles are earlier experimental data; solid line represents the fit to these data using the ESP parameters in Table 3.1 and the chemical potential expression for $NaNO_2$(s) and $NaNO_2$(aq) in Table 3.2.

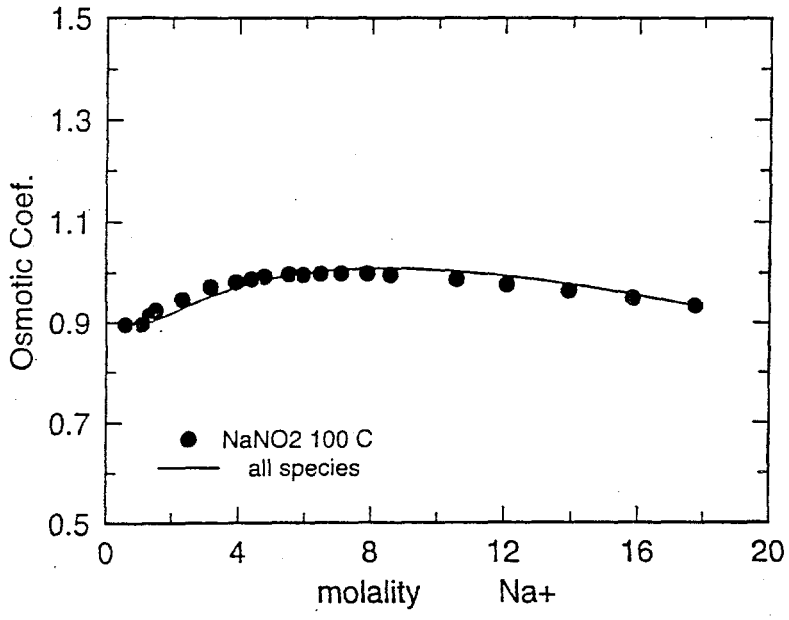

Figure 3.11. Osmotic Coefficient of $NaNO_2$-H_2O Solution at 100°C. Solid circles are earlier experimental data; solid line represents the fit to these data using the ESP parameters in Table 3.1 and the chemical potential expression for $NaNO_2$(s) and $NaNO_2$(aq) in Table 3.2.

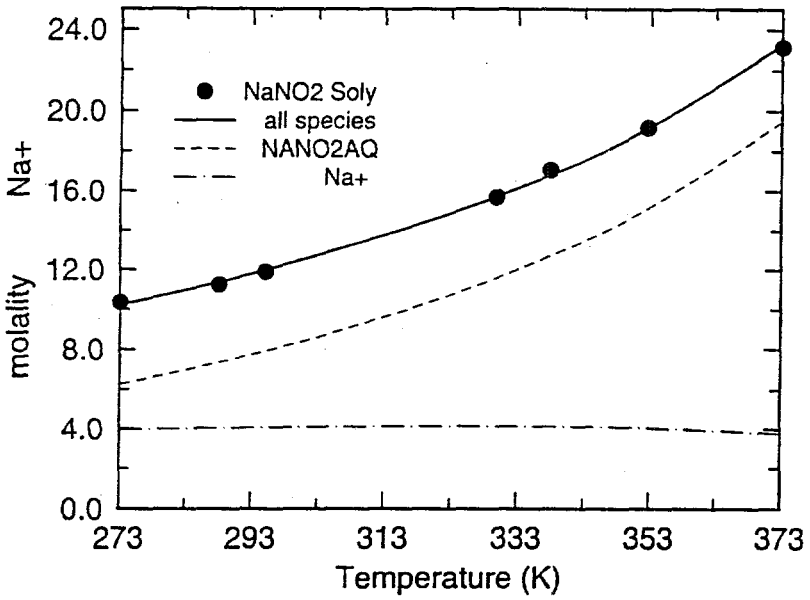

Figure 3.12. $NaNO_2$ Solubility. Solid circles are experimental data from Linke (1965); solid line represents the fit to these data using the ESP parameters in Table 3.1 and the chemical potential expression for $NaNO_2$(s) and $NaNO_2$(aq) in Table 3.2. Dashed line represents the contribution from the ion pair, and the dash-dot line is the contribution from Na^+.

3.4.3 Na_2CO_3

Na_2CO_3 is considerably less soluble than either $NaNO_3$ or $NaNO_2$, and no ion-pair was required. The osmotic data of Peiper and Pitzer (1982) at 5°C (Figure 3.13), 15°C (Figure 3.14), 25°C (Figure 3.15), 35°C (Figure 3.16), and 45°C (Figure 3.17) are adequately modeled using a $b_{Na\text{-}CO3}$ and $c_{Na\text{-}CO3}$ with linear temperature dependence. Fits for the standard chemical potentials for $Na_2CO_3{\cdot}10H_2O$, $Na_2CO_3.7H_2O$, and $Na_2CO_3.H_2O$ are shown in Figure 3.18. The standard chemical potential for the solid phase $Na_2CO_3{\cdot}10H_2O$ has a quadratic temperature dependence, while those for the $Na_2CO_3.7H_2O$ and $Na_2CO_3.H_2O$ phases have a linear temperature dependence.

3.4.4 Na_3PO_4

The $b_{Na\text{-}PO4}$ given in Bromley (1973) does not adequately reproduce the experimental osmotic data at 25°C (Robinson and Stokes 1959). These data appear inconsistent with measurements of the osmotic coefficient at 50°C and 100°C in earlier experiments. Until this discrepancy is resolved, we recommend using the 25°C $b_{Na\text{-}PO4}$ given in Table 3.1 and the standard chemical potential for solid Na_3PO_4 given in Table 3.2. As shown in Figure 3.19, the b parameter given in Table 3.2 does a much better job of reproducing the experimental data than does the standard ESP value.

3.5 Higher Order Systems

As discussed above, the purpose of the thermodynamic model is to be able to interpolate phase relations from binary systems (or ternary systems) into multicomponent systems with as much reliability as possible. In the following sections, the model developed from the binary electrolyte data will be applied to ternary systems for which there are experimental data. The extension of our model to ternary and higher order chemical systems assumes that the binary interactions (and hence, the binary interaction parameters) account for the majority of all the interactions within the system, i.e., that three-, four-, etc. particle interactions yield only minor contributions. The extent to which this assumption is valid governs the accuracy with which the properties of higher order systems will be predicted using our model (which is based only on binary interactions).

Owing to characteristics of some chemical systems, certain of the necessary binary interaction parameters are best established from experimental data on higher order systems. For example, the limited solubility exhibited by some salts prevents the evaluation of specific ion interactions between their constituents when they are the only ions present in solution. For this reason, some of the ESP parameters presented in this report, although representing binary interactions, were actually derived from experimental data on ternary or higher order systems.

The following sections include several examples where our binary electrolyte does indeed provide valid predictions of more chemically complex systems; however, the validity of this assumption needs to be experimentally verified for each chemical system.

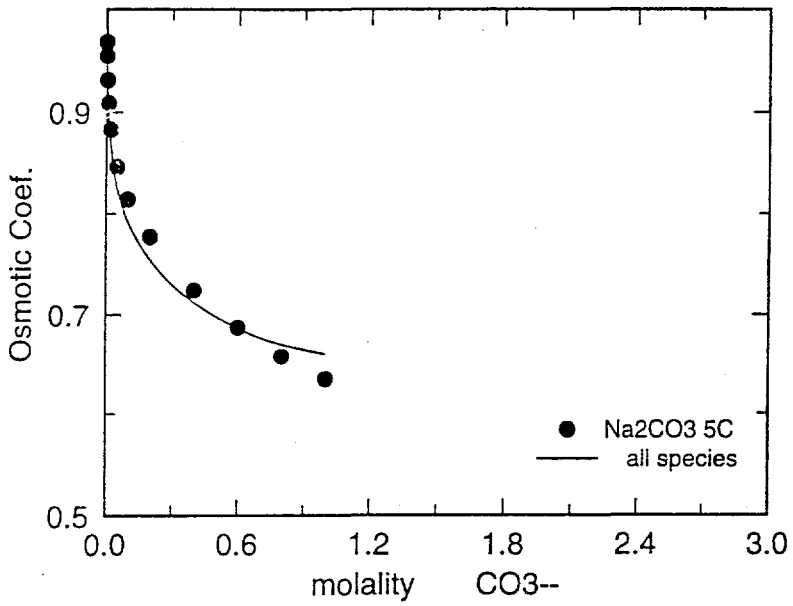

Figure 3.13. Osmotic Coefficient of Na_2CO_3 Solution at 5°C. Solid circles are data from Peiper and Pitzer (1982); solid line represents the fit to these data using the ESP parameters in Table 3.1.

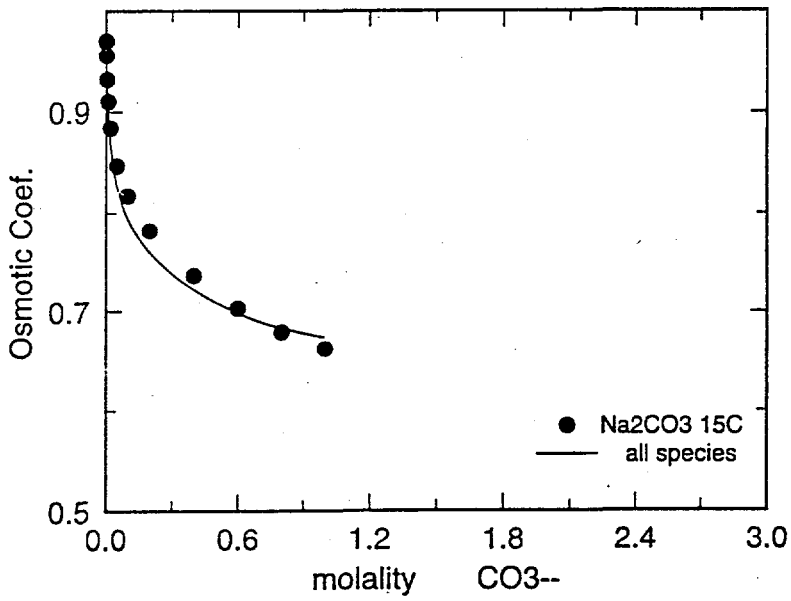

Figure 3.14. Osmotic Coefficient of Na_2CO_3 Solution at 15°C. Solid circles are data from Peiper and Pitzer (1982); solid line represents the fit to these data using the ESP parameters in Table 3.1.

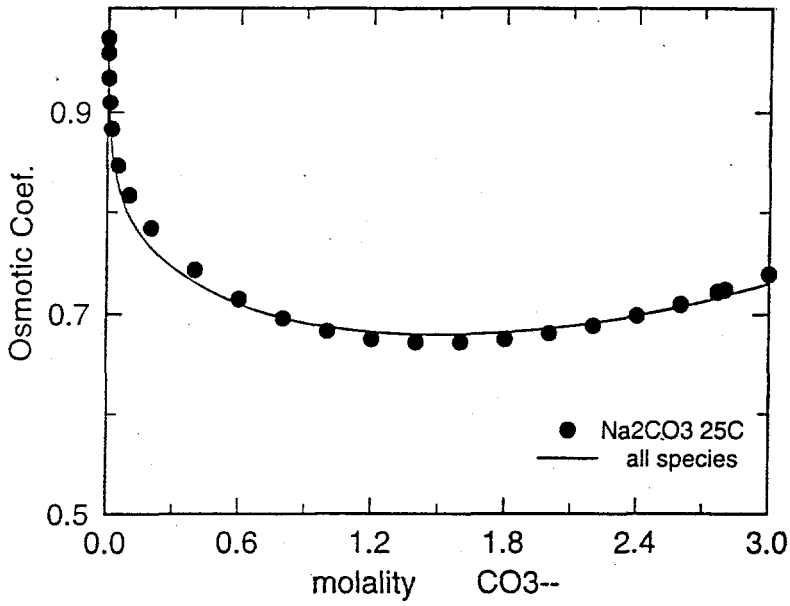

Figure 3.15. Osmotic Coefficient of Na_2CO_3 Solution at 25°C. Solid circles are data from Peiper and Pitzer (1982); solid line represents the fit to these data using the ESP parameters in Table 3.1.

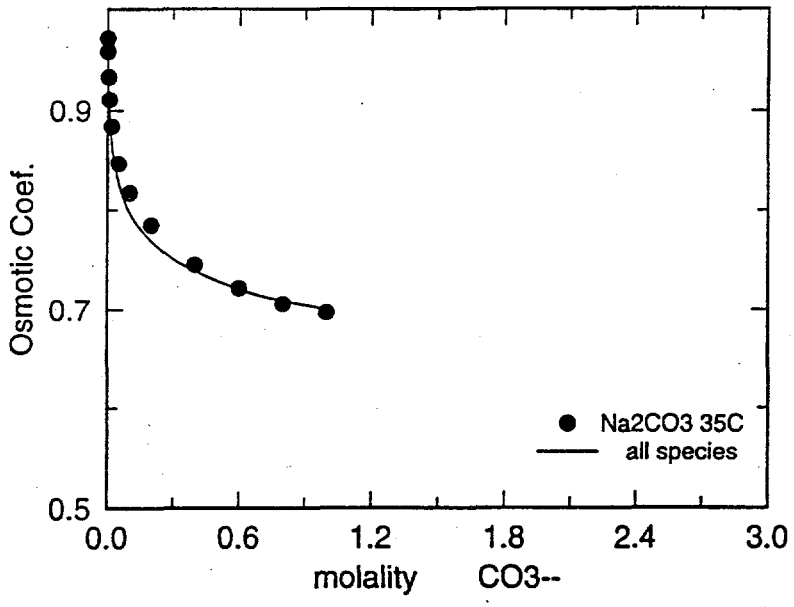

Figure 3.16. Osmotic Coefficient of Na_2CO_3 Solution at 35°C. Solid circles are data from Peiper and Pitzer (1982); solid line represents the fit to these data using the ESP parameters in Table 3.1.

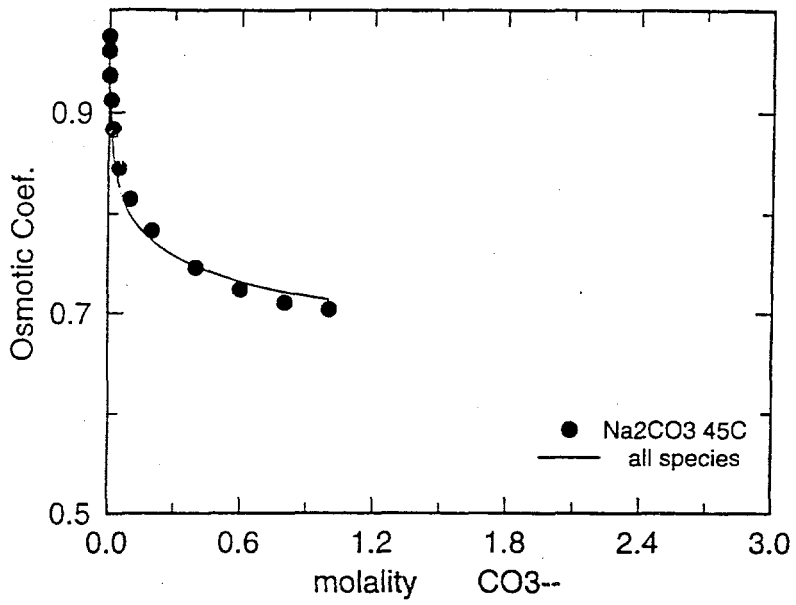

Figure 3.17. Osmotic Coefficient of Na_2CO_3 Solution at 45°C. Solid circles are data from Peiper and Pitzer (1982); solid line represents the fit to these data using the ESP parameters in Table 3.1.

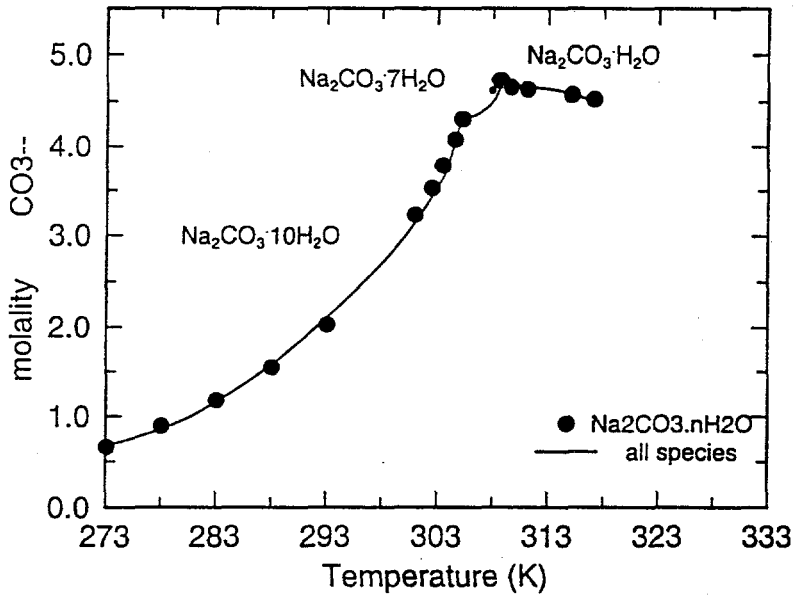

Figure 3.18. Solubility Data from Linke (1965) with Model Fits for $Na_2CO_3 \cdot 10H_2O$, $Na_2CO_3 \cdot 7H_2O$, and $Na_2CO_3 \cdot H_2O$ Using Standard Chemical Potentials Given in Table 3.2.

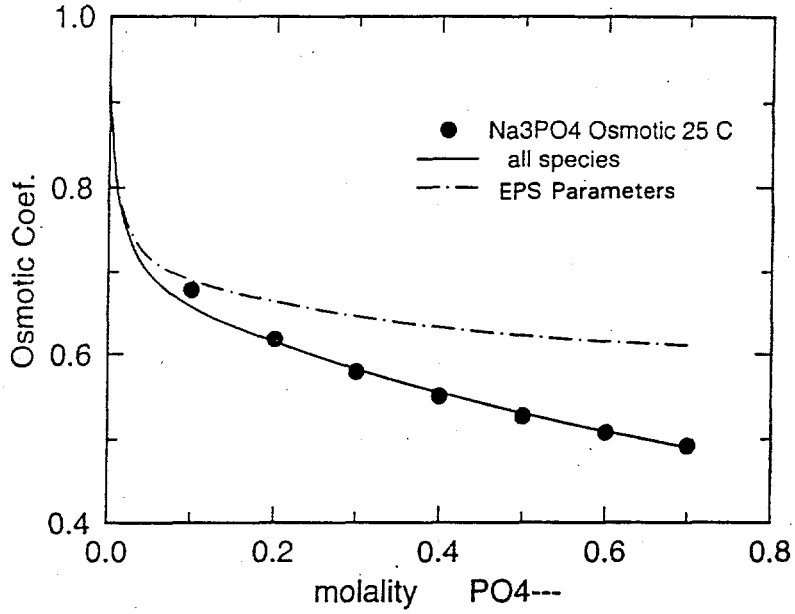

Figure 3.19. Osmotic Data at 25°C for Na_3PO_4. Solid line shows current model predictions and dashed line shows predictions using the standard ESP parameters.

3.5.1 The Aqueous System: Na-OH-Al(OH)$_4$

ESP parameters for Na-Al(OH)$_4$ were fit using experimental data on gibbsite solubility in Wesolowski (1992). As can be seen in Figures 3.20 through 3.23, the data can be fit adequately with the Bromley b and c terms linear in temperature (given in Table 3.1). No ion pair is required. In the Pitzer model for Na-K-Cl-OH-Al(OH)$_4$ developed by Wesolowski (1992), interaction parameters for both $Al(OH)_4^-$-OH^-, and Na-$Al(OH)_4^-$-OH^- were employed. The ESP model does not allow anion-anion or ternary interactions; however, as shown in these figures, the ESP model does quite well on the relevant subset of the data in Wesolowski (1992).

3.5.2 The Aqueous System: Na-OH-NO_3-Al(OH)$_4$

Prediction of the solubility of gibbsite in Na-OH-NO_3 solutions using the Na-OH, Na-NO_3, $NaNO_3$(aq)-OH, and Na-Al(OH)$_4$ parameters developed above are shown in Figures 3.24 through 3.27. The level of agreement between predicted and experimental values is not as good as that obtained in earlier experiments using the Pitzer electrolyte model, but is nevertheless adequate considering the experimental uncertainty in aluminate concentration. Limitations in the ESP model arise because of its failure to account for interactions between ions of the same sign, which results in limited flexibility in this chemical system compared with the Pitzer ion interaction formalism. Specifically, there is no parameter designated in the ESP model to represent the Al(OH)$_4$-NO_3 interaction.

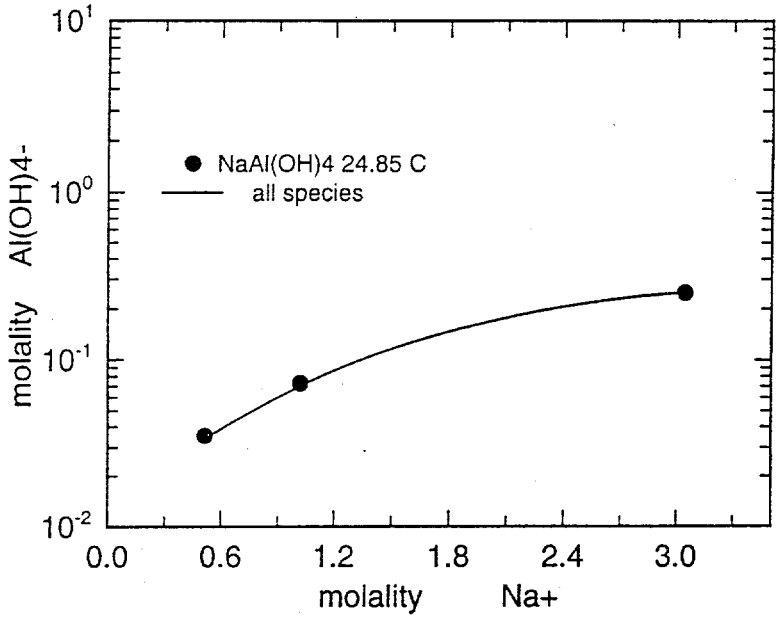

Figure 3.20. Solubility of Gibbsite in Sodium Hydroxide Solution at 25°C. Solid circles represent experimental data from Wesolowski (1992); solid line represents the fit to these data using ESP parameters derived in this work (Table 3.1).

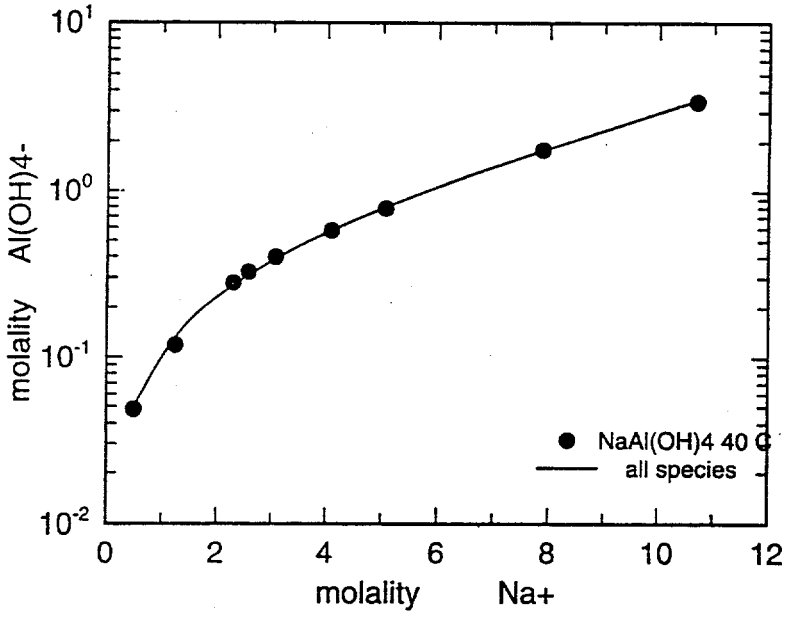

Figure 3.21. Solubility of Gibbsite in Sodium Hydroxide Solution at 40°C. Solid circles represent experimental data from Russell et al. (1955); solid line represents the fit to these data using ESP parameters derived in this work (Table 3.1).

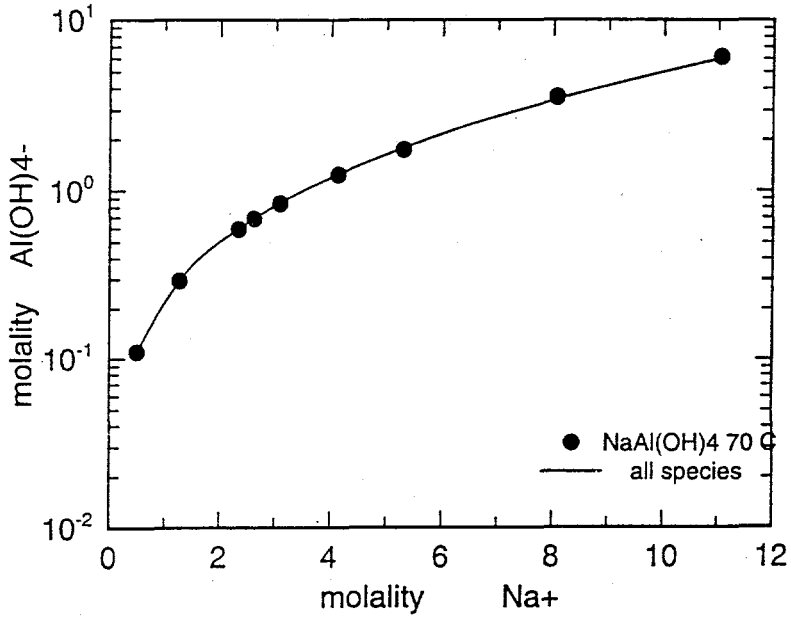

Figure 3.22. Solubility of Gibbsite in Sodium Hydroxide Solution at 70°C. Solid circles represent experimental data from Russell et al. (1955); solid line represents the fit to these data using ESP parameters derived in this work (Table 3.1).

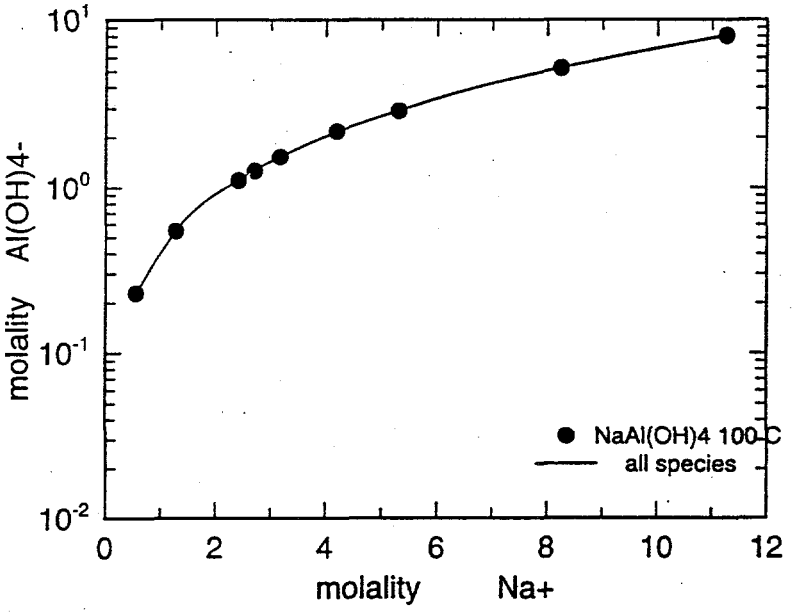

Figure 3.23. Solubility of Gibbsite in Sodium Hydroxide Solution at 100°C. Solid circles represent experimental data from Russell et al. (1955); solid line represents the fit to these data using ESP parameters derived in this work (Table 3.1).

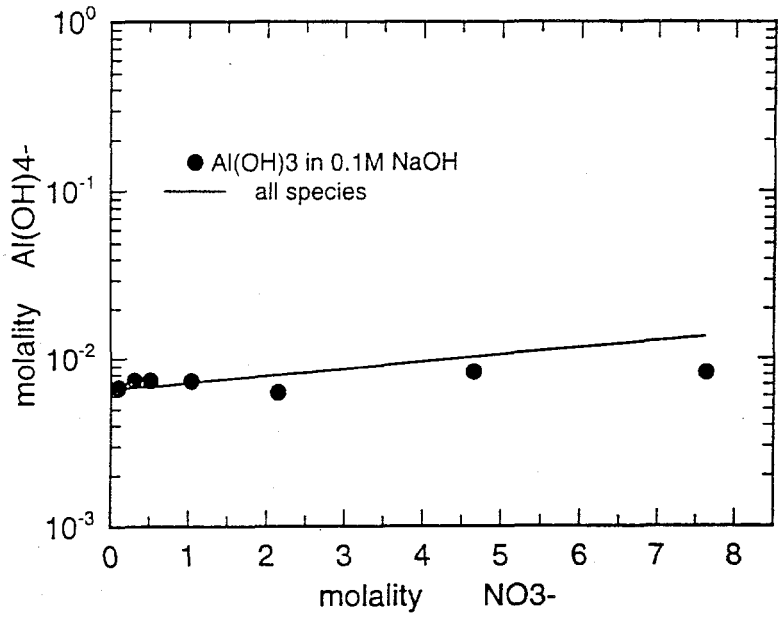

Figure 3.24. Solubility of Gibbsite in Na-NO_3-OH Solution at 0.1 M NaOH and 25°C. Solid circles represent earlier experimental data; solid line represents the fit to these data using ESP parameters derived in this work (Table 3.1).

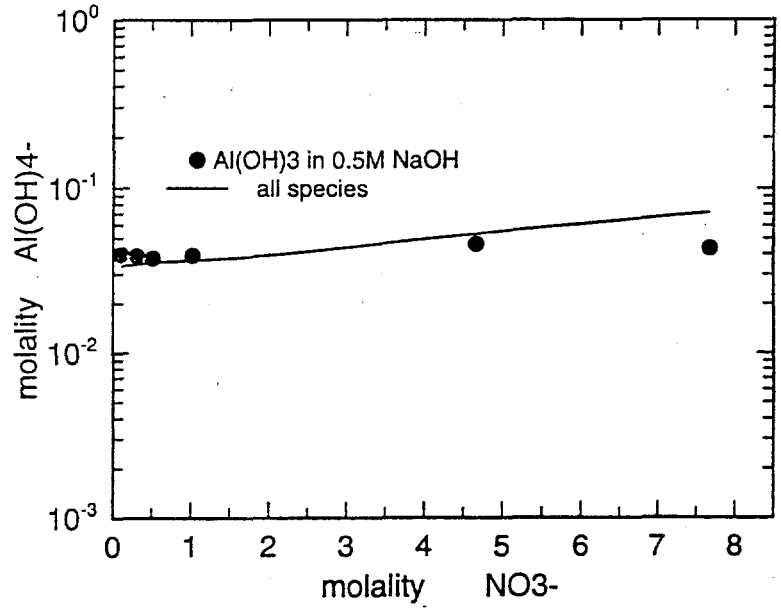

Figure 3.25. Solubility of Gibbsite in Na-NO_3-OH Solution at 0.5 M NaOH and 25°C. Solid circles represent earlier experimental data; solid line represents the fit to these data using ESP parameters derived in this work (Table 3.1).

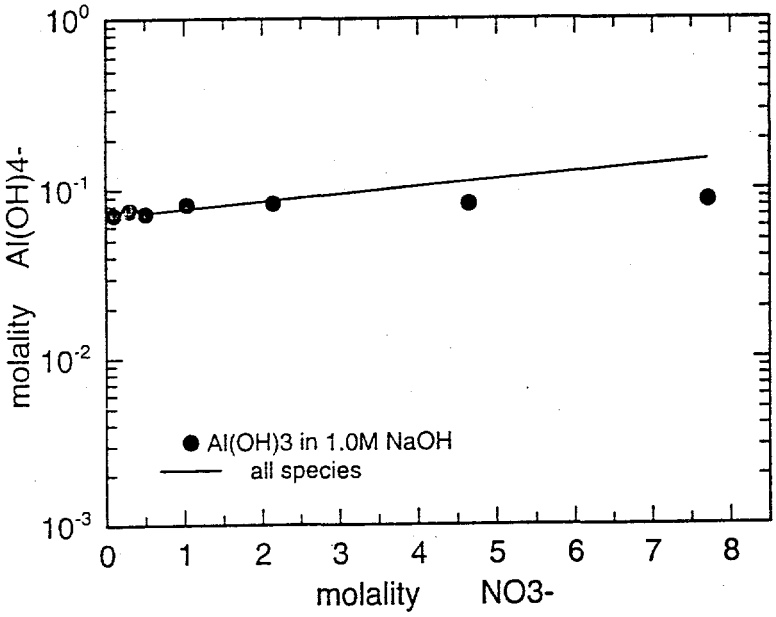

Figure 3.26. Solubility of Gibbsite in Na-NO_3-OH Solution at 1.0 M NaOH and 25°C. Solid circles represent earlier experimental data; solid line represents the fit to these data using ESP parameters derived in this work (Table 3.1).

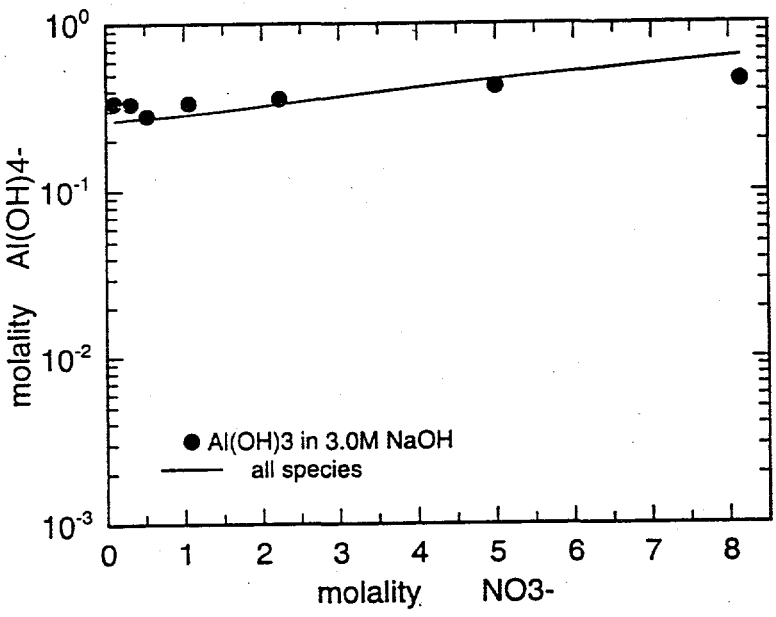

Figure 3.27. Solubility of Gibbsite in Na-NO_3-OH Solution at 3.0 M NaOH and 25°C. Solid circles represent earlier experimental data; solid line represents the fit to these data using ESP data using ESP parameters derived in this work (Table 3.1).

3.5.3 The Aqueous System: Na-OH-NO_2-$Al(OH)_4$

Prediction of the solubility of gibbsite in Na-OH-NO_2 solutions using the Na-OH, Na-NO_2, $NaNO_2$(aq)-OH, and Na-$Al(OH)_4$ parameters developed above are shown in Figures 3.28 through 3.31. These data were not available for earlier experiments, and so comparison with a Pitzer model is not possible at this time. The trends and level of agreement with experimental data are qualitatively similar to the case of nitrate.

3.5.4 The Aqueous System: Na-OH-$Cr(OH)_4 \pm$ NO_3

As shown in Figure 3.32, the solubility of $Cr(OH)_3$ in NaOH is qualitatively similar to gibbsite at low molality (below about 2 molal). However, at higher hydroxide concentrations, the molality of $Cr(OH)_4^-$ rises more rapidly than in the case of gibbsite. Although various combinations of parameters were found that reproduced the available solubility data with approximately the same level of accuracy, we have chosen to model the Na-OH-$Cr(OH)_4$ system as an analog of the Na-OH-$Al(OH)_4$ system and to attribute differences at high hydroxide concentration to the formation of an ion pair ($NaCr(OH)_4$(aq)). Thus, the Na-$Cr(OH)_4$ interaction has the same Bromley parameters as Na-$Al(OH)_4$, and the curves in Figures 3.32 and 3.33 were produced by including the $NaCr(OH)_4$(aq) ion pair and adjusting its chemical potential to achieve the best possible fit. The solubility of $Cr(OH)_3$ in NaOH-$NaNO_3$ solutions is more strongly dependent on the molality of NO_3^- than is gibbsite.

3.5.5 The Aqueous System: $Na \pm$ $OH \pm$ $NO_3 \pm$ NO_2

An important subset of our major electrolyte model with respect to the Hanford wastes is the Na-OH-NO_3-NO_2 system. Data for the three most concentrated mixed systems were selected for study. These systems are the $NaNO_3$-$NaNO_2$-H_2O system, which reaches concentrations as high as 36 molal at 100°C (Figure 3.34); the $NaNO_3$-NaOH-H_2O system (Figure 3.35); and the $NaNO_2$-NaOH-H_2O system (Figure 3.36). Our predictions are in good agreement with experimental data, even to very high ionic strengths. For the $NaNO_3$-NaOH-H_2O system, the binary model was only qualitatively correct. As in earlier experiments, we introduced a $\lambda_{OH\text{-}NaNO3}$ to obtain a better fit. Also shown in these figures are the predictions using "off the shelf" ESP parameters. It is clear that our revised ESP parameters, based on the osmotic and solubility data to high ionic strength, represent a considerable improvement over the standard ESP parameters.

3.6 Conclusions and Recommendations

The evidence presented above generally supports the use of the ESP electrolyte model for process simulation to aid in development of tank waste remediation strategies. For the NaF, NaOH, Na_2SO_4, $NaNO_3$, $NaNO_2$, Na_2CO_3, $NaAl(OH)_4$, and $NaCr(OH)_4$ binary systems, it was possible to obtain acceptable fits to osmotic and/or solubility data. We have also improved the ESP model for Na_3PO_4. When revised parameters, fit from binary data on high ionic strength systems, are incorporated into the model, ESP accurately predicts the behavior of the $NaNO_3$-$NaNO_2$-H_2O, $NaNO_3$-NaOH-H_2O, $NaNO_2$-NaOH-H_2O, $NaNO_3$-NaOH-$Al(OH)_3$, $NaNO_2$-NaOH-$Al(OH)_3$, and $NaNO_3$-NaOH-$Cr(OH)_3$ mixed systems. We emphasize the importance of using experimental data at high ionic strengths to develop ESP parameters suitable for process simulation of tank brines, and caution strongly against using the standard parameters valid only at low ionic strengths.

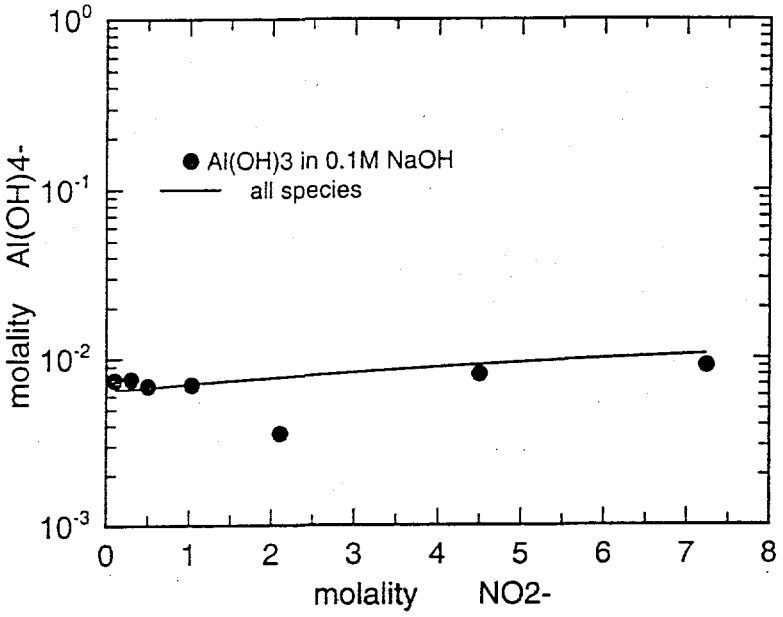

Figure 3.28. Solubility of Gibbsite in Na-NO_2-OH Solution at 0.1 M NaOH and 25°C. Solid circles represent earlier experimental data; solid line represents the fit to these data using ESP parameters derived in this work (Table 3.1).

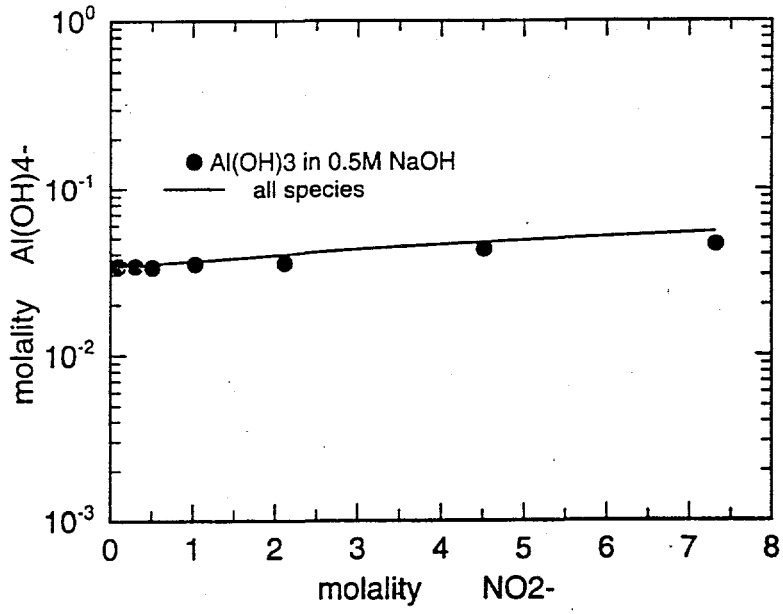

Figure 3.29. Solubility of Gibbsite in Na-NO_2-OH Solution at 0.5 M NaOH and 25°C. Solid circles represent earlier experimental data; solid line represents the fit to these data using ESP parameters derived in this work (Table 3.1).

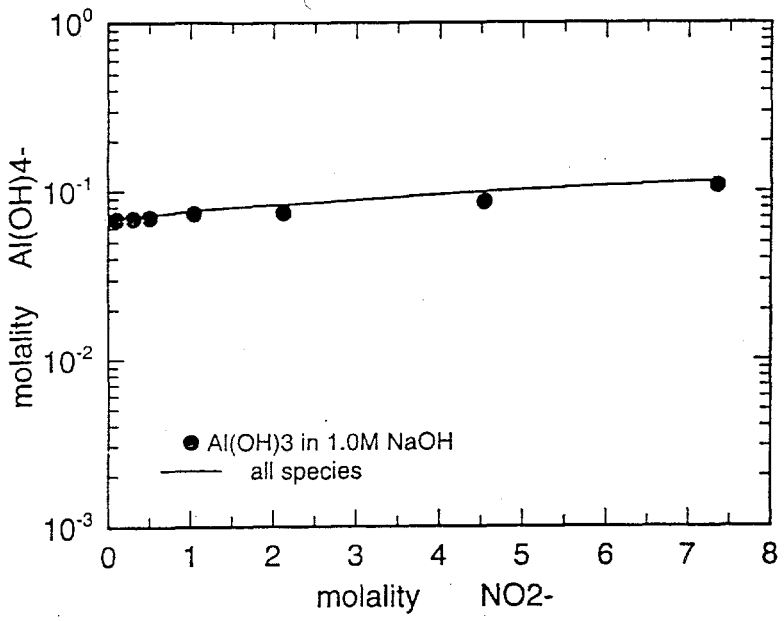

Figure 3.30. Solubility of Gibbsite in Na-NO_2-OH Solution at 1.0 M NaOH and 25°C. Solid circles represent earlier experimental data; solid line represents the fit to these data using ESP parameters derived in this work (Table 3.1).

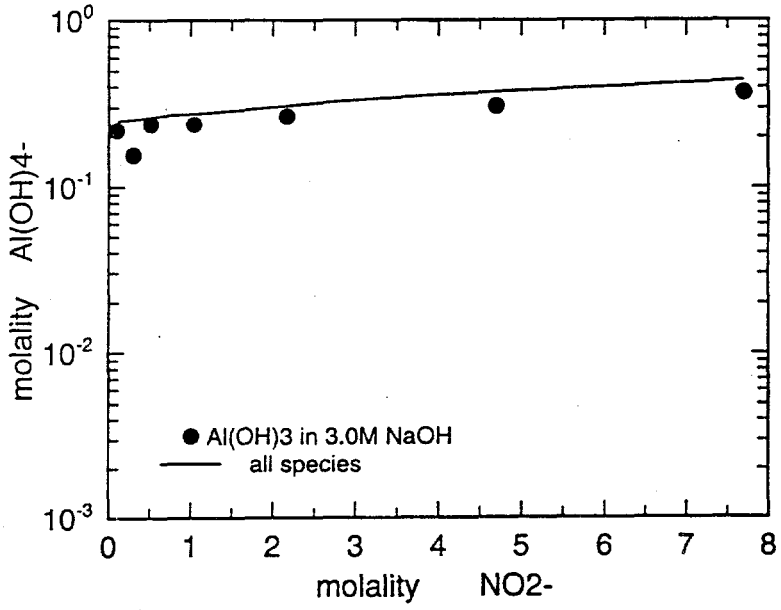

Figure 3.31. Solubility of Gibbsite in Na-NO_2-OH Solution at 3.0 M NaOH and 25°C. Solid circles represent earlier experimental data; solid line represents the fit to these data using ESP parameters derived in this work (Table 3.1).

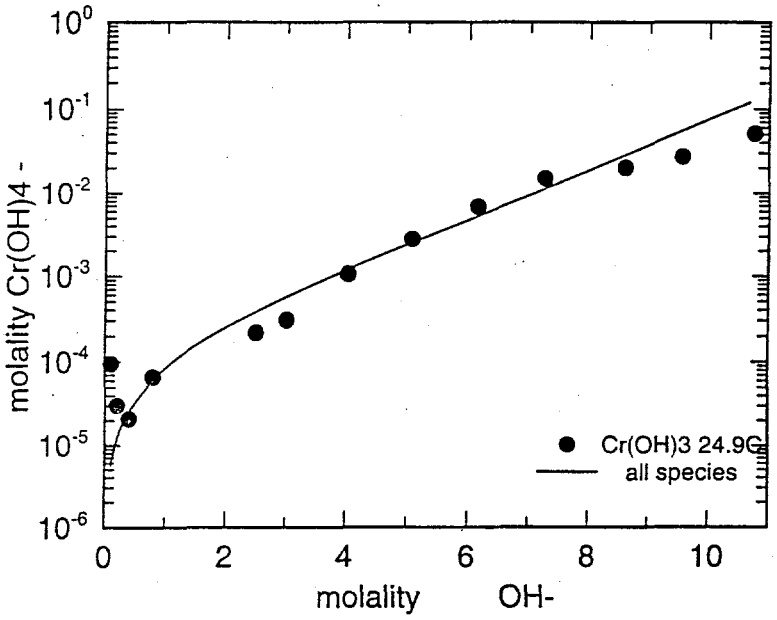

Figure 3.32. Solubility of Chromium(III) Hydroxide in Sodium Hydroxide Solution at 25°C. Solid circles represent earlier experimental data; solid line represents the fit to the data using ESP parameters derived in this work (Table 3.1).

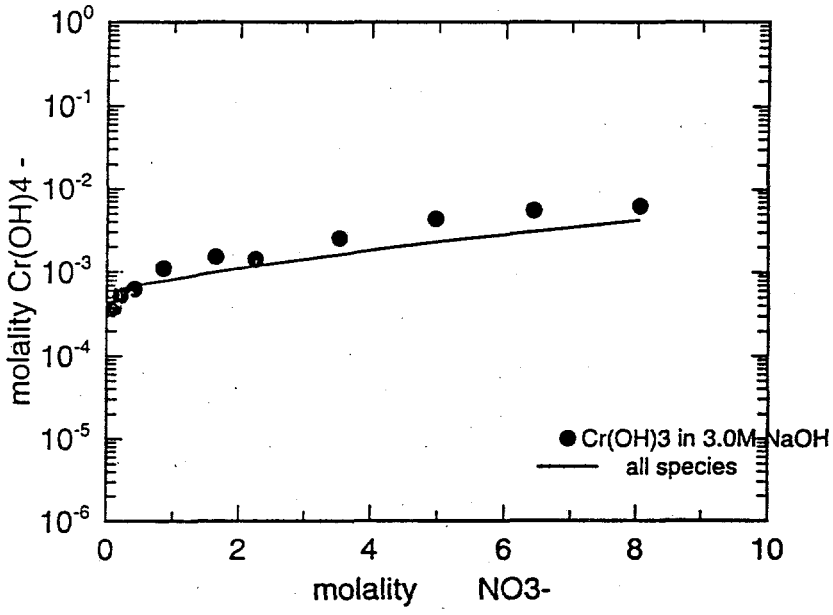

Figure 3.33. Solubility of Chromium(III) Hydroxide in Na-NO_3-OH Solution at 3 M NaOH and 25°C. Solid circles represent earlier experimental data; solid line represents the fit to the data using ESP parameters derived in this work (Table 3.1).

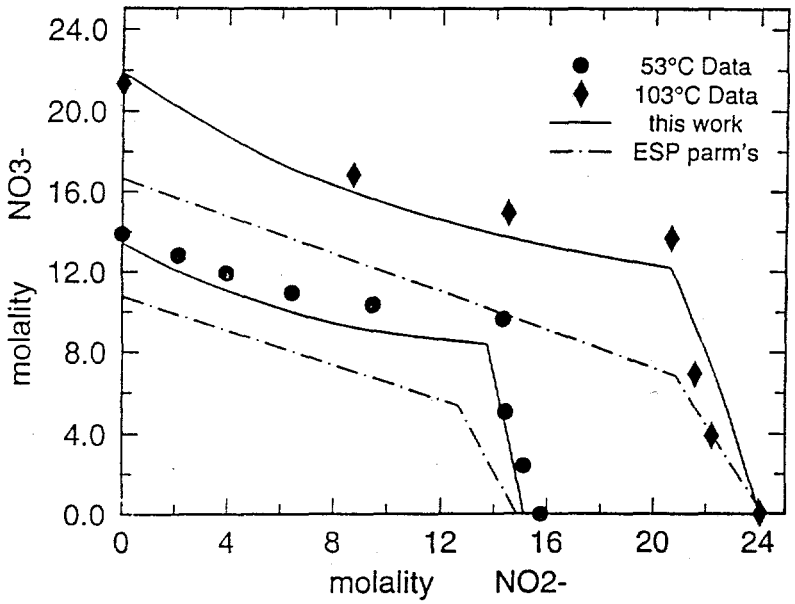

Figure 3.34. Ternary Solubility Data (filled circles) at 52°C and 103°C. Solid line shows current model predictions, and dashed line shows predictions using the standard ESP parameters.

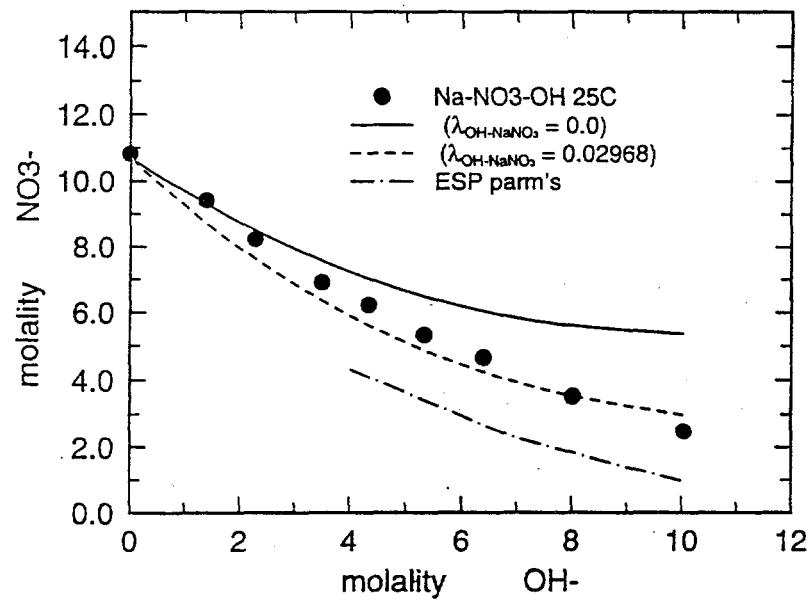

Figure 3.35. Ternary Solubility Data for $NaNO_3$ in NaOH Solution (filled circles) at 25°C. Solid line shows model prediction for using only the binary data. The dashed line shows the model fit using a nonzero $\lambda_{OH-NaNO3}$, and the dot-dashed line shows predictions using the standard ESP parameters.

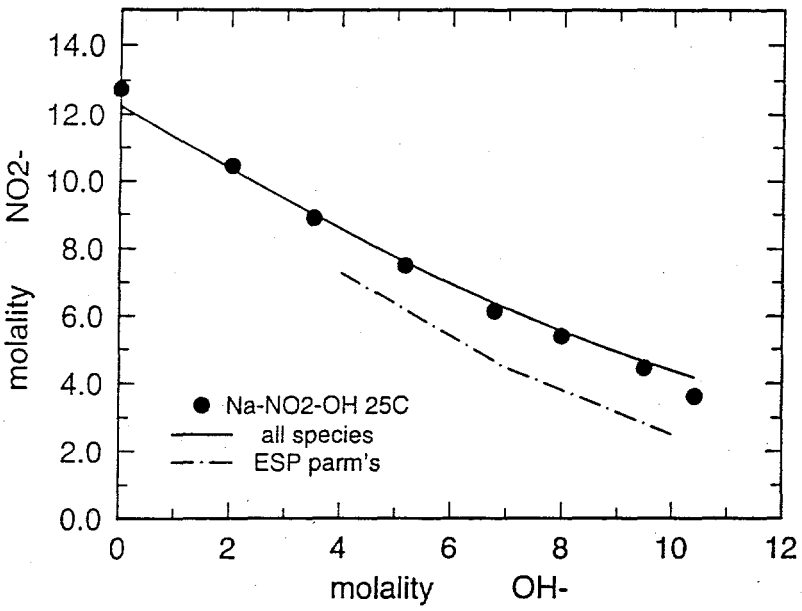

Figure 3.36. Ternary Solubility Data for $NaNO_2$ in NaOH Solution (filled circles) at 25°C. Solid line shows current model predictions, and dot-dashed line shows predictions using the standard ESP parameters.

3.7 References

Ananthaswamy, J., and G. Atkinson. 1985. "Thermodynamics of Concentrated Electrolytes. 5. A Review of the Thermodynamics Properties of Aqueous Calcium Chloride in the Temperature Range 273.15-373.15 K." *J. Chem. Eng. Data* 30:120-128.

Bromley, L. A. 1973. "Thermodynamic Properties of Strong Electrolytes in Aqueous Solution. *AIChE Journal* 19:313-320.

Greenberg, J. P., and N. Møller. 1989. "The Prediction of Mineral Solubilities in Natural Waters: A Chemical Equilibrium Model for the Na-K-Ca-Cl-SO_4-H_2O System to High Concentration from 0 to 250°C." *Geochim. Cosmochim. Acta.* 53:2503-2518.

Grotheim, K., W. Voigt, B. Haugsdal, and A. Dittrich. 1988. *Acta Chem. Scand. Se. A.* 42:470.

Linke, W. F. 1965. *Solubilities of Inorganic and Metal Organic Compounds.* Vol. 1 and 2. American Chemical Society.

Møller, N. 1988. The Prediction of Mineral Solubilities in Natural Waters: A Chemical Equilibrium Model for the Na-Ca-Cl-SO_4-H_2O System to High Temperature and Concentration." *Geochim. Cosmochim. Acta.* 52:821-837.

Pabalan, R. T., and K. S. Pitzer. 1987. "Thermodynamics of NaOH(aq) in Hydrothermal Solutions." *Geochim. Cosmochim. Acta.* 51:829-837.

Peiper, J. C., and K. S. Pitzer. 1982. "Thermodynamics of Aqueous Carbonate Solutions Including Mixtures of Sodium Carbonate, Bicarbonate and Chloride." *J. Chem. Thermodyn.* 14:613-638.

Pitzer, K. S. 1991. "Ion Interaction Approach: Theory and Data Correlation." In *Activity Coefficients in Electrolyte Solutions*, ed. K. S. Pitzer. CRC Press, 2nd edition, pp. 75-153.

Rard, J. A., and R. F. Platford. 1991. "Experimental Methods: Isopiestic." In *Activity Coefficients in Electrolyte Solutions*, ed. K. S. Pitzer. CRC Press, 2nd edition, pp. 209-277.

Robinson, R. A., and R. H. Stokes. 1959. *Electrolyte Solutions.* Butterworths.

Russell, A. S., J. D. Edwards, and C. S. Taylor. 1955. "Solubility and Density of Hydrated Aluminas in NaOH Solution." *J. Metals* 7:1123-1128.

Shpigel, L. P., and K. P. Mischenko. 1967. "Activities and Rational Activity Coefficients of Water in Potassium Nitrate and Sodium Nitrate at 1, 25, 50, and 75°C over a Wide Range of Concentration." *Zh. Prikl. Khimii* 40:680-683.

Wesolowski, D. J. 1992. "Aluminum Speciation and Equilibria in Aqueous Solution: I. The Solubility of Gibbsite in the System Na-K-Cl-OH-$Al(OH)_4$ from 0 to 100°C." *Geochim. et Cosmochim. Acta.* 56:1065-1091.

Wu, Y. C., and W. J. Hamer. 1980. "Revised Values of the Osmotic Coefficients and Mean Activity Coefficients of Sodium Nitrate in Water at 25°C." *J. Phys. Chem. Ref. Data* 9:513-518.

4.0 Sludge Characterization Studies

Jun Liu, Larry E. Thomas, Yuan L. Chen, and Li-Qiong Wang

The objectives of this subtask are to identify the major solid phases present in sludge; to determine how radionuclides are partitioned among the observed phases; to characterize the ion exchange, colloidal chemistry, and dissolution behavior of phases during sludge processing; and to use the resulting database on sludge chemistry to help evaluate existing sludge pretreatment technologies and develop new sludge pretreatment schemes. Work within this subtask is focused on analyzing both tank and simulated wastes using techniques such as transmission electron microscopy (TEM), scanning electron microscopy (SEM), x-ray diffractometry (XRD), and nuclear magnetic resonance (NMR). TEM analyses provide structural and morphological information on the angstrom scale and compositional information on the sub-nm scale (to 1 nm). SEM analyses provide morphological and compositional information on a larger (micrometer) scale. XRD provides bulk information about the crystalline phases, and NMR analyses of simulated wastes provide additional insight into the chemistry and chemical reactions of tank wastes.

During the third quarter, characterization and analysis of sludge samples from Tanks T-111, BX-107, T-104, S-104, and B-111, including washed samples and residual solids, was completed. The results from these analyses are summarized in Table 4.1 and are discussed in the following sections, along with results from FY 1994 on other tanks.

4.1 Aluminum

Aluminum is an important component in S-104, T-104, BX-107, C-112, SY-103 and 101-SY wastes. It exists in different forms, and the solubility and physical behavior of these wastes appear to be directly related to the aluminum phases.

Boehmite [AlOOH]: The dominant phase in S-104 consists of boehmite platelets that are about 1 μm wide. This would be expected since S-104 was a boiling tank, and boehmite tends to form at high temperatures. The dissolution kinetics for boehmite are slower than for gibbsite, and the majority of the boehmite particles in the S-104 sample were not removed by washing and leaching (Figure 4.1). Boehmite is also known to have a low sedimentation density.

Aluminum hydroxide [$Al(OH)_3$]: Most of the aluminum in C-112 waste is in the form of rectangular gibbsite rods that are longer than 5 μm (Figure 4.2A). These gibbsite particles dissolved during washing (Figure 4.2B). Aluminum hydroxide is also observed in SY-103; however, this $Al(OH)_3$ does not have a well-defined morphology (Figure 4.3). Amorphous $Al(OH)_3$ is observed in T-104 and BX-107 samples. It exists as aggregates of small particles (10 nm). The amorphous $Al(OH)_3$ is removed by washing and leaching (Figure 4.4A).

Amorphous aluminum phosphate [$AlPO_4$]: Amorphous aluminum phosphate particles are observed in T-104 and BX-107 samples (Figure 4.4B). These particles do not have a well-defined morphology and are dissolved by washing and leaching.

Table 4.1. Distribution of Major Phases

Aluminum					
$Al(OH)_3$ (soluble)	**$AlPO_4$ (soluble)**	**AlOOH (slow kinetics)**	**Amorphous aluminosilicate (insoluble)**	**Crystalline aluminosilicate (insoluble)**	**Sodium aluminate (soluble)**
BX-107 C-112 T-104 105-AW 103-SY	BX-107 T-104	C-112 S-104	BX-107 T-104	B-111 (trace) BX-107 C-112 (trace) T-104 105-AW (trace)	101-SY

Iron	
Iron bismuth silicate hydroxide (insoluble)	**Amorphous iron hydroxide (insoluble)**
B-111 BX-107 T-104 T-111	B-111 BX-107 C-112 T-104 T-111 105-AW (trace)

Phosphate			
Sodium phosphate (soluble)	**Calcium phosphate (insoluble)**	**$AlPO_4$ (soluble)**	**$La(P_2O_7)_3$ (insoluble)**
B-111 BX-107 C-112 T-104	C-112 T-111 (HAP)	BX-107 T-104	T-111

Chromium		
3^+ with $Al(OH)_3$	**3^+ with $Fe(OH)_3$**	**6^+ (?) with bismuth oxide**
101-SY	BX-107 T-104 T-111	B-111

Other Minor Phases
(mostly insoluble)
Bi_2O_3, Fe_2MnO_4, goethite, $UO_x(OH)_y$, bismuth iron phosphate

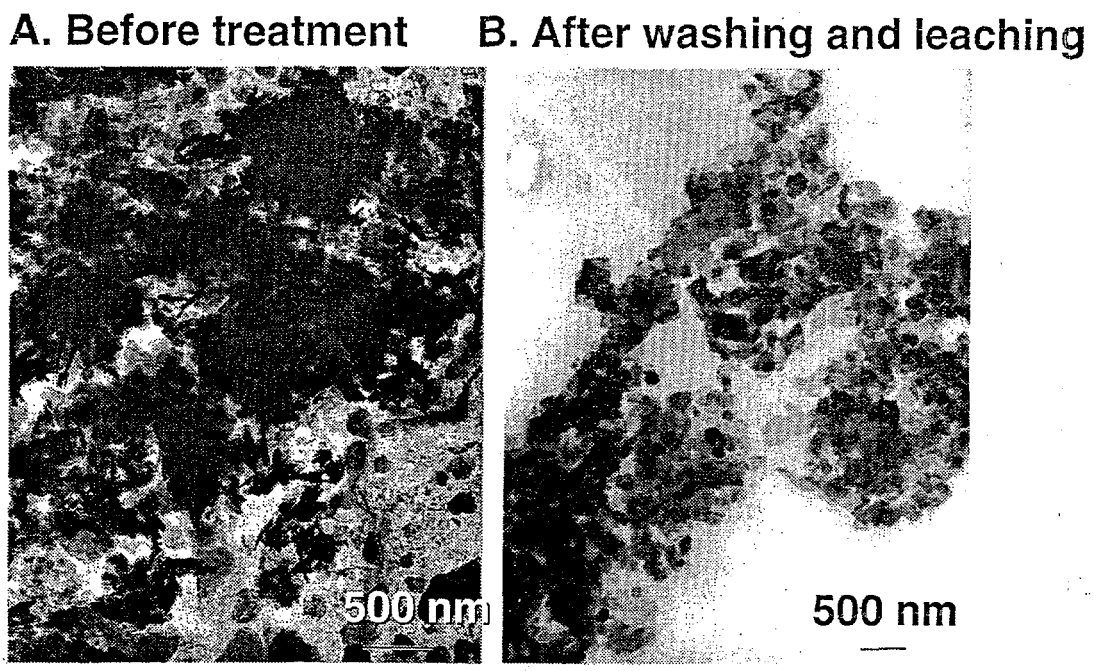

Figure 4.1. Boehmite Particles (AlOOH) in S-104 Waste Before (A) and After Washing and Leaching (B). Washing and leaching removed only the salt, not the boehmite.

4.2 Interaction of Silicon with Aluminum

Silicon in BX-107 and T-104 tank wastes has reacted with aluminum to form aluminosilicate species. These aluminosilicates are far less soluble than the pure aluminum hydroxide phases. A large amount of amorphous aluminosilicate is observed in BX-107 and T-104 samples (Figure 4.5). This phase does not have a well-defined morphology. Crystalline sodium aluminosilicate hydrate also is observed in T-104 waste (Figure 4.6), and another minor aluminosilicate phase, possibly cancrinite, is observed in B-111 waste.

4.3 Interactions Between Iron, Bismuth, and Silicon

In the bismuth-containing wastes (T-111, BX-107, T-104, and B-111), iron and silicon also are present. These three components tend to interact with one another to form an amorphous bismuth iron silicate hydroxide phase. The existence of this phase suggests that not all of the silicon in these wastes interacts with aluminum to form aluminosilicates. In some wastes, there is silicon in excess of the silicon contained in the bismuth iron silicate phase. This excess silicon appears to be dissolved by washing and leaching.

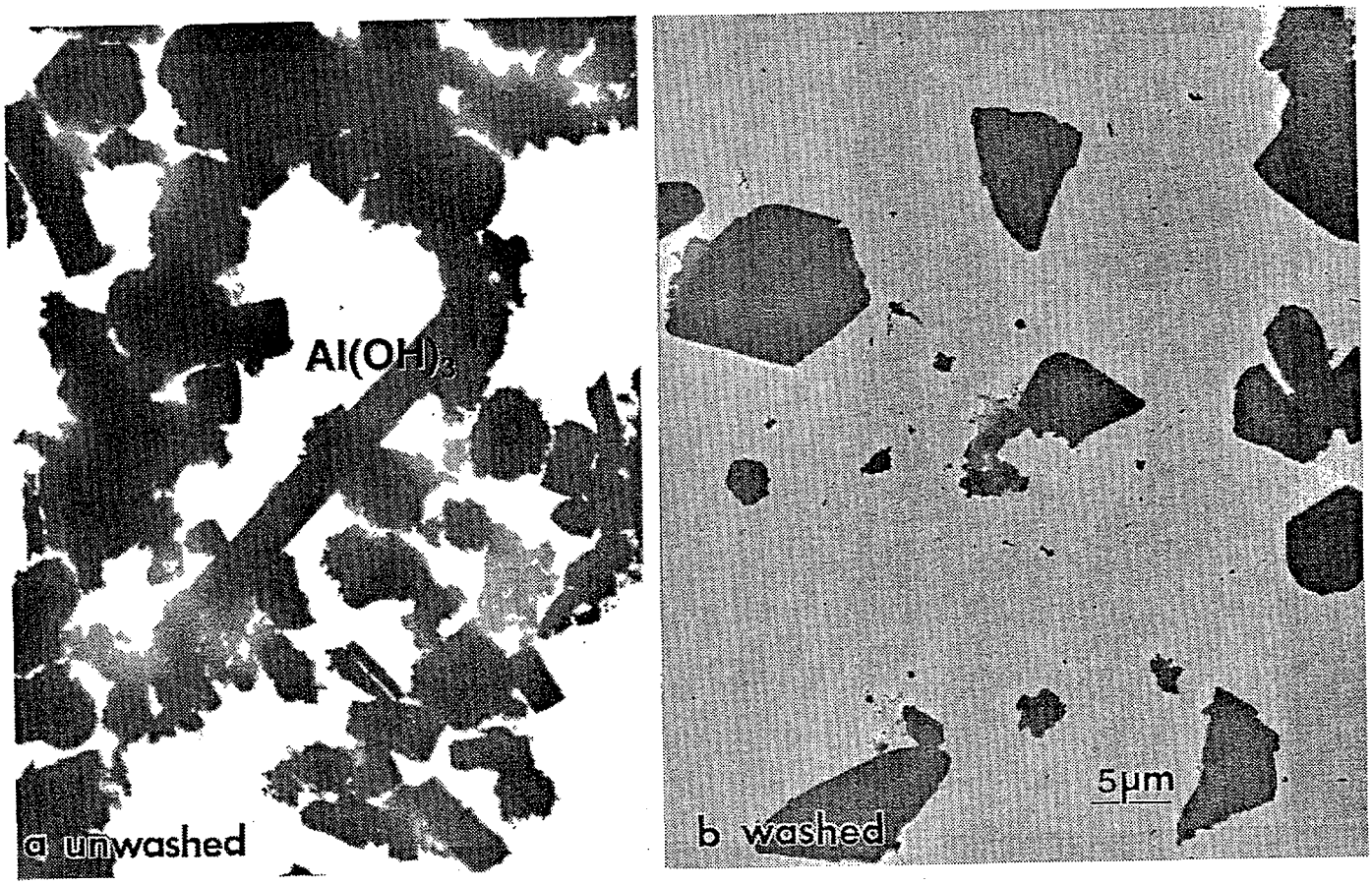

Figure 4.2. Gibbsite in C-112 Waste. The gibbsite (A) was removed by washing (B).

The bismuth iron silicate hydroxide phase consists of aggregates of very fine particles. The primary particles are < 10 nm, and the primary agglomerate size is < 100 nm (Figure 4.7). These materials are poorly crystalline, and the composition changes slightly from one area to another. A small amount of uranium is also detected in these regions. The diffraction pattern from these regions was not well defined, with only two rings identified. The peak positions do match those from bismuth ferrite [$Fe_2Bi(SiO_4)_2OH$], the only compound found in literature that contained iron, silicon, and bismuth; however, certain regions have better crystalline structures that appear to be closer to that of bismuth ferrite. Figure 4.8A shows the dark field of the bismuth iron silicate hydroxide phase. The uniform gray background is indicative of an amorphous structure. Figure 4.8B shows the bright field image.

Although the bismuth iron silicate is highly insoluble, washing and leaching caused the aggregate morphology to change. Before treatment, agglomerates (composed of primary agglomerates bound together by sodium salts) were > 100 μm in size. Washing and leaching caused the agglomerates to break into particles < 1 μm as shown in the SEM image in Figure 4.9. Analysis with TEM revealed even smaller aggregate sizes. Breakup of the agglomerates affects the sedimentation behavior of sludges; smaller particles and aggregates are difficult to settle.

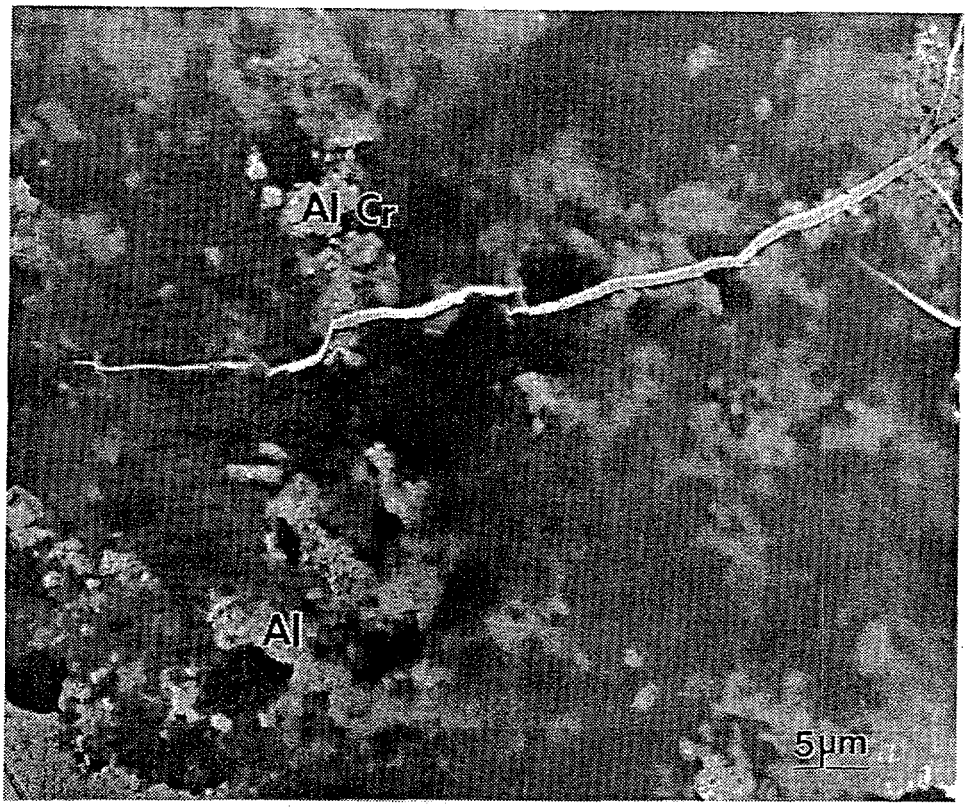

Figure 4.3. $Al(OH)_3$ in 103-SY Waste. The $Al(OH)_3$ contains chromium.

4.4 Phosphate

Sodium phosphate: A large amount of sodium phosphate salt exists in T-111, BX-107, T-104, and B-111 wastes. These salts should be water soluble; however, results from TEM studies suggest that sodium phosphate is still present in BX-107, T-104, and B-111 samples after leaching.

Calcium phosphate: Calcium phosphate is an important phase in C-112 waste (Figure 4.10A). This phase is sometimes found together with other phases such as nickel hydroxide (Figures 4.10B and 4.10C). The calcium phosphate is not soluble. Calcium phosphate in T-111 appears to be in the form of hydroxyapatite (HAP), which also is not soluble.

Other phosphate phases: Some phosphate is found with uranium-rich particles (Figure 4.11A). This phosphate dissolves with leaching, and the uranium particles break up into nm-sized particles (Figure 4.11B). A minor phase found in BX-107 is insoluble bismuth iron phosphate. Another minor phosphate phase, lanthanum phosphate, was observed in T-111. This insoluble phase is shown in Figure 4.12.

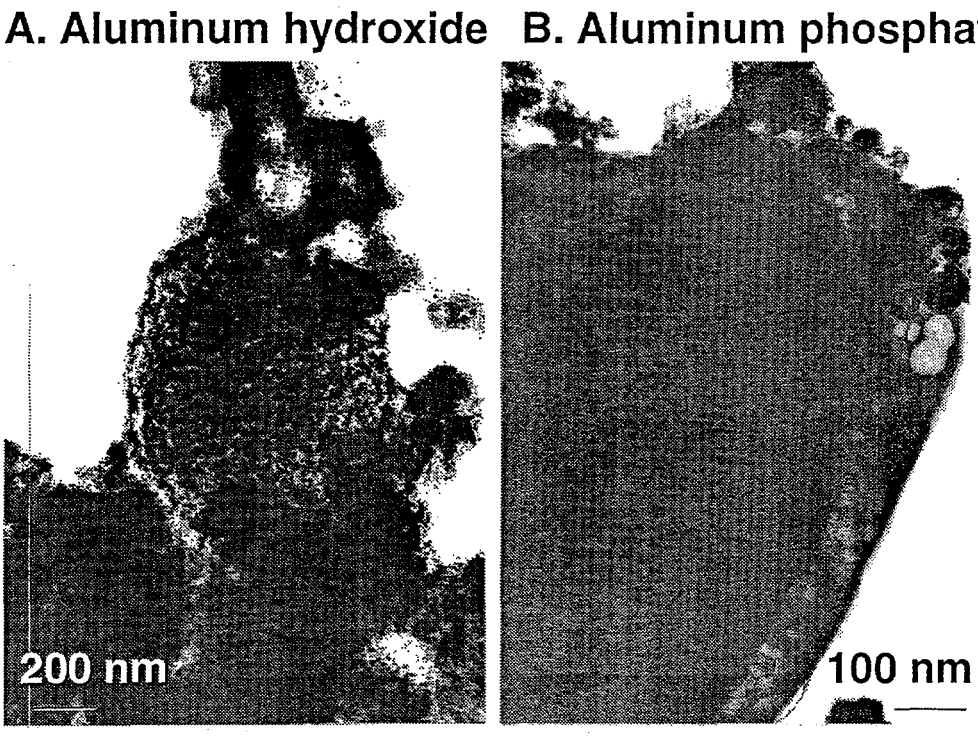

Figure 4.4. Amorphous $Al(OH)_3$ (A) and Aluminum Phosphate (B) in T-104 and BX-107 Wastes. These phases were removed by washing and leaching.

4.5 Chromium

Chromium in 103-SY waste appears to be associated with aluminum hydroxide (Figure 4.3) and should be in the 3+ state. In T-111, B-111, T-104, and BX-107 samples, a small amount of amorphous iron hydroxide doped with chromium is observed. The chromium in these samples also should be in 3+ state. This phase is not soluble. In BX-107, B-111, and T-111, bismuth oxide is found (Figure 4.13). The bismuth oxide in B-111 has been identified as $Bi_{38}CrO_{60}$ and suggests a small amount of chromium in the +6 state is present in this phase.

4.6 Summary

The results obtained from this characterization study are consistent with elemental analysis data and tank history information. These results support the dissolution and sedimentation behavior that has been observed in particular tank sludges. In addition, these results provide guidelines for developing sludge simulants that are used in colloidal studies.

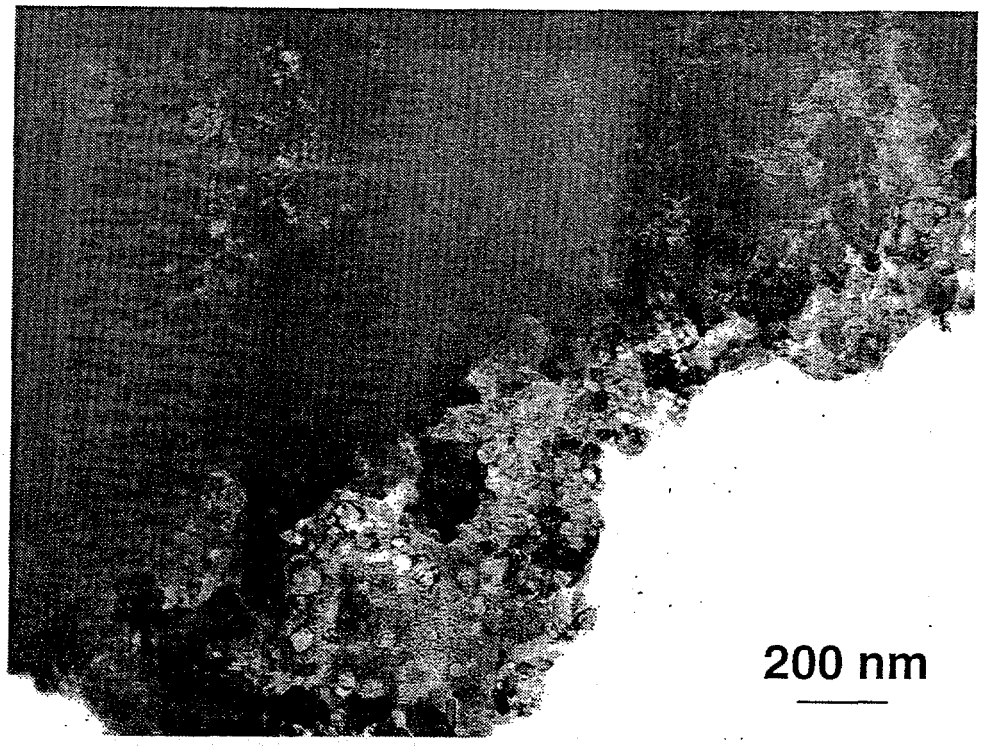

Figure 4.5. Amorphous Aluminosilicate in T-104 and BX-107 Wastes. This phase was not removed by washing and leaching.

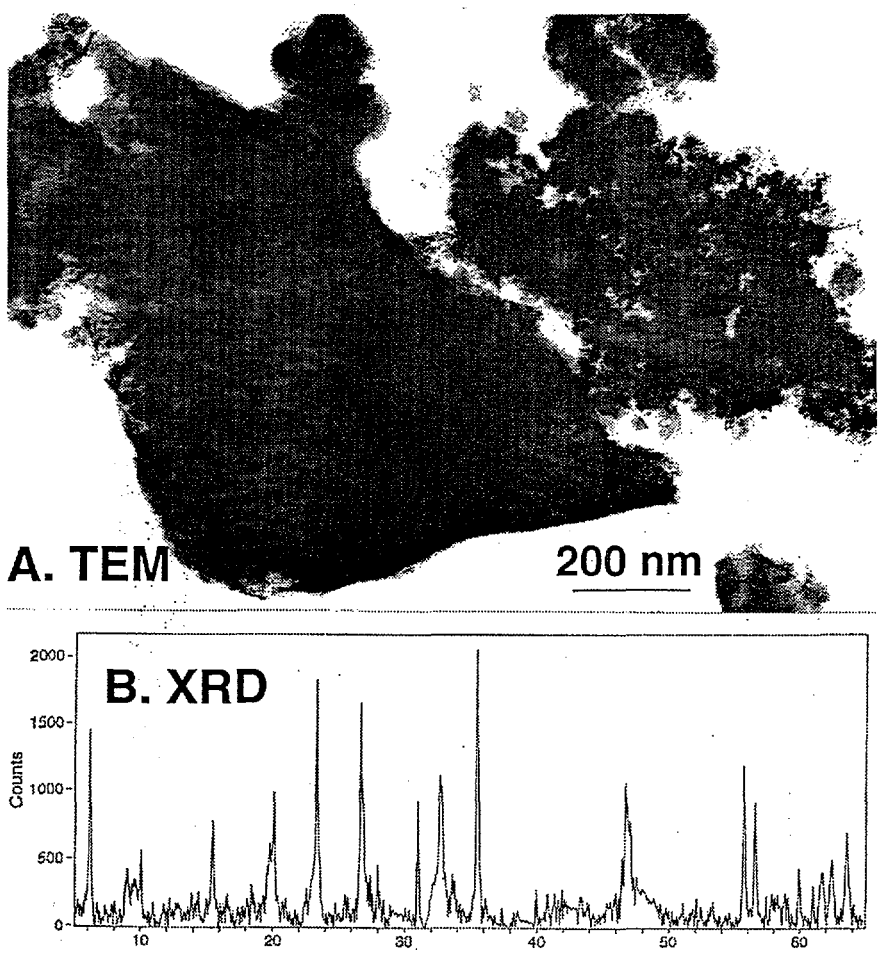

Figure 4.6. Sodium Aluminosilicate Hydrate in T-104. This phase is not soluble.

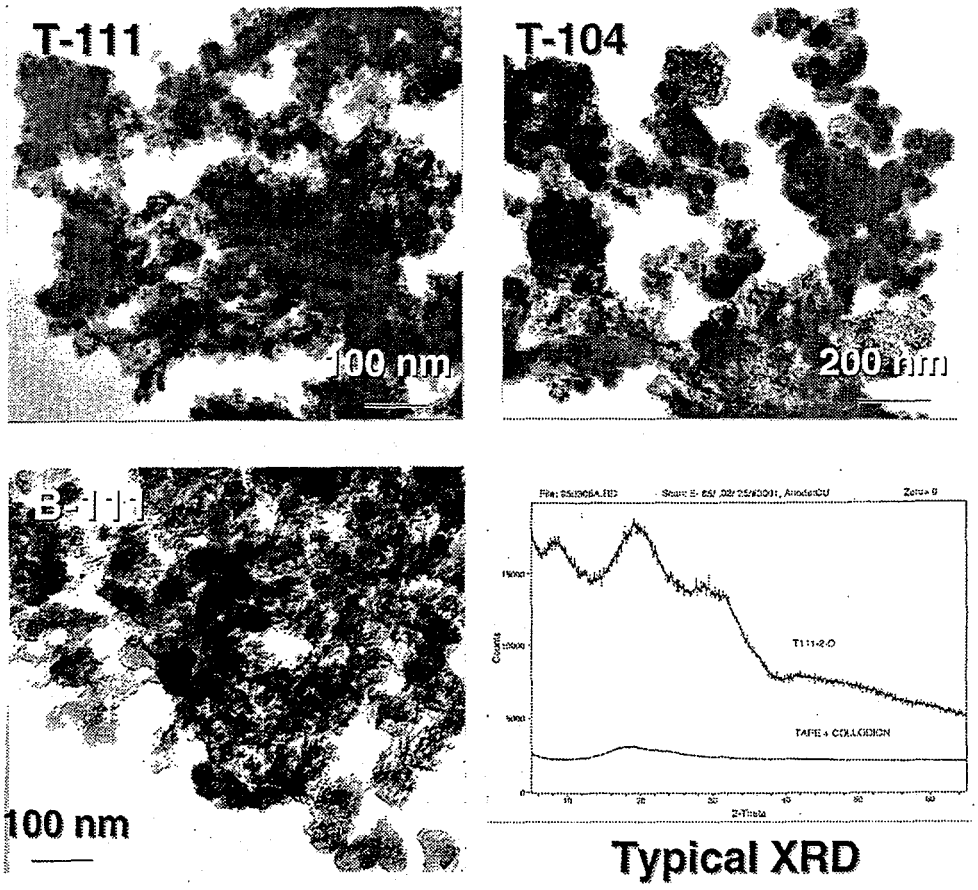

Figure 4.7. Typical Morphology of the Bismuth Iron Silicate Hydroxide in T-111, B-111, T-104, and BX-107 Wastes. These wastes have similar particle and agglomerate morphologies, with spherical primary agglomerates < 100 nm.

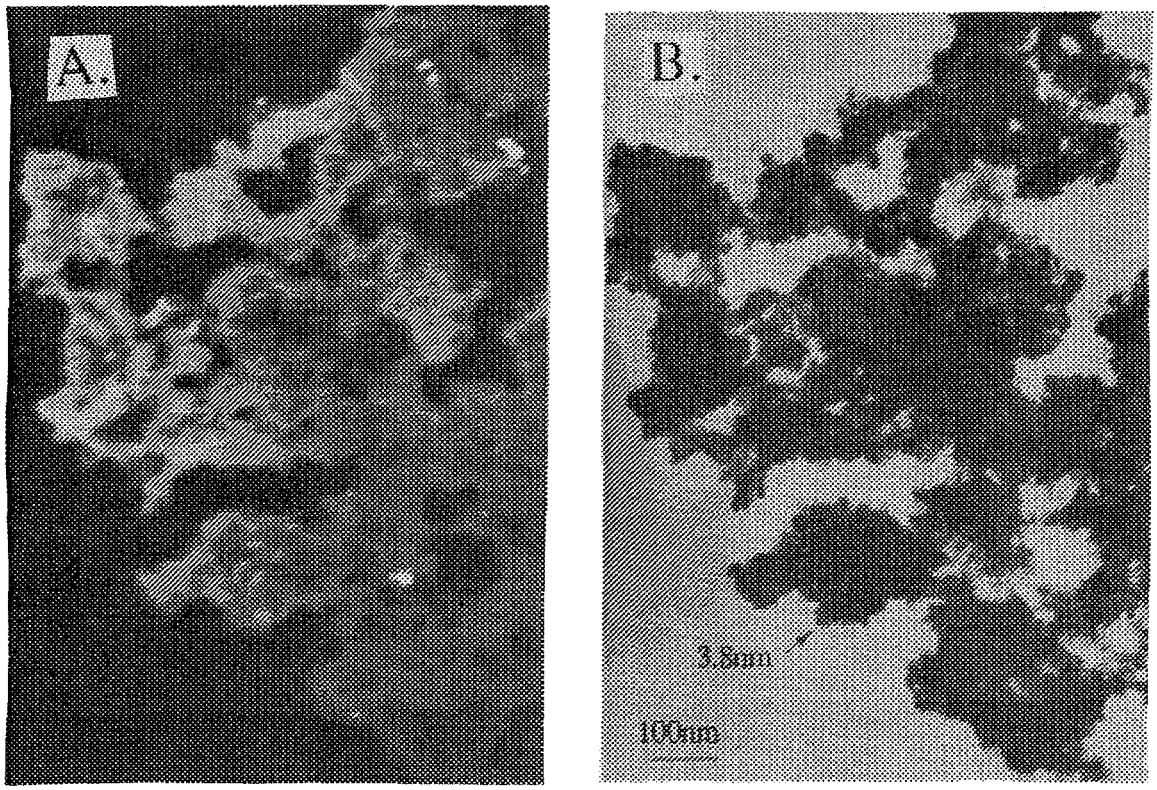

Figure 4.8. Bismuth Iron Silicate Hydroxide in the Bismuth-containing Tanks. Uniform gray background in the dark field image (A) indicates that it is not crystalline. Figure B shows the bright field.

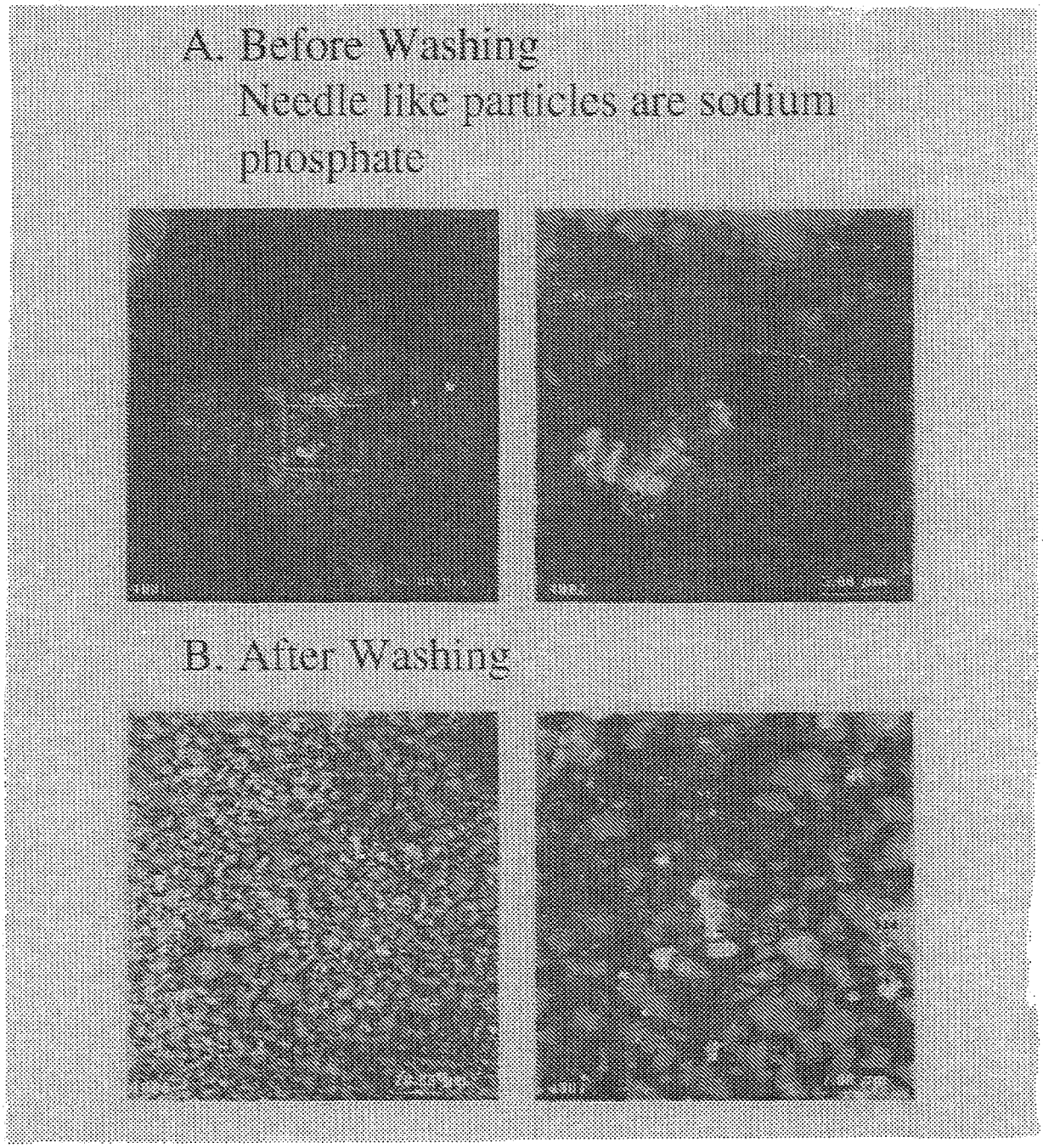

Figure 4.9. Effect of Washing and Leaching on the Bismuth Iron Silicate Phase. This phase is not soluble; however, washing and leaching caused the agglomerates to break up into aggregates < 1 μm.

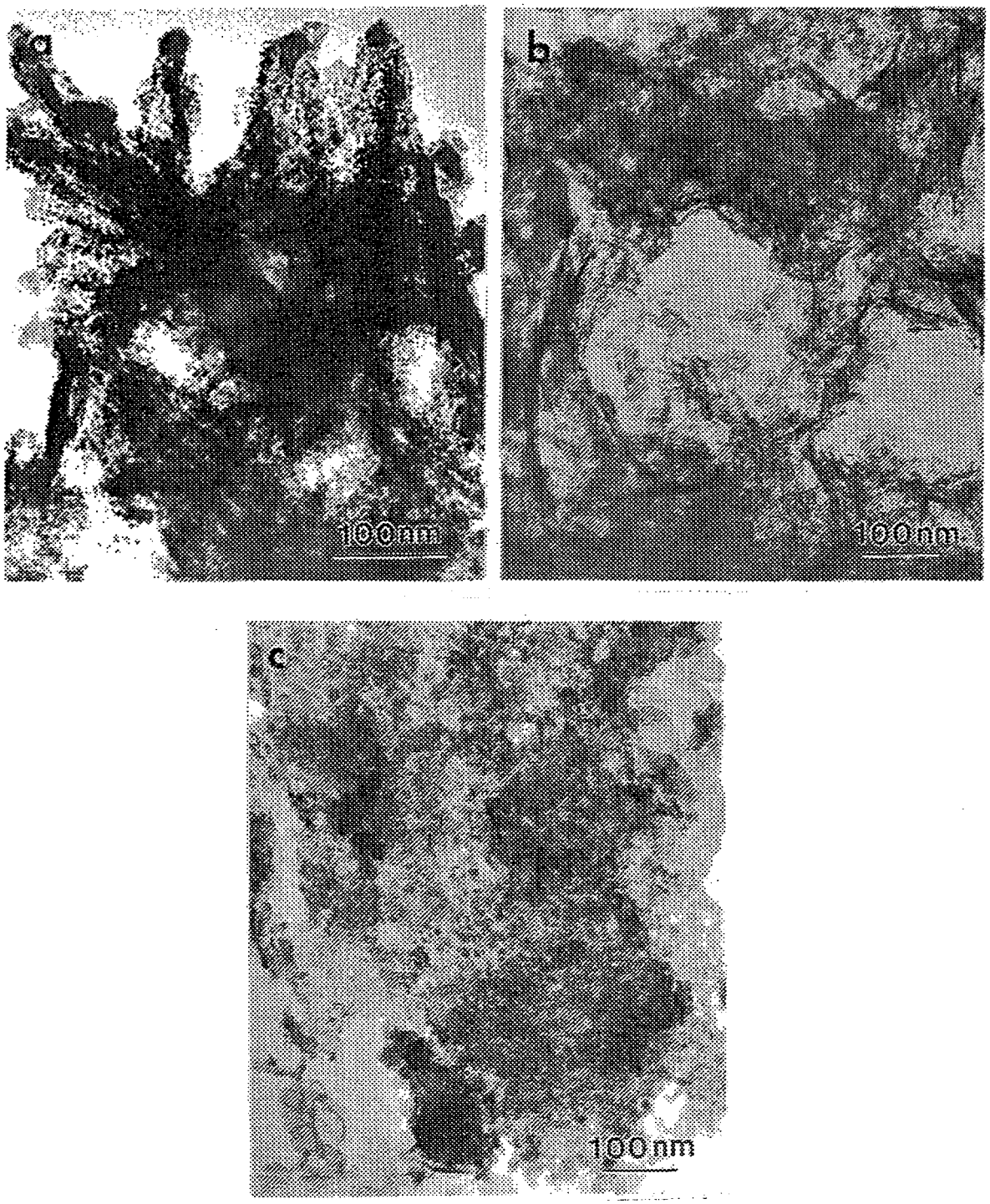

Figure 4.10. Insoluble Calcium Phosphate in C-112 Waste. Figures B and C show the calcium phosphate mixed with nickel hydroxide.

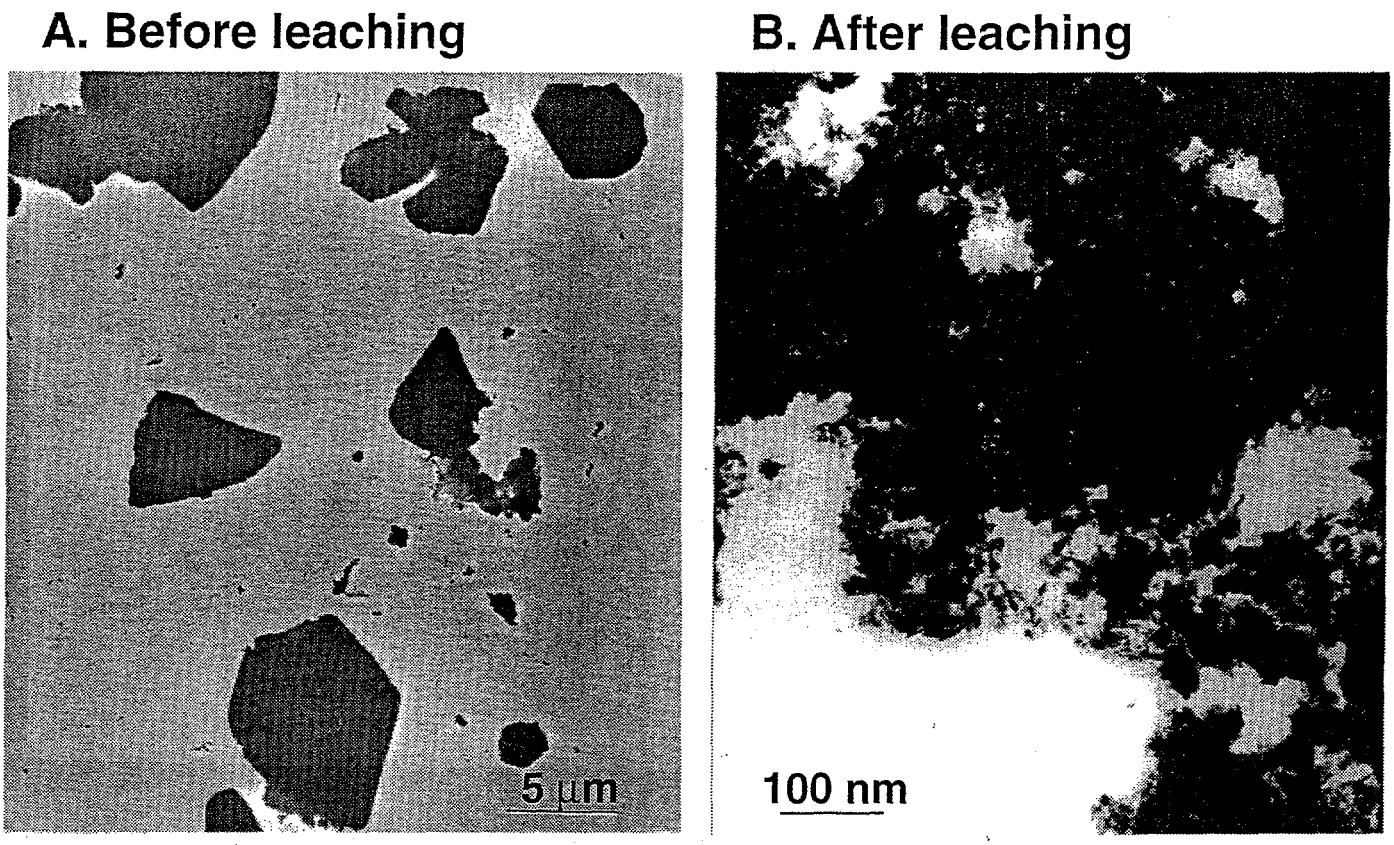

Figure 4.11. Phosphate Associated with Uranium-rich Particles in C-112 Waste (A). Leaching removed the phosphate and caused the particles to break up into nm-sized particles (B).

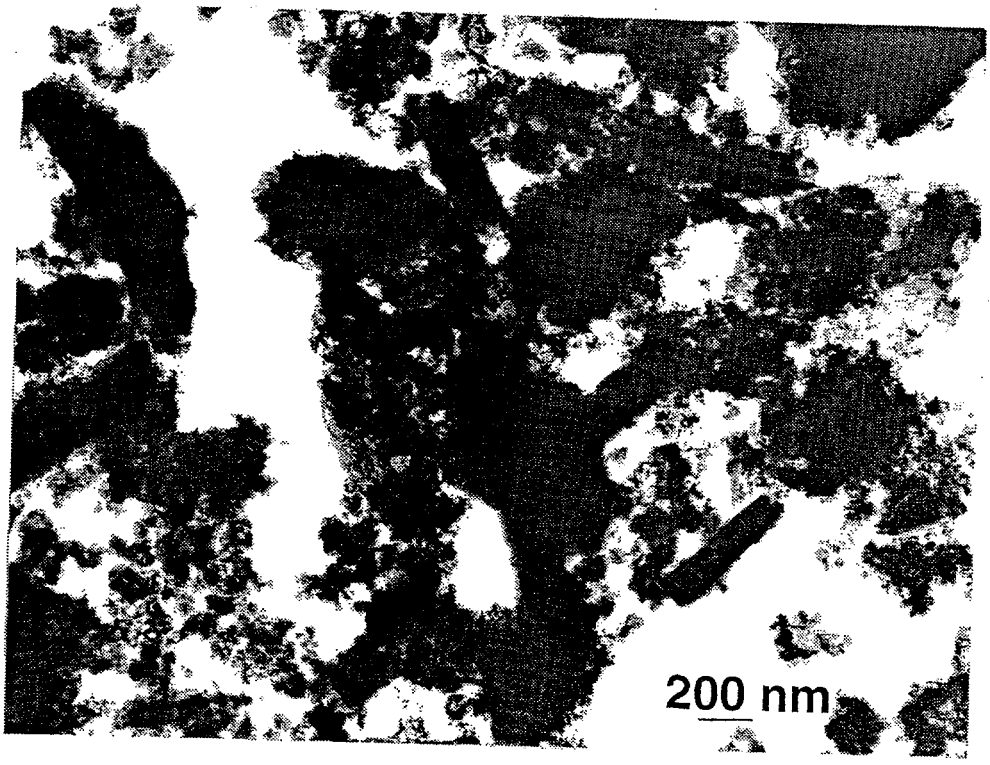

Figure 4.12. Insoluble Bismuth Iron Phosphate Found in BX-107.

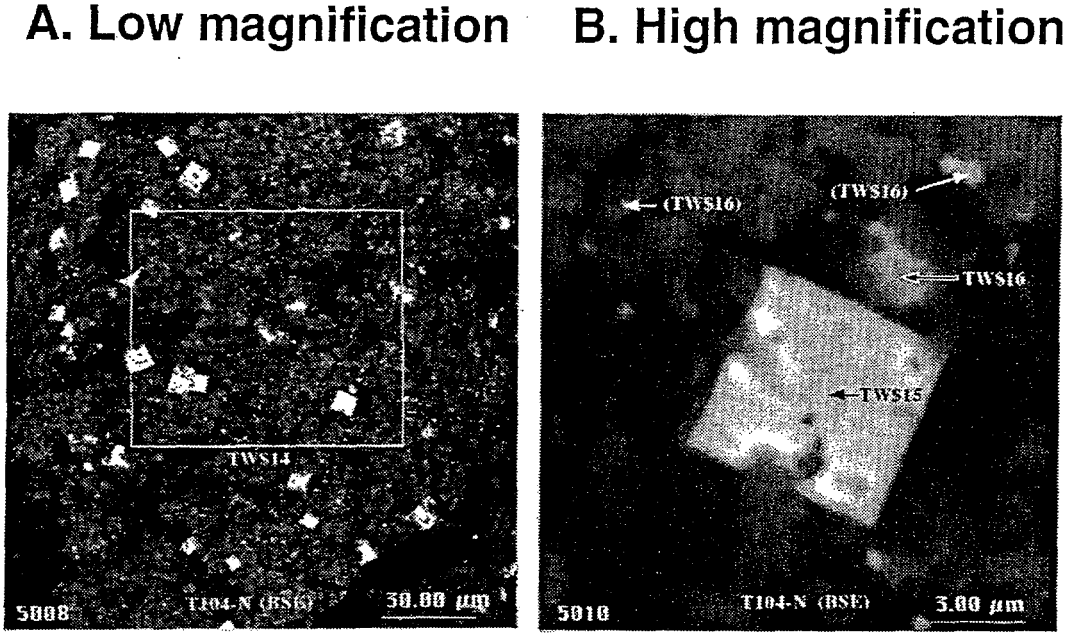

Figure 4.13. Bismuth Oxide Found in T-104, BX-107, and B-111 Wastes. Chromium is associated with some of the bismuth oxide ($Bi_{38}CrO_{60}$), although most of the Cr in these three wastes is associated with amorphous $Fe(OH)_3$.

5.0 Sludge Component Speciation

David L. Blanchard, Steven D. Conradson (LANL), Nigel G. Gotts, Nancy J. Hess, J. Craig Hutton, and Marc M. Lamoureux

The chemical speciation of sludge components is perhaps the single most important factor in determining how they will respond to any chemical processing. Chemical speciation is defined in this context as identification of the chemical compounds and phases and the *physical location*, e.g., co-precipitation versus precipitation in separate phases, or at the surface of another phase, etc., of sludge constituents. This detail is required because elemental information is not sufficient for predicting how a complex mixture will respond to a given treatment.

The purpose of this subtask is to provide data on the chemical speciation of specific components of tank wastes that are important to developing the pretreatment baseline. These data will allow prediction of how different tank wastes will respond to pretreatment processes, as well as assist in the interpretation of existing pretreatment process chemistry data. The following sections discuss the progress made during the third quarter on this subtask.

5.1 Chromium Speciation

Chromium in the feed stream to HLW vitrification may be a problem. The solubility limit in boro-silicate glass is roughly 0.5 to 1 wt%. Above this solubility limit, chromium forms spinel compounds and separates from the glass melt (M.L. Elliott and P.R. Hrma, PNL, personal communication), and the integrity of the resulting phase-separated glass is suspect. Enhanced sludge washing tests (washing with 0.01 M $NaNO_2$/0.01 M NaOH, leaching with 3 M NaOH, then washing again with 0.01 M $NaNO_2$/0.01 M NaOH), have shown that chromium removal varies greatly for different tank wastes, and even for different cores in the same tank. In some cases, a significant amount of chromium [ranging from ~0.5 wt% up to 22 wt% (B. M. Rapko, PNL, personal communication, data to be published)] is left in the undissolved solids that feed into the HLW stream. This may be cause for serious concern, particularly because waste from many of the tanks (approximately 165 of the 177) remain untested. The chromium species in the residual solids have not been identified.

Chromium removal by enhanced sludge washing was estimated for five tank wastes (Colton 1995) by assuming 75% of the water-insoluble chromium would dissolve during the caustic leach. This assumption is believed to be consistent with current systems engineering assumptions. Comparison of the calculated values with experimental data shows errors in the amount of chromium removed that range from 2% to 100%. In order to predict chromium removal with any accuracy, chemical information about the chromium is required. What is the ratio of Cr(III) to Cr(VI) in the various wastes? How much of each is removed by enhanced sludge washing? Is the chromium left behind found in pure phases, such as Cr_2O_3 and $Cr(OH)_3$; in minerals such as $FeCr_2O_4$; or coprecipitated in another phase, such as an oxide of iron, bismuth, or aluminum? The extent of chromium removal will be determined almost exclusively by these details.

5.1.1 Experimental

Due to analytical problems, samples originating from the TWRS Sludge Treatment Technology Task, were not available for x-ray absorption spectroscopy (XAS) experiments that were scheduled for

May 5 - 10, 1995. Performing these experiments within this time frame was important because of the limited amount of synchrotron beam time available. Therefore, fresh untreated samples of B-111, S-104, T-104 and T-111 wastes were removed from the hot cells, then washed and leached following an abbreviated version of the procedure used by the Sludge Treatment Technology Task. The sludge washing and leaching procedure consisted of a wash with 0.01M NaOH/0.01M $NaNO_2$, two leaches (3M NaOH), and three washes (same as first wash). Chromium and manganese K edge XAS data were collected on the samples at the Stanford Synchrotron Radiation Laboratory (SSRL). The preliminary analysis of the data is discussed below.

5.1.2 Results

An XAS spectrum may be divided into two regions for analysis. The first region comprises the spectrum roughly 50 eV below to 100 eV above the absorption edge. This is called the near-edge region, and is used for x-ray absorption near-edge spectroscopy (XANES). If only one or two species are present they can often be identified by features in the XANES region. XANES is particularly useful for identifying different oxidation states of an element. XANES of the chromium K edge from the tank samples was used in this quarter to make a preliminary determination of the Cr(III)/Cr(VI) ratio. The spectra were analyzed following the standard procedure of pre-edge background subtraction and normalization to the absorption step height (Sayers and Bunker 1988). The second region comprises the data at energies greater than roughly 50 eV above the absorption edge, and is used for extended x-ray absorption spectroscopy (EXAFS). The analysis of the EXAFS is still in progress and will be only briefly discussed in this report.

A pre-edge feature in the Cr(VI) XANES region may be used to determine the amount of Cr(VI) present in a sample (Bajt et al. 1993). The pre-edge is the region at lower energy than the absorption edge. Figure 5.1 shows the XANES for a Cr(VI) standard ($K_2Cr_2O_7$) and a Cr(III) standard (Cr_2O_3). (These data were taken during the previous quarter.) The feature, a peak at 5993 eV, is apparent in the Cr(VI) spectrum and absent from the Cr(III) spectrum.

Figure 5.2 shows the chromium K edge XANES for the untreated and treated samples of T-104 waste. The presence of the pre-edge peak and the shape of the spectrum above the absorption edge jump reveal the presence of Cr(VI) in the untreated sample. In sharp contrast to that, the treated sample appears to have little or no Cr(VI). All untreated samples tested contained Cr(VI). All treated samples had insignificant amounts of Cr(VI).

The Cr(VI) pre-edge peak was fit using a linear combination of the spectra from the Cr(VI) and Cr(III) standards. Two assumptions are implicit in this procedure:

1. The pre-edge peak of the Cr(VI) present in the tank samples is identical to the pre-edge peak of the Cr(VI) standard.

The pre-edge peak represents an electronic transition that is partially allowed due to the tetrahedral coordination of the Cr(VI) (Bianconi 1988; Durham 1988). Because first shell coordination of Cr(VI) by oxygen is tetrahedral (Cotton and Wilkinson 1988), and because this region of the spectrum is largely unperturbed by the structure beyond the first coordination shell (Bajt et al. 1993; Waychunas 1987), this is a good assumption.

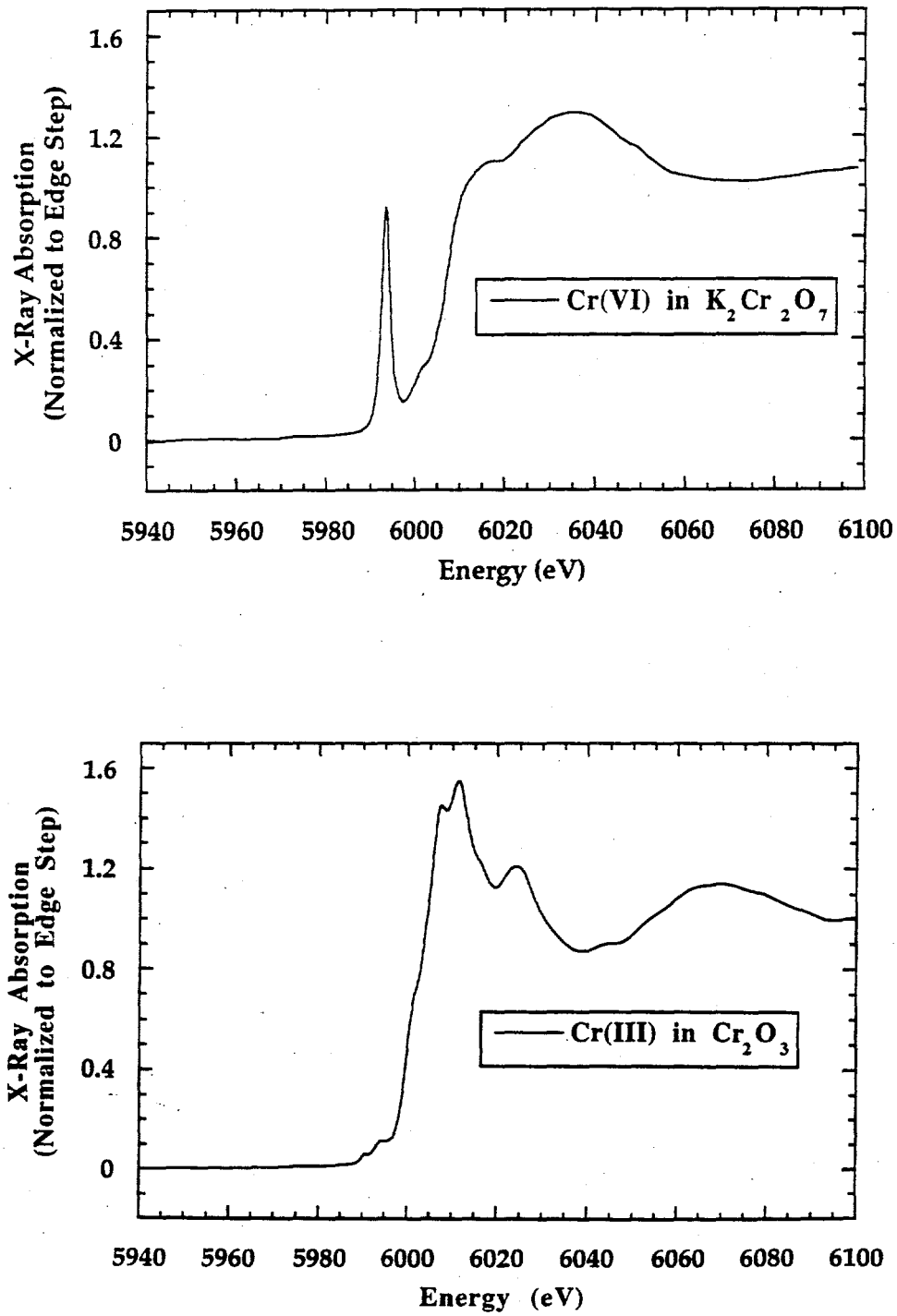

Figure 5.1. X-ray Absorption K Edge for a Cr(VI) Standard ($K_2Cr_2O_7$) and a Cr(III) Standard (Cr_2O_3). The pre-edge peak at 5993 eV in the Cr(VI) spectrum is used to determine the percentage of Cr(VI) in the tank waste samples.

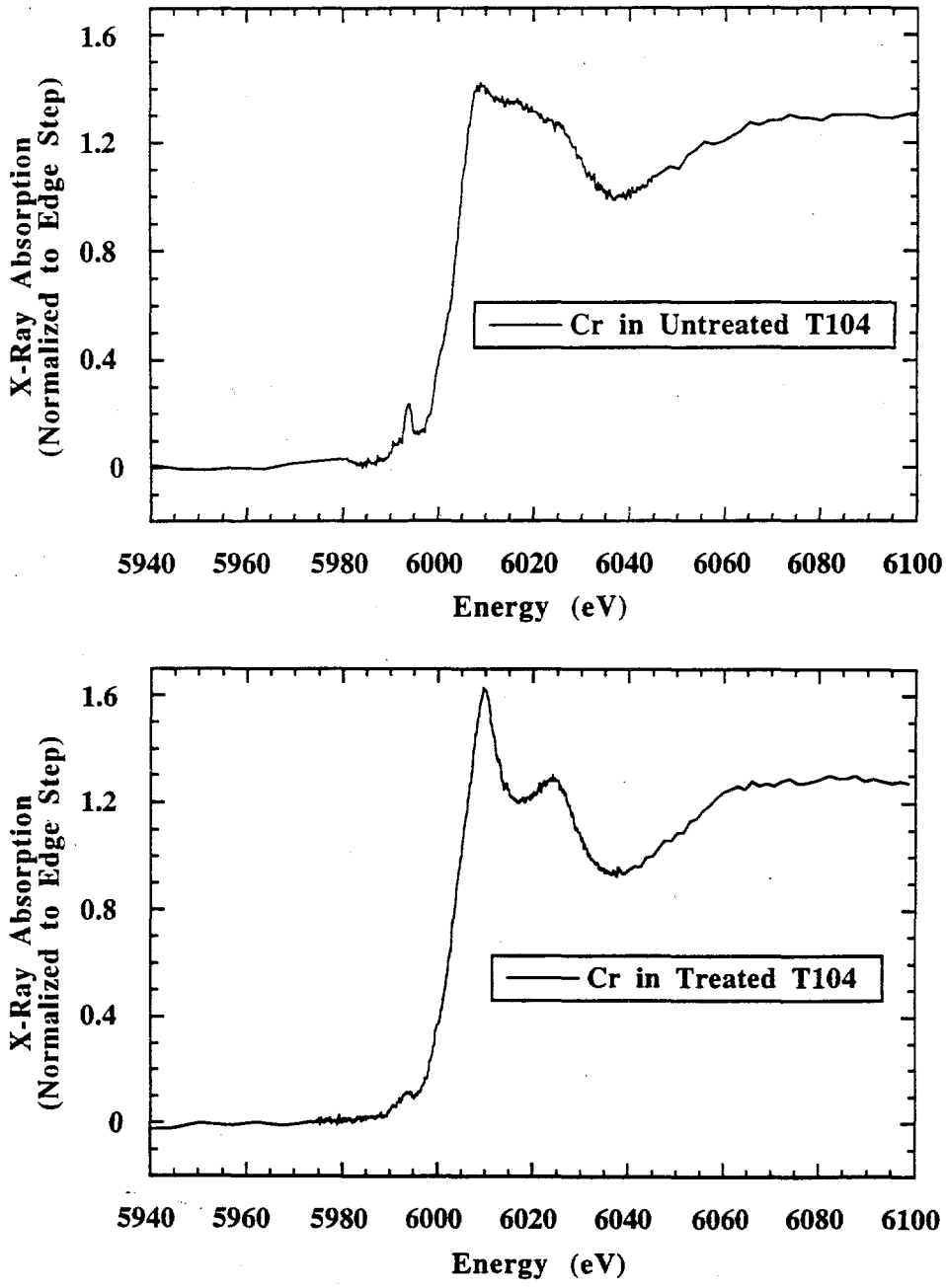

Figure 5.2. X-ray Absorption K Edge of Chromium for the Untreated and Treated Samples of T-104 Waste. The presence of the pre-edge peak and the shape of the spectrum above the absorption edge jump reveal the presence of Cr(VI) in the untreated sample. In contrast, the treated sample appears to have little or no Cr(VI).

2. In the region of the Cr(VI) pre-edge peak, the spectra of all chromium species other than Cr(VI) look the same as the Cr(III) spectrum.

Cr(III) ions are octahedrally, not tetrahedrally, coordinated in compounds reasonably expected to be in tank waste (Cotton and Wilkinson 1988). Therefore, XAS spectra of the Cr(III) species are expected to have little or no structure in this region. The +VI and +III oxidation states are expected to be dominant for chromium in tank waste. Therefore (2) is a good assumption.

Because of these assumptions, the error in the percentages of Cr(VI) and Cr(III) determined using this method must be estimated at +/- 10%. The spectra are being fit using a more rigorous method that will provide results with a lower error. The Cr(III)/Cr(VI) pre-edge peak fit for the untreated sample from Tank T-104 is shown in Figure 5.3. The fit is good, and indicates 15% Cr(VI) in this sample. Fits for the other tanks were similar.

The results from the pre-edge peak fits are summarized in Table 5.1. All the $BiPO_4$ wastes (Tanks B-111, T-104, and T-111) contain both Cr(III) and Cr(VI). The REDOX waste sample from Tank S-104 contains only Cr(VI), an unusual result. Cr(VI) was used in the REDOX process to oxidize other components of the process stream. Because the components were in fact oxidized, it was assumed that some of the chromium was reduced to Cr(III), which is therefore expected to be present (A.L. Boldt, WHC, personal communication). In addition, any nitrite present is expected to reduce Cr(VI) to Cr(III). Nitrite is expected to be found in the tanks because of its addition for corrosion inhibition and because of production from nitrate by radiolysis. Reasons for the absence of Cr(III) in this waste are being investigated. In all cases, no Cr(VI) was found in the treated samples within the

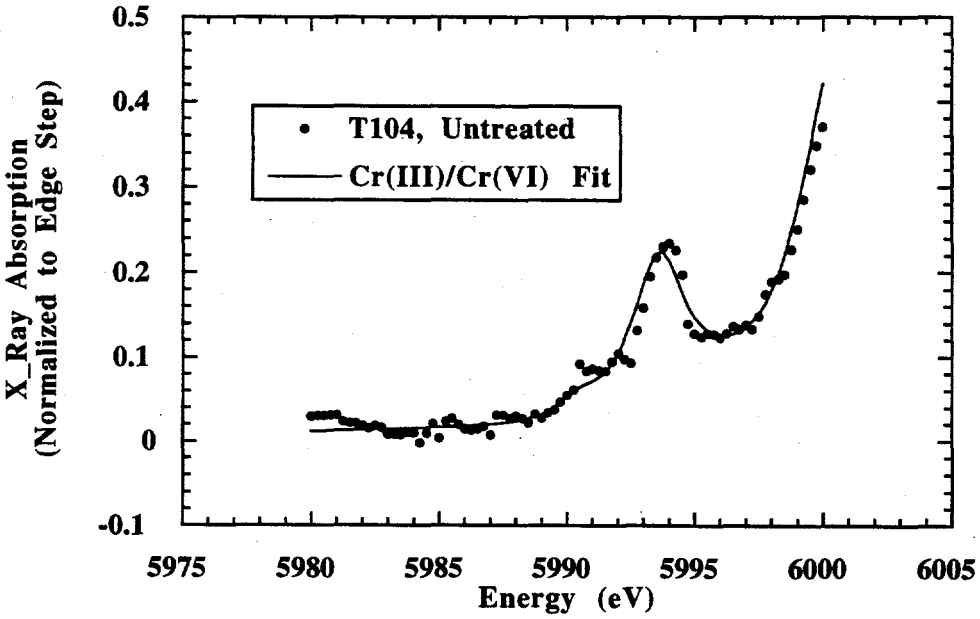

Figure 5.3. The Cr(VI) Pre-edge Peak Fit for the Untreated Sample from Tank T-104. The fit indicates 15% Cr(VI) in this sample. Fits for the other tanks were similar.

Table 5.1. Cr(III) and Cr(VI) Removal by Enhanced Sludge Washing[a] - XANES Results

		Untreated		Treated		% Removal			C(ppm)
Tank	Waste	%Cr(III)	%Cr(VI)	%Cr(III)	%Cr(VI)	Total Cr[b]	Cr(III)	Cr(VI)	Tot Cr
B111	2C, 5-6	70	30	100	0	40	15	100	7000
S104	Redox	0	100	0	0	100	–	100	370
T104	1C	85	15	100	0	25	15	100	4600
T111	2C, 224	75	25	100	0	60	50	100	3200

(a) A wash (0.01M NaOH/0.01M $NaNO_2$), two leaches (3M NaOH) and three washes (same as first wash).
(b) Determined by fusion/ICP. Preliminary data from Sludge Treatment Technology Task.

error. Therefore, all Cr(VI) in these samples is removed by the washing and leaching procedure. Data on total chromium removal from the TWRS Sludge Treatment Technology Task ("Total Cr" column in Table 5.1) were combined with the results of the XANES analysis to determine the amount of Cr(III) removed. Half (50%) of the chromium in T-111 waste was removed by enhanced sludge washing. However, only 15% of the Cr(III) in B-111 and T-104 wastes was removed.

A comparison of the percentage of total chromium removed by the first ("retrieval") wash with the percentage of Cr(VI) determined by XANES suggests that all Cr(VI) is removed by the first wash, leaving the Cr(III) behind (Table 5.2). (All "Actual" values in the table are preliminary results from the TWRS Sludge Treatment Technology Task.

Table 5.2. Removal of Chromium by Enhanced Sludge Washing

	% Removal, 1st Wash		% Cr(VI)	% Removal, Leach[d]		% Removal, Total		Resid. Conc. (ppm)	
Tank	Expected[a]	Actual[b]	Untreated[c]	Expected	Actual	Expected	Actual	Expected	Actual
B111	23	27	30	56	14	79	41	1010	7000
S104	45	90	100	42	6	87	96	4440	370
T104	16	17	15	63	10	79	27	607	4600
T111	11	24	25	67	40	78	64	920	3200

(a) All "Expected" values are based on the following assumptions (consistent with current systems engineering assumptions):
1) The treatment is a 0.1M NaOH wash followed by a 3M NaOH leach.
2) After the wash, Cr is present as $Cr(OH)_3$.
3) There is a 1:1 molar ratio of OH- to Cr in the caustic leach.
4) 75% of the water-insoluble chromium [$Cr(OH)_3$] will leach with caustic.
5) Various other assumptions that may be found in Colton (1995).
(b) All "Actual" values are preliminary results of analysis of solutions and solids following treatment by a wash (0.01M NaOH/0.01M $NaNO_2$), two leaches (3M NaOH) and three washes (same as first wash). Preliminary data from the Sludge Treatment Technology Task.
(c) From XANES analysis.
(d) Includes the three final washes.

Chromium removal was better than expected for the wash step. All "Expected" values in Table 5.2 are estimated values based on the current engineering assumptions for the baseline pretreatment of the tank wastes (Colton 1995), and were produced by the Pretreatment Chemistry Evaluation subtask. The higher-than-anticipated removal suggests that there is more Cr(VI) present in the tank wastes than anticipated.

Comparison of the expected and actual removal of chromium by the leach and final washes indicates much less chromium removal for the $BiPO_4$ wastes (B-111, T-104 and T-111) than expected, which suggests the chromium is present as some species other than $Cr(OH)_3$. Because of the poor removal by the leach step, the overall removal was poor, and for these wastes the residual concentrations of chromium are significant. Analysis of the EXAFS data is in progress to determine the speciation of the Cr(III) that remains behind. Identification of the species may allow a correlation with another component of the sludges that, in turn, permits the effectiveness of the baseline for chromium removal to be predicted for the various wastes. Preliminary results suggest that there are at least two species of chromium left behind in all three $BiPO_4$ wastes. For the B-111 and T-104 samples, it appears that the predominant species is chromium incorporated in a phosphate or aluminate phase, with some chromium in a chromium, iron, or bismuth phase. For T-111 waste, the species are the same, but relative amounts are reversed.

The manganese XAS spectra for the tank samples (B-111, T-104, S-104, and T-111) are being analyzed. The results may provide some insight into the variation in the Cr(III)/Cr(VI) ratio in these samples, as Mn(IV) may be able to oxidize Cr(III) to Cr(VI) in the tank wastes.

5.2 Aluminum, Phosphate, and Sulfate Speciation

Speciation of aluminum is also very important. Enhanced sludge washing tests indicate that, for some wastes, aluminum may be a glass-limiting component. No clear correlation with another component (such as the correlation of phosphorus with calcium) has been deduced, so prediction of aluminum removal is very inaccurate. Tests performed under the Colloidal Studies subtask have demonstrated that $Al(OH)_3$ is easily dissolved by caustic, while boehmite [gamma AlO(OH)], though thermodynamically soluble, is kinetically limited to extremely slow dissolution rates. TEM and XRD analysis of actual sludge samples (Sludge Characterization subtask) has confirmed that $Al(OH)_3$ is removed by enhanced sludge washing, while boehmite is left in the residual solids. Aluminosilicate species are also left behind, but most are amorphous phases and, therefore, could not be identified by TEM or XRD. Identification of these aluminosilicate species will permit correlation with other tank components and aid in predicting the amount of aluminum that will be removed with the baseline processing strategy. Identification of aluminum species in the residual solids is also critical for optimizing the baseline pretreatment process and, if necessary, for modifying the baseline.

Raman spectra of Tank T-104 waste before and after enhanced sludge washing were collected (Figure 5.4) and are being analyzed. These data will be used to help identify aluminum as well as phosphate and sulfate species (including amorphous phases) in the waste. Phosphate and sulfate species also are glass-limiting components for some of these tank wastes (B.M. Rapko, PNL, personal communication).

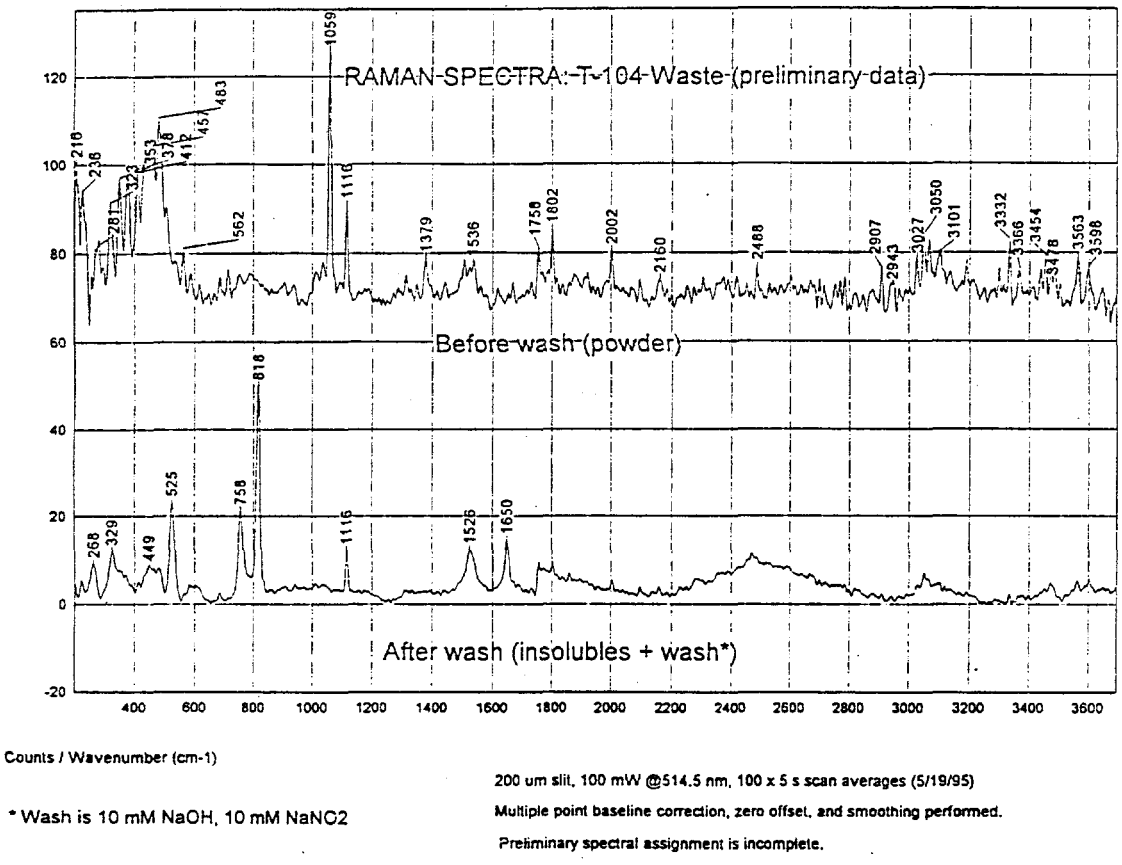

Figure 5.4. Raman Spectra of T-104 Tank Waste Before and After Treatment by Enhanced Sludge Washing. Analysis of the spectra for Al, P and S speciation is in progress.

5.3 Summary

Four waste samples (from Tanks B-111, S-104, T-104 and T-111) were washed and leached to provide samples for speciation studies. Chromium and manganese XAS spectra for eight tank samples (one untreated and one treated sample for each of the tanks listed) were collected at SSRL. Preliminary analysis of the XAS data for chromium indicates that:

for $BiPO_4$ wastes:

- Only Cr(VI) is soluble, and all Cr(VI) is soluble.
- Estimated amounts of soluble chromium, i.e., Cr(VI), are good (even conservative).
- Estimates of amount of insoluble chromium that will leach are too high, possibly due to incorporation of Cr(III) in other "unleachable" phases typical of $BiPO_4$ wastes.

- If removal of chromium to ≤ 5000 ppm chromium in residual solids is necessary, the effectiveness of enhanced sludge washing is marginal, due to poor leaching of Cr(III).

for REDOX wastes:

- All Cr(VI) is soluble.
- More Cr(VI) may be present than estimated.
- If most of the chromium is present as Cr(VI), enhanced sludge washing will remove more chromium than estimated.
- The absence of Cr(III) is unexpected, and may indicate that the core sample tested is not truly representative of REDOX tank wastes.

Raman spectra of T-104 waste were collected before and after treatment. The spectra are being analyzed to determine the feasibility of using Raman spectroscopy for aluminum, phosphate, and sulfate speciation in tank waste solids.

5.4 References

Bajt, S., S. B. Clark, S. R. Sutton, M. L. Rivers, and J. V. Smith. 1993. *Anal. Chem.*, 65:1800.

Bianconi, A. 1988. In *X-Ray Absorption*, eds. D. C. Konigsberger and R. Prins. John Wiley and Sons, New York, pp. 611 - 614, and references therein.

Colton, N. G. 1995. *Sludge Pretreatment Chemistry Evaluation: Enhanced Sludge Washing Separation Factors*. PNL-10512, Pacific Northwest Laboratory, Richland, Washington.

Cotton, F. A., and G. Wilkinson. 1988. *Advanced Inorganic Chemistry*. John Wiley and Sons, New York, pp. 679 ff, and references therein.

Durham, P. J. 1988. In *X-Ray Absorption*, ed. D.C. Konigsberger and R. Prins. John Wiley and Sons, New York, pp. 78 - 81, and references therein.

Sayers, D. E., and B. A. Bunker. 1988. In *X-Ray Absorption*, eds. D.C. Konigsberger and R. Prins. John Wiley and Sons, New York, p. 211.

Waychunas, G. A. 1987. *Am. Mineral.* 72:89.

6.0 Pretreatment Chemistry Evaluation

Penny Colton

Engineering flowsheets that define the interrelationships between pretreatment technologies, in terms of operations, material and energy flows, and equipment, are evaluated in systems engineering studies to provide information for design and planning purposes, e.g., process capacity requirements, final waste stream compositions and volumes, and tank storage requirements. For these evaluations, tank waste inventory data and knowledge of the chemical and physical characteristics of tank wastes are needed. While efforts within the TWRS Sludge Treatment Technology Development and Tank Waste Treatment Science tasks are focused on providing experimental data for engineering evaluations, the technical database in terms of process feed compositions is far from complete. In the absence of data, engineering studies frequently must rely on estimated waste inventories and on assumptions about the chemical and physical behavior of waste components to define feed compositions.

One of the objectives of the Pretreatment Chemistry Evaluation subtask is to gather, evaluate, and integrate data on tank wastes that are relevant to refining these estimated inventories and assumed "dissolution factors," i.e., wash and leach factors for partitioning waste components between liquid and solid phases. Efforts this quarter have focused on using experimental data to evaluate selected dissolution factors for the total SST waste inventory and on outlining an approach for extracting tank-specific partitioning factors for all SST wastes from limited experimental data. The following sections summarize the results to date from these efforts.

6.1 Aluminum, Chromium, and Phosphate Dissolution Factors - SST Waste Inventory

Currently, the feed to the TWRS Process Flowsheet (Orme 1994) represents a homogeneous mixture of both single- and double-shell tank wastes. Together, the combined inventory data and the dissolution factors represent a composition that minimizes the volume of HLW produced. As a result, this feed stream is often referred to as an "idealized blend." Because the feed to pretreatment drives process capacity and HLW volumes, accurate inventory and dissolution factors are needed. Work performed under this subtask in FY 1994 included an evaluation of some of the sludge wash factors that are assumed for the overall SST inventory, specifically, wash factors for elements that would be found primarily in sludges, e.g., bismuth, iron, etc. Salt cake data from Schulz (1980) were not included in the review at that time, and, as a result, wash factors for elements such as aluminum, chromium, and phosphorus that are found in salt cake- as well as sludge-type wastes were not revised.

During this quarter, a preliminary review of data was conducted for salt cake wastes from two major evaporator campaigns. The results from this review and the results from recent sludge washing and leaching experiments (summarized in Table 6.1) for aluminum, chromium, and phosphate were used to project SST wash and leach factors for these three waste constituents. The results from this evaluation are summarized in Table 6.2.

Aluminum. The currently assumed inventory for aluminum in SSTs is 2940 MT: 25% "soluble," i.e., aluminum that would be removed with an inhibited water wash; and 75% "insoluble," i.e., aluminum that would remain after an inhibited water wash. The projected masses for the various waste groupings account for 108% of the assumed aluminum inventory; however, no data were available for two salt

Table 6.1. Summary of Enhanced Sludge Washing Results

		Aluminum				Chromium				Phosphate			
		% SST Al Inv	MT removed/ MT starting	% removed (tank)	% removed (SST Al Inv)	% SST Cr Inv	MT removed/ MT starting	% removed (tank)	% removed (SST Cr Inv)	% SST PO4 Inv	MT removed/ MT starting	% removed (tank)	% removed (SST PO4 Inv)
BIPO4													
1C (PNL)	T-104	1.06	19.3/31.2	62	0.66	0.66	0.475/1.76	27	0.18	3.0	78.1/142	55	1.7
1C (LANL)	T-104	1.06	19.7/31.2	63	0.67	0.66	0.880/1.76	50	0.33	3.0	139/142	98	2.9
1C/RCW	U-110	6.1	141/178	79	4.8	0.15	.194-.306/.413	47-74	0.093	0.93	~43.9/43.9	100	0.93
	T-107	0.54	12.4/15.9	78	0.42	0.130	0.213/0.349	61	0.079	2.0	92.5/93.4	99	2.0
1C/TBP	BX-107	0.76	15.2/22.4	68	0.52	0.56	0.438/1.51	29	0.16	2.3	102/110	93	2.2
2C/5-6	B-110	0.051	<0.8/1.5	<53	0.027	0.46	0.781/1.22	64	0.29	1.4	63.4/65.4	97	1.3
	B-111	0.051	0.03/1.5	2	0.00102	0.48	0.512/1.28	40	0.19	1.1	46.3/50.9	91	0.98
2C/224	T-111	0.036	0.139/1.07	13	0.0047	1.4	2.35/3.73	63	0.88	0.66	22.5/31.3	72	0.48
224	B-201	0.0219	.116-.264/.643	18-41	0.0058	0.17	.213-.288/.443	48-65	0.091	0.051	.389-.940/2.41	16-39	0.014
TBP													
TBP(f)/1C	C-109	1.17	27.8/34.3	81	0.95	0.026	.052-.058/.069	75-84	0.021	1.2	24.6/58.6	42	0.52
	C-112	0.36	9.09/10.7	85	0.31	0.070	0.133/0.188	88	0.050	1.1	43.7/52.0	84	0.92
REDOX													
REDOX-RCW	S-104	6.7	74.5/196	38	2.5	2.7	6.92/7.13	97	2.6	0.0102	<DL/0.481		<DL
PUREX													
AR Sludge	C-103	0.155	2.18/4.55	48	0.074	0.072	0.021/0.194	11	0.0078	0.083	2.59/3.93	66	0.055
Totals		17.6		58	10.2	6.8		68	4.6	14		86	12
		Based on 2940 MT Al for SST wastes				Based on 268 MT Cr for SST wastes				Based on 4730 MT PO4 for SST wastes			

NOTE: The % removed figures (Total SST Inventory) reflect sludge samples only. Part of the inventories for Al, Cr, and PO4 may be distributed throughout salt cake wastes which comprise 65% of the total SST waste inventory.

Table 6.2. Projected Aluminum, Chromium, and Phosphate Distribution and Dissolution Factors for SST Waste Inventory.

		Aluminum					Chromium					Phosphate				
		Wash MT	Leach MT	Insoluble MT	Total MT	% Al SST Inv	Wash MT	Leach MT	Insoluble MT	Total MT	% Cr SST Inv	Wash MT	Leach MT	Insoluble MT	Total MT	% PO4 SST Inv
BiPO4	1C	2.33	142	88.5	233	7.92	2.10	4.47	6.57	13.1	4.90	276	763	22	1061	22.4
	2C	0.153	0.038	9.35	9.54	0.324	1.18	3.84	2.82	7.84	2.92	171	171	22	364	7.7
	224	0.0917	2.66	6.42	9.17	0.312	1.01	2.60	2.72	6.33	2.36	2.40	7.21	24.7	34.4	0.7
	EB/1C	16.8	3.06	1.95	21.8	0.740	0.0462	0.0859	0.132	0.264	0.099	2102	--	--	2102	44.4
		19.3	148	106.2	273	9.30	4.34	11.0	12.2	27.6	10.3	2553	942	68.2	3559	**75.3**
TBP	TBP	0.011	8.977	2.1	11.1	0.377	0.0971	0.383	0.0913	0.571	0.213	115	311	317	743	15.7
	TFeCN	0.899	20.1	4.7	25.7	0.874	0.298	0.161	0.030	0.489	0.182	80.5	6.9	51.4	139	2.9
	PFeCN															
	BYits															
		0.910	29.1	6.8	36.8	1.25	0.395	0.544	0.121	1.06	0.396	195	318	368	882	18.6
REDOX	R-RCW (boil)	46.8	398.0	726	1171	39.8	19.2	22.2	1.25	42.6	15.9	0.259	--	2.61	3	0.061
	R-RCW	44.2	816.8	243	1104	37.5	18.1	20.9	1.21	40.2	15.0	0.244	--	2.46	3	0.057
	(R)/EB	265	2.37	3.86	271	9.22	72.7	--	--	72.7	27.1	256	--	--	256	5.41
	EB/(R)															
	EB/RCW															
		356	1217	967	2550	**86.6**	110	43	2.5	156	**58.0**	257	--	5.08	262	5.53
PUREX	CC/AR	7.52	4.41	4.78	16.7	0.568	0.297	0.111	3.30	3.71	1.38	36.6	--	1.93	38.5	0.814
	AR/PCW	0.0200	19.2	20.7	39.9	1.36	0.0112	0.112	1.00	1.12	0.418	2.41	6.96	4.8	14.2	0.300
	PCW/ZrCW	2.0	47.5	49.6	99.1	3.37	0.1470	0.257	3.27	3.68	1.37	0.93	19.5	10.5	30.9	0.654
	DSSF	160	–	17.8	178	6.04	0.492	1.31	14.6	16.4	6.11	64.5	--	1.32	65.8	1.39
		169	71	92.8	333	11.34	0.947	1.79	22.2	24.9	9.29	104.4		18.6	149.4	3.16
Totals (MT)		545	1465	1177	3195		116	56.4	37.0	209		3109	1258	460	4849	
% SST Inv		18.5	49.8	40.0		108	43.2	21.0	13.8		78.0	65.7	26.6	9.7		103
		Based on 2940 Al for SST wastes					Based on 268 MT Cr for SST Wastes					Based on 4730 MT PO4 for SST wastes				

cake waste types that also could contain aluminum. The aluminum in these additional waste types might increase the percentage of wash-soluble aluminum to reflect the assumed wash factor of 25%. Note that the bulk of the aluminum appears to be in wastes that originated from the REDOX process and evaporator campaigns. Aluminum nitrate was used as a salting agent in REDOX campaigns. The 50% total aluminum estimated to be removed with leaching translates to removing ~56% to 60% of the aluminum that remained after the wash. The aluminum behavior of S-104 waste was extrapolated to account for all REDOX (boiling) wastes. The low aluminum removal in S-104 may be due to slower leaching rates or solubility constraints for boehmite, which appears to be the predominant form of aluminum in that tank.

Chromium. The currently assumed inventory for chromium in SSTs is 269 MT: 55% "soluble" and 45% "insoluble." The projected masses for the various waste groupings account for only 79% of the assumed chromium inventory; however, no data were available for two salt cake waste types that most likely contain chromium. Again, note that the bulk of the chromium is expected to be in REDOX-type wastes. Chromium was added as an oxidizing agent in higher concentrations in the REDOX process than in other processes.

Phosphate. The currently assumed inventory for phosphate in SSTs is 4730 MT: 61% "soluble" and 39% "insoluble." The projected masses for the various waste groupings account for 103% of the assumed phosphate inventory. While no data were available for two salt cake waste types, these waste types would not be expected to contain significant concentrations of phosphate. Not surprisingly, the bulk of the phosphate is expected to be in wastes that originated from the bismuth phosphate process. The projected wash factor agrees with the currently assumed wash factor. The 27% total phosphate removed in the leach translates to 76% of the water-insoluble phosphate being removed. Assuming the phosphate in the residual solids is tied to calcium, the SST calcium inventory would be approximately 370 MT, close to three times higher than the inventory currently assumed.

6.2 An Approach for Defining Tank-specific Dissolution Factors

While the idealized blend can be used to estimate the volume of HLW that will be produced, tank-specific data are required in order to more realistically evaluate the effect of pretreatment processes on this volume. Estimated inventories exist for all SST wastes. These inventories are derived from the Tank Layer Model (TLM) and defined waste streams that were developed by Los Alamos National Laboratory (LANL) using process and tank fill history records. In addition to these estimated inventories, wash and leach data will be available for 25 SST sludge-type wastes; characterization data will be available for approximately 32 wastes; and salt cake data (Schulz 1980) will be reviewed for an additional 7 wastes by the end of FY 1995.

The challenge is to reconcile this information in order to establish sound inventories and dissolution factors because results from systems engineering evaluations will be only as good as the input to the evaluation. One approach that is being examined by this subtask is to assign dissolution factors to each of the defined wastes streams, and then use the TLM to weight the contributions of these factors to a specified tank waste inventory. The relationships among individual SST wastes and various waste groups, process streams, and chemical processing campaigns were established to see how available information for a limited number of tank wastes might translate into dissolution information for defined waste streams. These relationships are pictured in Figure 6.1. The following points are noted to help interpret this figure:

- Waste-type groups originated from the Sort on Radioactive Waste Type (SORWT) model (Hill et al. 1995).

- The LANL-defined waste streams represent, for the most part, the various process streams. These defined waste streams were used in conjunction with the TLM to estimate tank-specific inventories.

- The process, waste stream, and waste grouping boxes are intended to be proportional to the volume of solids that correspond to these boxes.

- The shading under the Tanks column represents a degree of data available and may be interpreted as follows

  Dark: experimental wash/leach data available

  Light: characterization data available with mass balance $\geq 90\%$

  Double-lined clear: salt cake work by Schulz (1980) or, for sludge wastes, characterization data available with mass balance $< 90\%$.

  The shading for the groups, waste streams, and processes is intended to represent the degree of information that is available for generating dissolution factors and is related to the shading for the specific tank wastes in each of these categories.

6.3 References

Hill, J. G., G. S. Anderson, and B. C. Simpson. 1995. *The Sort on Radioactive Waste Type Model: A Method to Sort Single-Shell Tanks Into Characteristic Groups*. PNL-9814, Rev. 2, Pacific Northwest Laboratory, Richland, Washington.

Orme, R. M. 1994. *TWRS Process Flowsheet.* WHC-SD-WM-TI-613, Westinghouse Hanford Company, Richland, Washington.

Schulz, W. W. 1980. *Removal of Radionuclides from Hanford Defense Waste Solutions.* RHO-SA-51, Rockwell Hanford Operations, Richland, Washington.

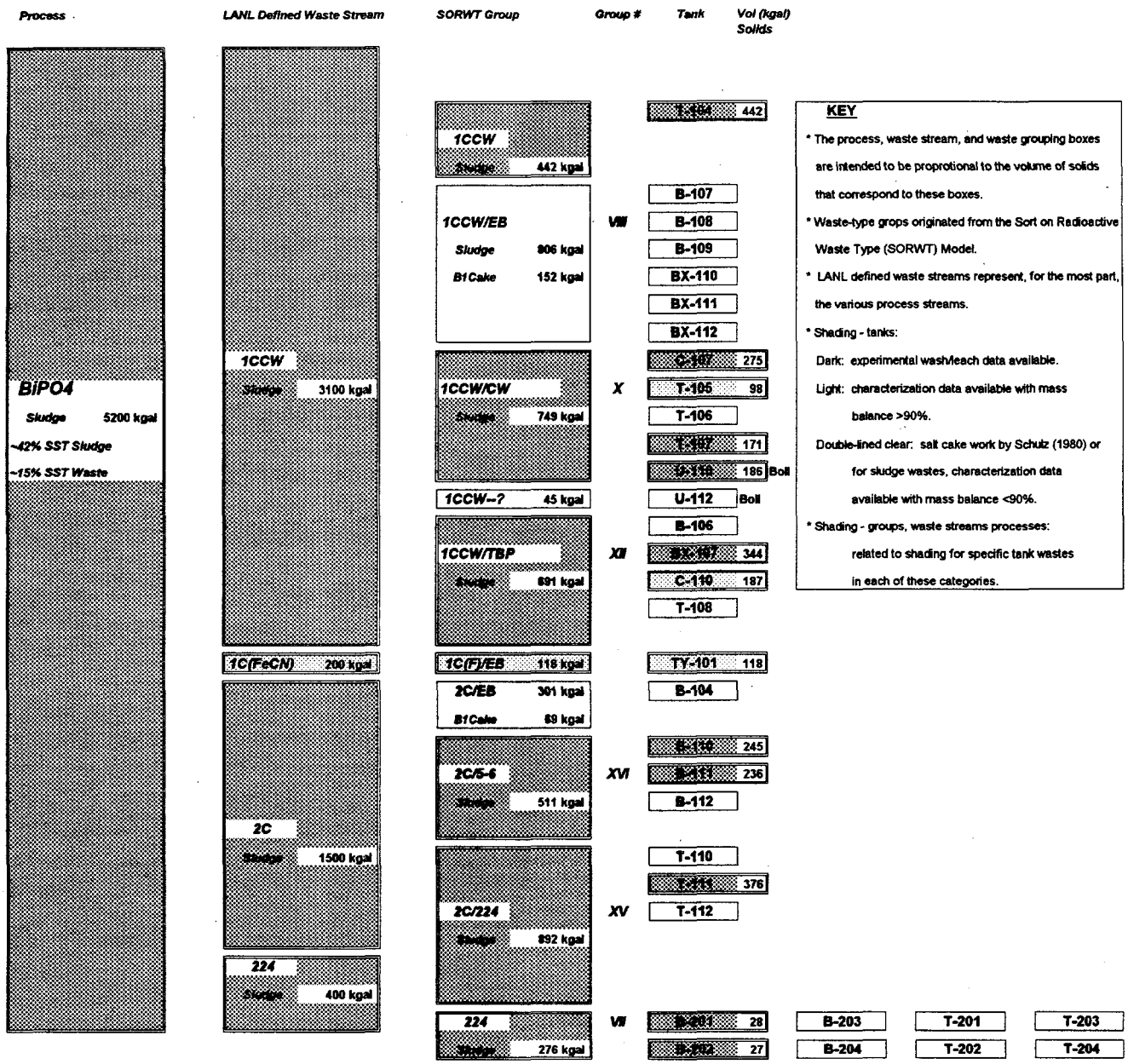

Figure 6.1. Pictorial Summary That Depicts the Relationships Among Chemical Processes/Campaigns, Defined Process Streams, SORWT Groups, and Single-Shell Tank Wastes.

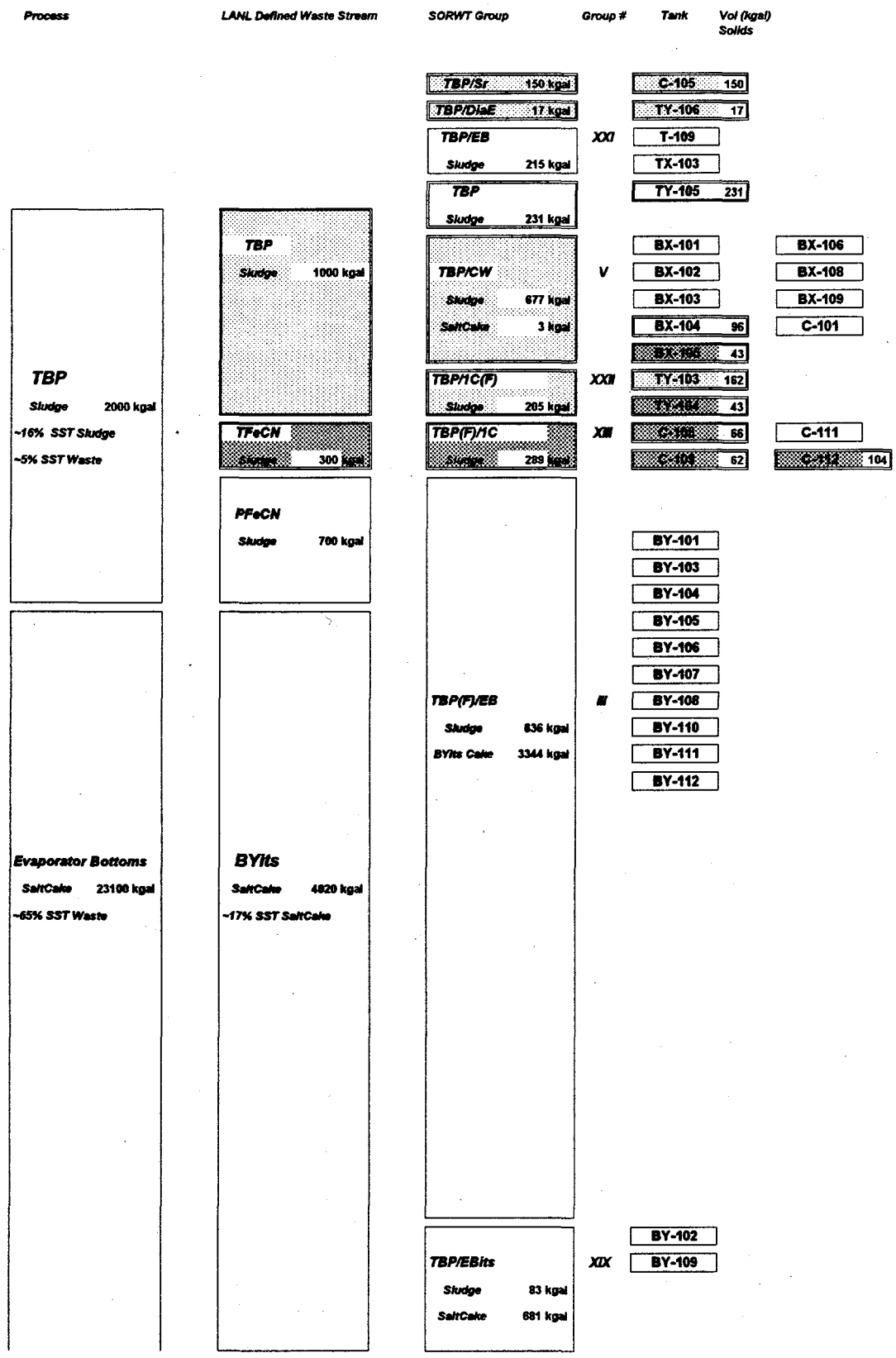
Process
LANL Defined Waste Stream
SORWT Group
Group #
Tank
Vol (kgal) Solids
TBP
Sludge 2000 kgal
~16% SST Sludge
~5% SST Waste
Evaporator Bottoms
SaltCake 23100 kgal
~65% SST Waste
TBP
Sludge 1000 kgal
TFeCN
Sludge 300 kgal
PFeCN
Sludge 700 kgal
BYIts
SaltCake 4820 kgal
~17% SST SaltCake
TBP/Sr 150 kgal
C-105 150
TBP/DiaE 17 kgal
TY-106 17
TBP/EB
Sludge 215 kgal
XXI
T-109
TX-103
TBP
Sludge 231 kgal
TY-105 231
TBP/CW
Sludge 677 kgal
SaltCake 3 kgal
V
BX-101
BX-102
BX-103
BX-104 96
BX-105 43
BX-106
BX-108
BX-109
C-101
TBP/1C(F)
Sludge 205 kgal
XXII
TY-103 162
TY-104 43
TBP(F)/1C
Sludge 289 kgal
XIII
C-106 66
C-104 62
C-111
C-112 104
TBP(F)/EB
Sludge 836 kgal
BYIts Cake 3344 kgal
III
BY-101
BY-103
BY-104
BY-105
BY-106
BY-107
BY-108
BY-110
BY-111
BY-112
TBP/EBits
Sludge 83 kgal
SaltCake 681 kgal
XIX
BY-102
BY-109

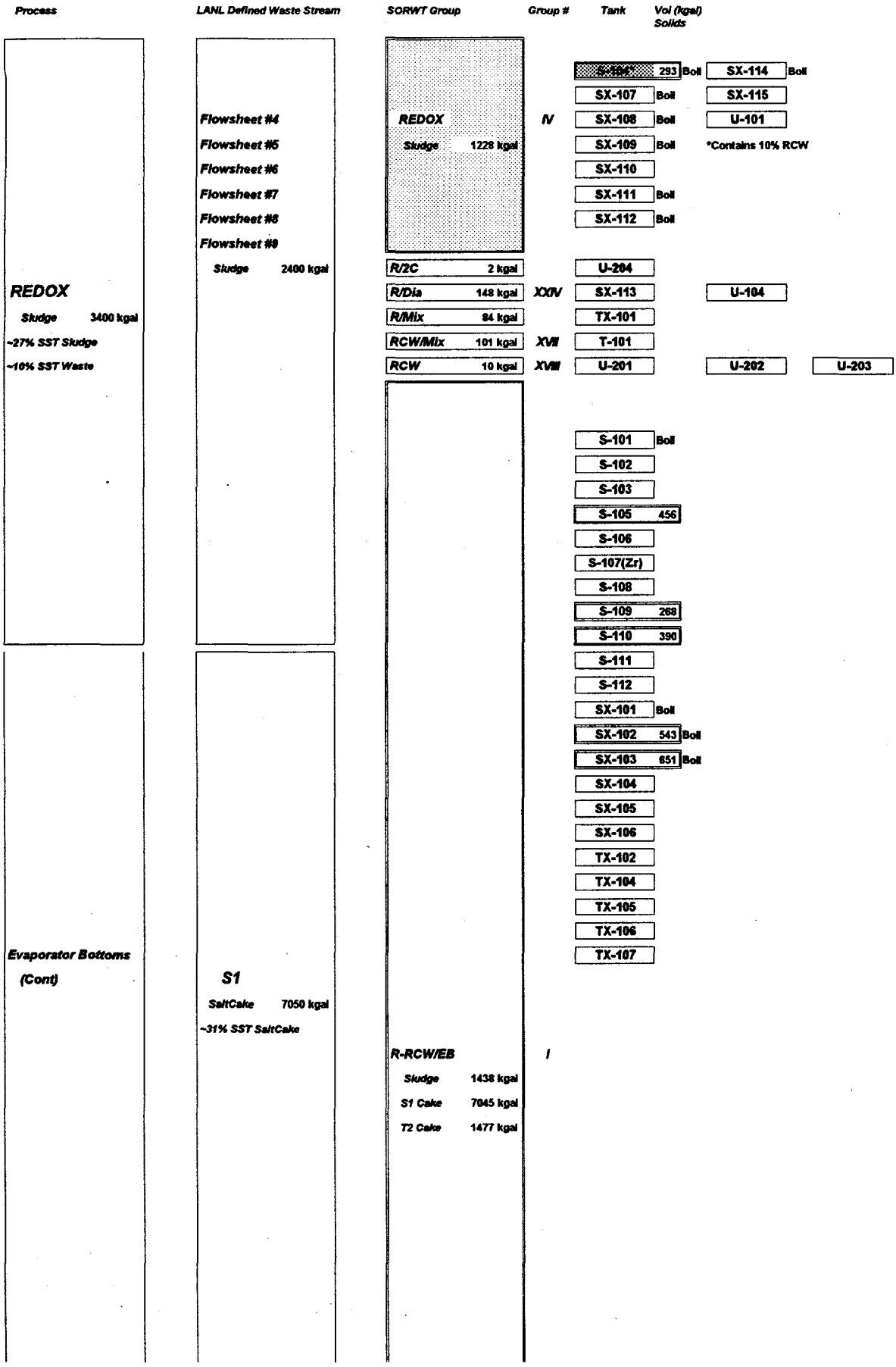
Process
LANL Defined Waste Stream
SORWT Group
Group #
Tank
Vol (kgal) Solids
REDOX
Sludge 3400 kgal
~27% SST Sludge
~10% SST Waste
Flowsheet #4
Flowsheet #5
Flowsheet #6
Flowsheet #7
Flowsheet #8
Flowsheet #9
Sludge 2400 kgal
REDOX
Sludge 1228 kgal
IV
S-104* 293 Boil
SX-107 Boil
SX-108 Boil
SX-109 Boil
SX-110
SX-111 Boil
SX-112 Boil
SX-114 Boil
SX-115
U-101
*Contains 10% RCW
R/2C 2 kgal
R/Dia 148 kgal
R/Mix 84 kgal
RCW/Mix 101 kgal
RCW 10 kgal
XXIV
XVII
XVIII
U-204
SX-113
TX-101
T-101
U-201
U-104
U-202
U-203
S-101 Boil
S-102
S-103
S-105 456
S-106
S-107(Zr)
S-108
S-109 268
S-110 390
S-111
S-112
SX-101 Boil
SX-102 543 Boil
SX-103 651 Boil
SX-104
SX-105
SX-106
TX-102
TX-104
TX-105
TX-106
TX-107
Evaporator Bottoms
(Cont)
S1
SaltCake 7050 kgal
~31% SST SaltCake
R-RCW/EB
Sludge 1438 kgal
S1 Cake 7045 kgal
T2 Cake 1477 kgal
I

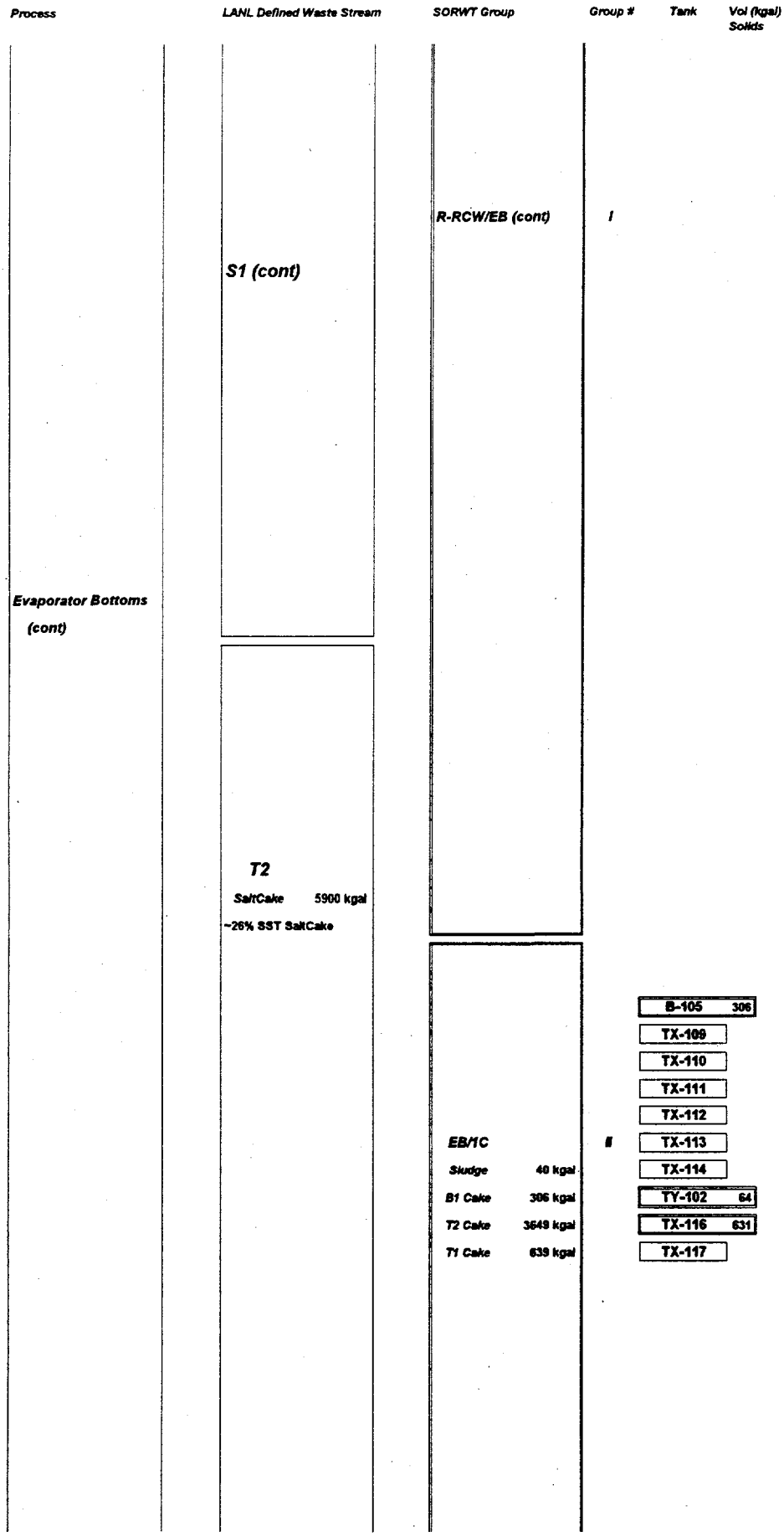
Process
LANL Defined Waste Stream
SORWT Group
Group #
Tank
Vol (kgal)
Solids
S1 (cont)
R-RCW/EB (cont)
I
Evaporator Bottoms
(cont)
T2
SaltCake 5900 kgal
~26% SST SaltCake
EB/1C
II
Sludge 40 kgal
B1 Cake 306 kgal
T2 Cake 3649 kgal
T1 Cake 639 kgal
B-105 306
TX-109
TX-110
TX-111
TX-112
TX-113
TX-114
TY-102 64
TX-116 631
TX-117

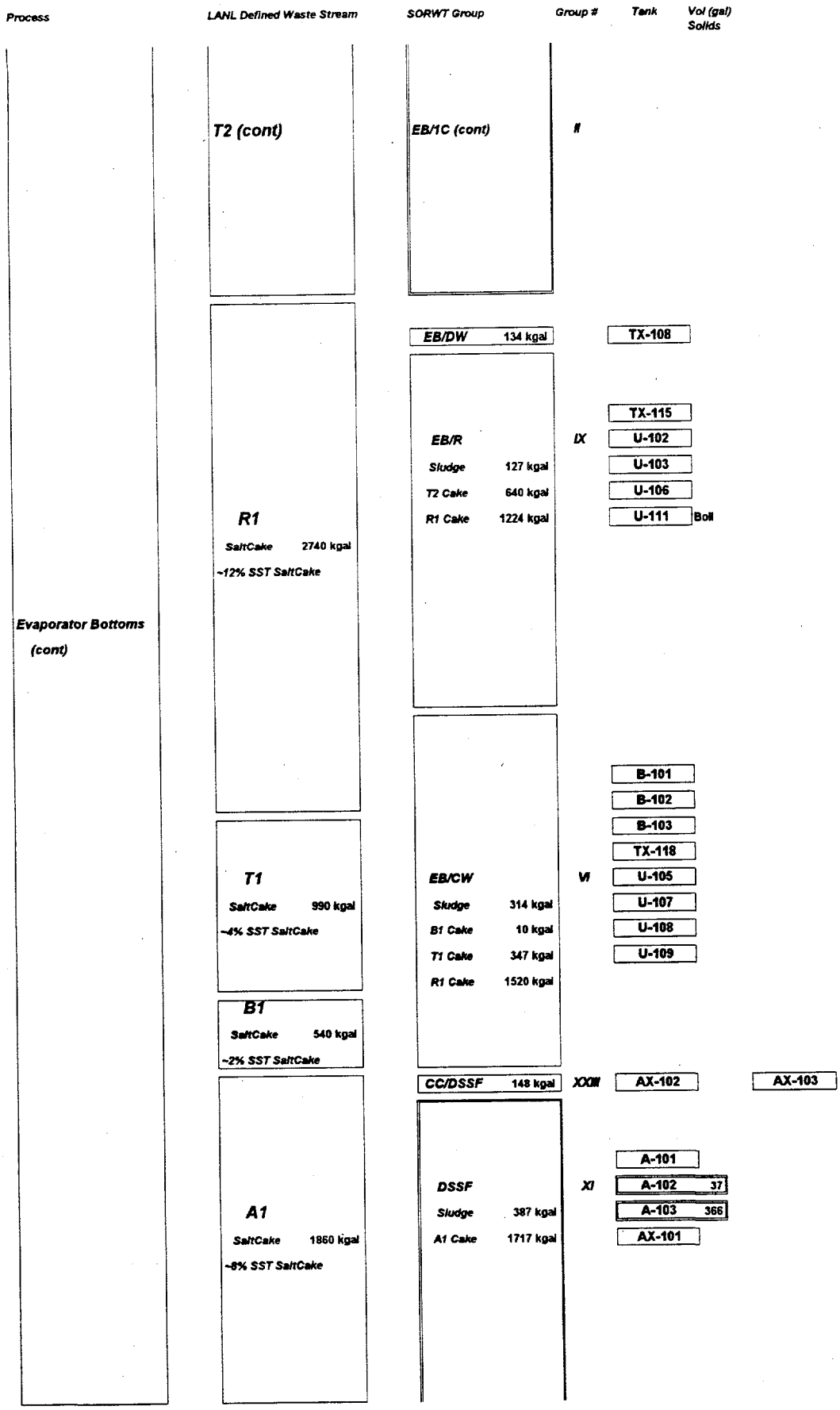
Process
LANL Defined Waste Stream
SORWT Group
Group #
Tank
Vol (gal) Solids
Evaporator Bottoms (cont)
T2 (cont)
EB/1C (cont)
II
EB/DW 134 kgal
TX-108
R1
SaltCake 2740 kgal
~12% SST SaltCake
EB/R
Sludge 127 kgal
T2 Cake 640 kgal
R1 Cake 1224 kgal
IX
TX-115
U-102
U-103
U-106
U-111
Boil
T1
SaltCake 990 kgal
~4% SST SaltCake
EB/CW
Sludge 314 kgal
B1 Cake 10 kgal
T1 Cake 347 kgal
R1 Cake 1520 kgal
VI
B-101
B-102
B-103
TX-118
U-105
U-107
U-108
U-109
B1
SaltCake 540 kgal
~2% SST SaltCake
CC/DSSF 148 kgal
XXII
AX-102
AX-103
A1
SaltCake 1860 kgal
~8% SST SaltCake
DSSF
Sludge 387 kgal
A1 Cake 1717 kgal
XI
A-101
A-102 37
A-103 366
AX-101

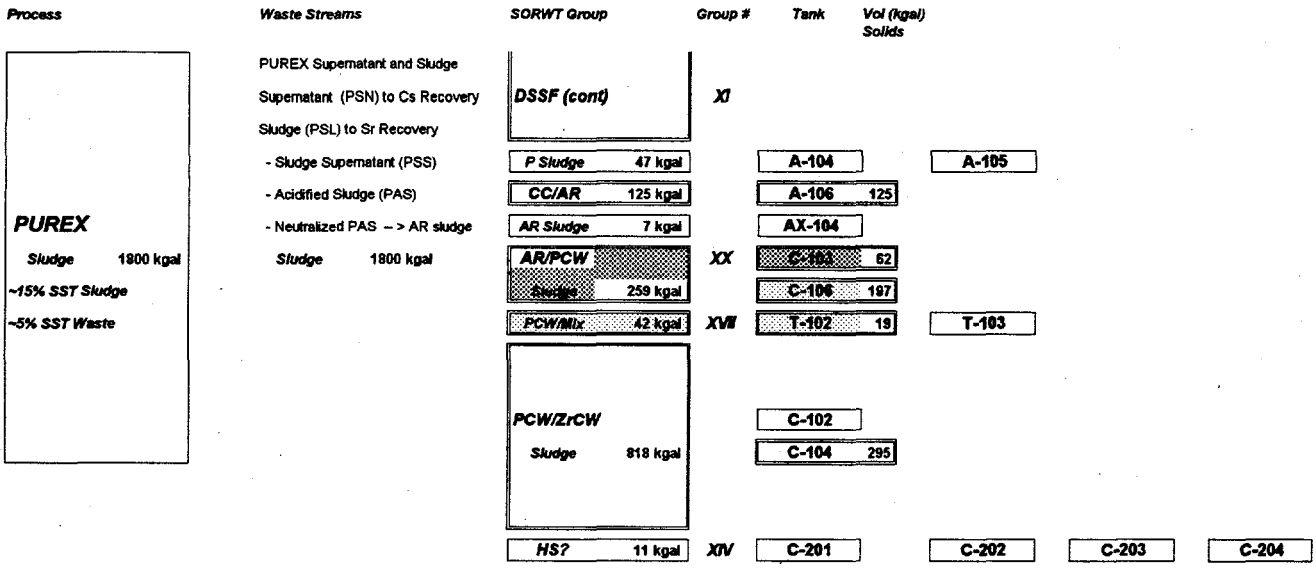
Process
Waste Streams
SORWT Group
Group #
Tank
Vol (kgal)
Solids
PUREX
Sludge 1800 kgal
~15% SST Sludge
~5% SST Waste
PUREX Supernatant and Sludge
Supernatant (PSN) to Cs Recovery
Sludge (PSL) to Sr Recovery
- Sludge Supernatant (PSS)
- Acidified Sludge (PAS)
- Neutralized PAS -- > AR sludge
Sludge 1800 kgal
DSSF (cont)
XI
P Sludge 47 kgal
A-104
A-105
CC/AR 125 kgal
A-106 125
AR Sludge 7 kgal
AX-104
AR/PCW
Sludge 259 kgal
XX
C-106 62
C-106 197
PCW/Mix 42 kgal
XVII
T-102 19
T-103
PCW/ZrCW
Sludge 818 kgal
C-102
C-104 295
HS? 11 kgal
XIV
C-201
C-202
C-203
C-204

7.0 Colloidal Studies for Solid-Liquid Separation

Bruce C. Bunker, Gordon L. Graff, Jon R. Phillips, Yong Wang, Lin Song, X. Shari Li, Peter A. Smith, Paul J. Bruinsma, David R. Rector, Joel M. Tingey, and Charles R. Hymas

The objective of the Colloidal Studies subtask is to understand and model the behavior of the insoluble colloidal particles that comprise tank sludge and determine how colloidal interactions impact major steps in tank waste processing. Experimental and theoretical studies have been performed to examine colloidal agglomeration behavior and the impact this behavior has on properties such as slurry viscosity, sedimentation rates, sediment densities, and ease of filtration.

During the first two quarters of FY 1995, the emphasis of the work was on understanding the colloidal behavior of single component systems such as gibbsite [$Al(OH)_3$], boehmite (AlOOH), and iron hydroxide [$Fe(OH)_3$]. Work performed this quarter includes studies of multicomponent systems; studies of how processing conditions, such as temperature and agitation, influence behavior; and studies of reactions between different sludge components. Work has also commenced to correlate the results obtained on the simple suspensions with results obtained on real tank sludge. For the final quarter, we anticipate that much of the work will involve colloidal studies on actual tank sludges and use equipment and facilities that are being consolidated into a new Hot Colloids Laboratory.

The information presented in the following sections will 1) describe activities performed to study reactions leading to the formation of aluminosilicates in tank waste; 2) describe progress that has been made to understand and model the general behavior of sludge suspensions based on agglomerate structures and how agglomerates are modified by processing conditions, such as heating and agitation; 3) describe experimental results obtained on various mixtures of colloidal particles; and 4) explain results reported to date on the behavior of actual sludge samples.

7.1 Formation of Aluminosilicates

Consolidation of colloidal particles to form cements represents one extreme class of behavior that can occur in slurries such as tank sludge. Experiments performed on multicomponent simulants show that recipes containing colloidal silica as a starting material sometimes form hard, cement-like materials. Beyond the concern that a certain fraction of cementous material might be present in tanks, the possibility exists that cement could be formed during retrieval, pretreatment, or feed concentration steps (in evaporators, etc.) with dire consequences. Conversely, deliberate conversion of specified waste streams into cement or grout as an immobilization strategy requires a knowledge of similar reactions.

Reactions involving silica are of interest not only in terms of cement formation but in terms of formation of insoluble phases that might impact pretreatment. Of particular concern is the formation of aluminosilicate phases that can be highly resistant to dissolution during washing and leaching. Such aluminosilicates would be retained even after pretreatment and potentially impact the volume of HLW glass.

The goals of the work described below are 1) to identify which aluminosilicate phases form as a function of solution compositions that might be encountered in waste processing; 2) to compare predictions of aluminosilicate formation with phase distributions seen in actual sludges via techniques such as transmission electron microscopy (TEM); 3) to develop models for aluminum removal from tank sludges based on the solubility and dissolution kinetics of aluminosilicates; and 4) to identify conditions that could lead to cement formation during retrieval, pretreatment, and remediation of tank wastes. The general approach is to prepare basic solutions containing various concentrations of sodium, aluminum, and silicon (as soluble species or colloids) and to use x-ray, solid-state nuclear magnetic resonance (NMR), and Raman techniques to characterize any solid materials that form. This quarter, the first series of solutions, prepared using boehmite and colloidal silica as the aluminum and silicon sources, have been characterized using x-ray and solid-state NMR analyses.

Solutions containing sodium, aluminum, and silicon can react to form a wide range of aluminosilicate phases. For example, the diagram in Figure 7.1 shows the phases produced via hydrothermal synthesis at 250°C for mixtures of NaOH, SiO_2, and AlOOH. The diagram shows that a number of structures including clays, zeolites, and feldspars can be produced by varying the ratios of Na:Al:Si. While such diagrams indicate the range of materials that can form, mere knowledge of the Na:Si:Al ratios in a given sludge composition is insufficient to predict the phases that might be present in tanks. Phase formation also depends on factors such as pH, solution concentrations, temperature, and the presence of competing reactions. High pH conditions tend to produce zeolites such as cancrinite, while

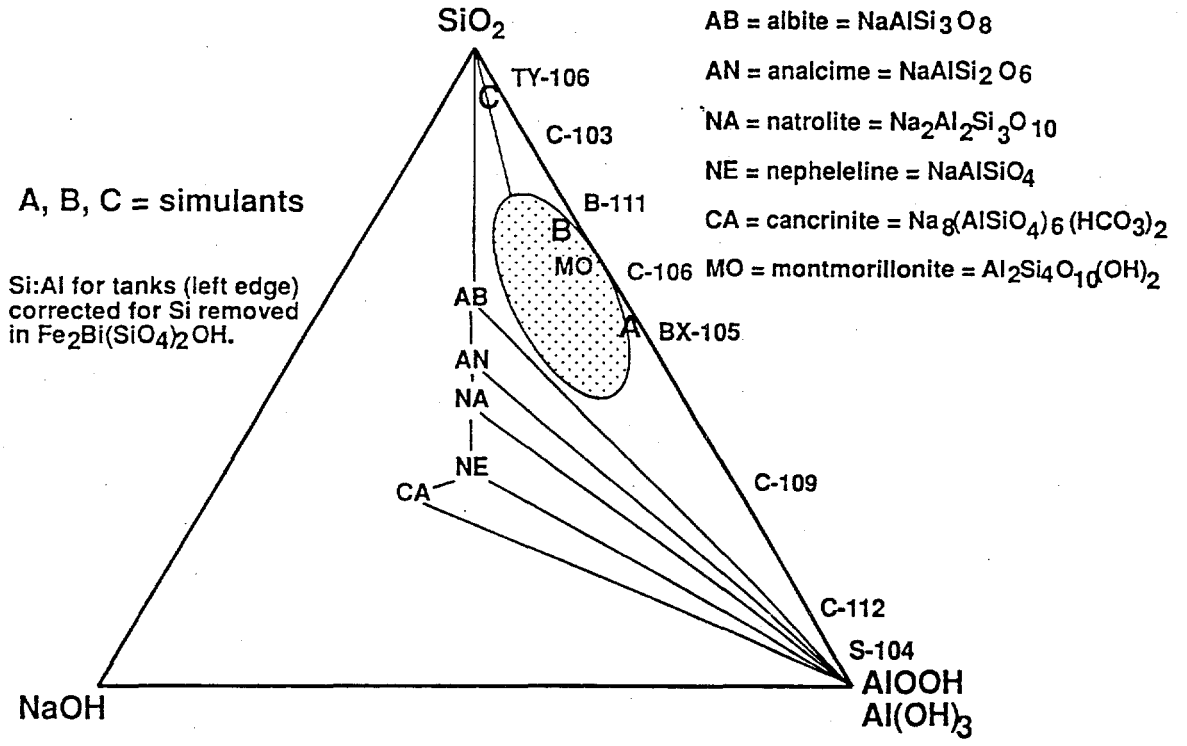

Figure 7.1. Phase Diagram for Aluminosilicates in Water. Many different aluminosilicate phases can potentially form in tanks vs. composition, pH, temperature, and time. Each phase has different solubility, stability characteristics.

lower pH solutions tend to form clays such as montmorillonite. Formation of some phases is kinetically limited. Aluminosilicate phases observed in hot solutions can take years to form in cold solutions. As will be shown below, high concentrations tend to lead to formation of amorphous gels and cements, while lower concentrations favor crystalline materials. Results from TEM analyses described in Section 4.0, Sludge Characterization Studies, indicate that soluble silica in some wastes reacts preferentially with iron and bismuth to form $Fe_2Bi(SiO_4)_2OH$ rather than aluminosilicates. "Free" silicon that is available for aluminosilicate formation represents the silicon not tied up in this phase. Si:Al ratios for known tank compositions corrected for removal of silicon by the bismuth iron silicate phase are indicated in Figure 7.1. Based on Si:Al ratio, the diagram suggests that a wide range of aluminosilicate phases might be possible over the range of tank compositions found at Hanford, with different mixes of phases being present in different tanks.

In terms of pretreatment, knowing the structure and composition of aluminosilicates is important for predicting the solubility and dissolution kinetics of aluminum leaching from sludge. For example, dissolution rate data for aluminosilicate phases extrapolated to tank processing conditions (Figure 7.2) indicate that initial aluminum leaching kinetics (in undersaturated solutions) can vary by up to seven orders of magnitude, depending on what phase is present. The removal of aluminum-containing phases was monitored via solution analyses and TEM to relate the relative dissolution rates to practical sludge washing and leaching experience. Gibbsite, with a dissolution rate near 10^{-7} mole/cm^2-sec, is completely dissolved in standard washing and leaching procedures, while boehmite, which dissolves

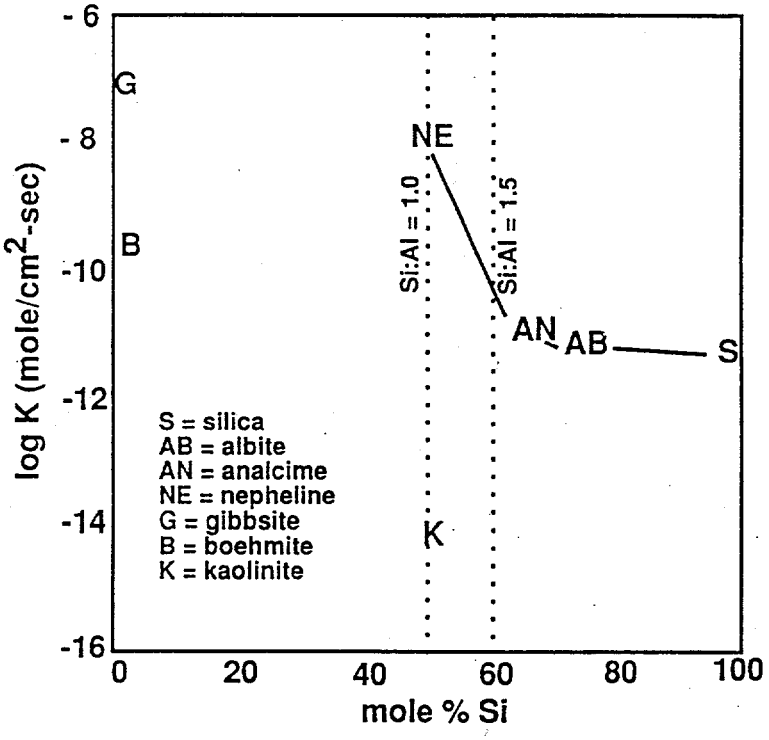

Figure 7.2. Range of Dissolution Rates for Aluminosilicates in Hot, Basic Solutions (100°C, pH 14). Composition range detected via NMR for zeolitic precipitates could result in a 1000-fold span of Al leach rates.

over 100 times slower, is largely retained in sludge using standard treatments. Indications are that nepheline, a zeolite with Si:Al = 1, could also be dissolved via standard washing and leaching, while analcime (Si:Al = 2) and albite (Si:Al = 3) would be largely untouched.

Several techniques are required to determine the structure and composition of aluminosilicates. If tank conditions lead to the formation of crystalline aluminosilicates and if the crystallites are relatively large, x-ray crystallography can sometimes provide sufficient identification of a given aluminosilicate phase. However, TEM analyses show that tank conditions can lead to the formation of amorphous or poorly crystalline aluminosilicates. In addition, many aluminosilicate phases (particularly zeolites and clays) can exhibit a wide range of compositions via substitution of aluminum for silicon in the structure. X-ray analysis is not sensitive to such substitutions. For this reason, solid-state NMR and Raman analyses are being investigated.

Solid-state NMR spectra are capable of providing quantitative information concerning local coordination geometries around both silicon and aluminum sites in aluminosilicates. ^{27}Al NMR spectra reveal whether aluminum is coordinated to 6 oxygens [Al(6) as in gibbsite, boehmite, and the octahedral sheets in clays] or in tetrahedral sites coordinated by 4 oxygens [Al(4) as in zeolites, feldspars, and the tetrahedral sheets in clays]. Octahedral Al(6) sites exhibit a chemical shift in NMR spectra near 0 ppm, while tetrahedral Al(4) sites appear in NMR spectra near 60 ppm. In all aluminosilicates, silicon is tetrahedrally coordinated by four oxygens. ^{29}Si NMR spectra reveal what species are bonded to these four oxygens. In zeolitic networks, where all oxygens bridge between two network formers such as silicon or aluminum, the spectra reveal how many of the oxygens around a given silicon are Si-O-Si bonds or Si-O-Al bonds. Oxygens in silicates and aluminosilicates can also be "non-bridging" oxygens bonded to one silicon and charge compensated by modifier cations such as Na^+. The notation used to describe the silicon environment, Q notation, denotes how many oxygens are bridging oxygens (given by a superscript number) and how many of the bridging oxygens are Si-O-Al (given by a subscript number). For example, Q^4_2 represents a silicon site surrounded by 2 Si-O-Si and two Si-O-Al oxygens, while Q^3_0 represents a site with one non-bridging oxygen and 3 Si-O-Si oxygens. Each of the different Q species has a distinct chemical shift (Figure 7.3). As peak areas are directly proportional to concentration, NMR spectra can provide the Q distribution for a given aluminosilicate, which in turn can be used to calculate the composition of the phase. For example (Figure 7.4), cancrinite, with Si:Al = 1 contains only Si-O-Al bonds (100% Q^4_4 units), while albite, with Si:Al = 3, contains Si-O-Si and Si-O-Al bonds. Of the three silicon in the formula unit $NaAlSi_3O_8$, two are Q^4_1 units and one is a Q^4_2 unit.

The range of aluminum and silicon concentrations reported for tank wastes and the pH range (generally above pH 10) for tanks is illustrated in Figure 7.5 along with ranges of solution compositions tested in the first four sets of experiments. Solutions for all four sets were prepared with Si:Al ratios of 1.1, 2.3, and 11 by varying the relative concentrations of colloidal silica and boehmite added to the suspension (Figure 7.5). Silicon concentrations for Series 1 to 3 were 5.3×10^{-2} M, 7.67×10^{-2} M, and 0.1 M for the solutions with Si:Al = 1.1, 2.3, and 11, respectively. The initial solution pH was adjusted to pH 13.5 (Series 1 and 2) and pH 12.5 (Series 3) using NaOH. Sodium nitrate was added to make the total Na^+ concentration 1 M (Series 1 and 3) or 5 M (Series 2). A fourth series was prepared at pH 13.5 with higher silicon and aluminum concentrations (2.13 M, 2.6 M, and 3.3 M). For Series 1 and 2, solution concentrations were low enough to allow for complete dissolution of the starting

colloidal silica and boehmite particles. For Series 3 and 4, dissolution of boehmite and silica consumed sufficient hydroxide ions to lower the pH. The pH reduction drove solutions to the saturation limit in boehmite and produced large concentrations of polymeric silicates. The effect of the incomplete reaction on the products observed is described below.

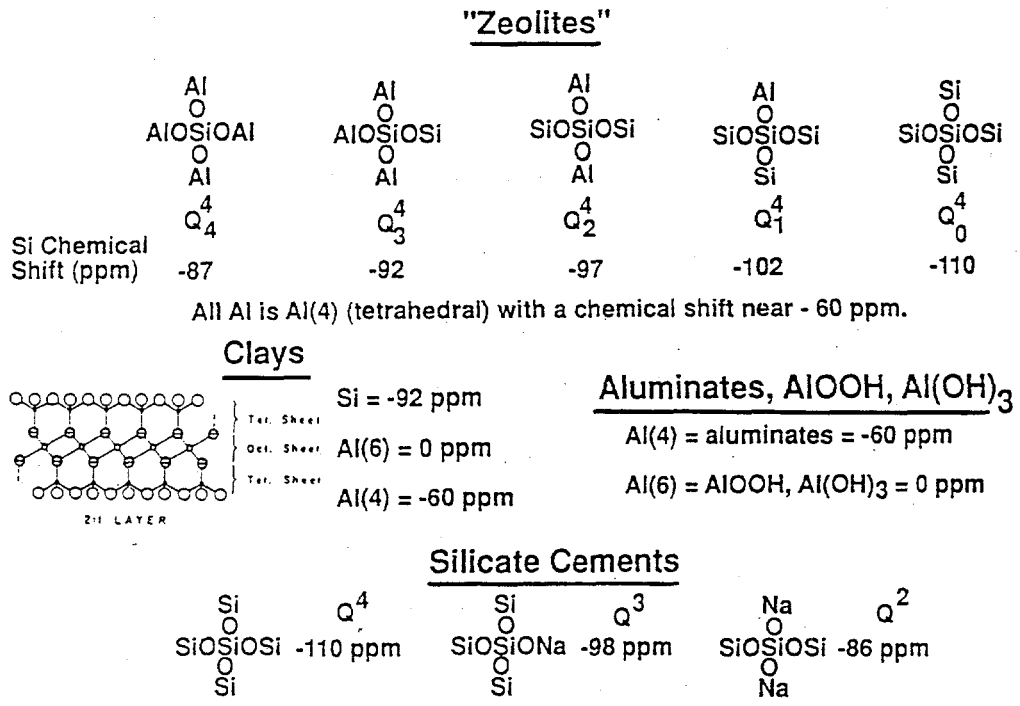

Figure 7.3. Atomic Structures of Aluminosilicates.

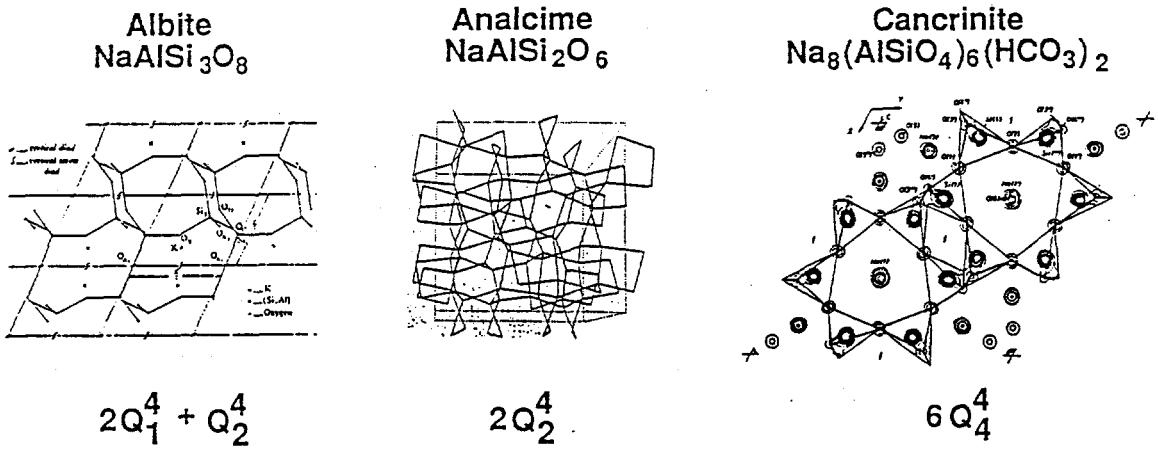

Figure 7.4. Network Aluminosilicates. These aluminosilicates consist of interconnected tetrahedral aluminate and silicate groups. Si NMR can determine the degree of Al substitution and net compositions for amorphous and crystalline aluminosilicates.

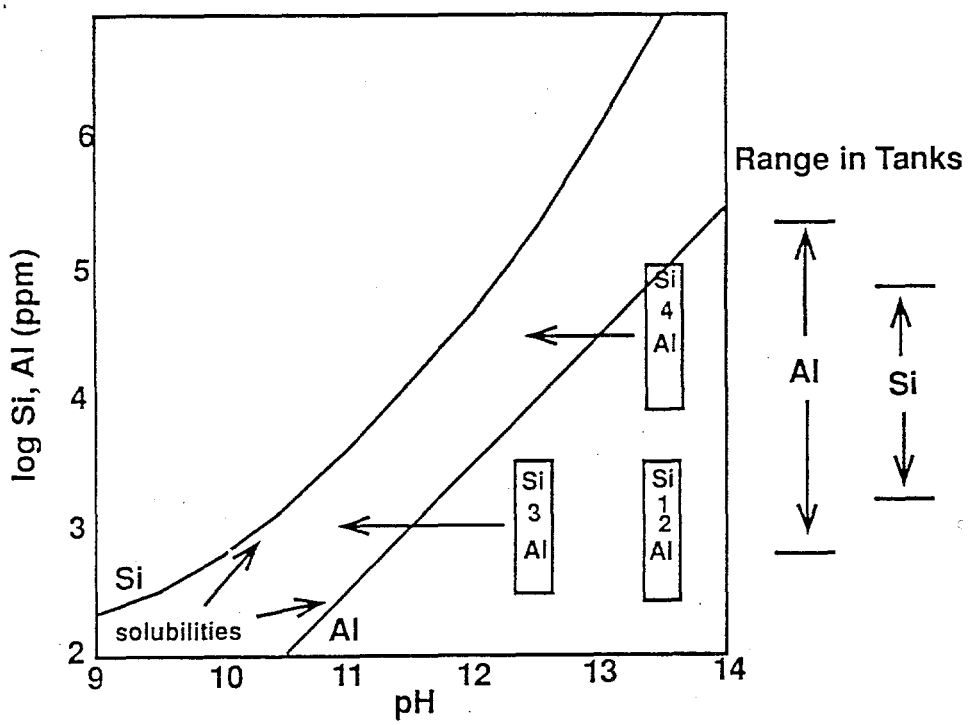

Figure 7.5. Silica and AlOOH Solubility Limits. Concentrations in tank wastes and simulants fall above and below these limits. Samples for NMR analyses (interior boxes) span analyzed compositions for tanks (exterior arrows) and include dilute Si, Al samples at pH 13.5 and both 5 M (1) and 1 M (2) $NaNO_3$; dilute samples at pH 12.5, 1 M $NaNO_3$ (3), and concentrated Si, Al samples at pH 13.5, 9 M $NaNO_3$ (4).

All aluminosilicate solutions corresponding to Series 1 [pH 13.5, 5 M $NaNO_3$, "low" concentration (completely soluble precursors)] produce single-phase cancrinite powders with nearly 100% yield. Solution analyses via inductively coupled plasma emission (ICP) analysis indicate that the aluminum left in solution is at or below detection limits (20 ppm), while the silicon left in solution roughly corresponds to what is expected based on removal of one silicon per aluminum to produce an insoluble solid. Solid-state ^{29}Si NMR spectra of the powders exhibit a single peak at -88 ppm that is identical to the spectrum for cancrinite independent of the Si:Al ratio in the initial solution. The peak position indicates that all silicon in all three samples (Si:Al in solution = 1.1, 2.3, and 11) is present as Q^4_4 units and indicates that the Si:Al ratio in the solid is 1, regardless of the Si:Al in solution. X-ray analyses confirm that single-phase cancrinite is produced.

Lowering the salt content of the solution from the 5 M in Series 1 to the 1 M used in Series 2 has a dramatic effect on the nature of the insoluble aluminosilicate phases produced. Solid-state ^{29}Si NMR spectra of the Series 2 samples (Figure 7.6) indicate that the composition of the precipitate composition is now dependent on the Si:Al ratio in the starting solution. In addition to the Q^4_4 peak seen at -88 ppm, additional peaks are now seen at -92, -97, and -103 ppm corresponding to Q^4_3, Q^4_2, and Q^4_1, respectively. As Si:Al in solution is increased, the population of Si-O-Si bonds in the solid relative to Si-O-Al bonds in the solid also increases as indicated by the change in the Q distribution. The relative areas of the different Q peaks has been used to calculate Si:Al ratios for each of the solid phases

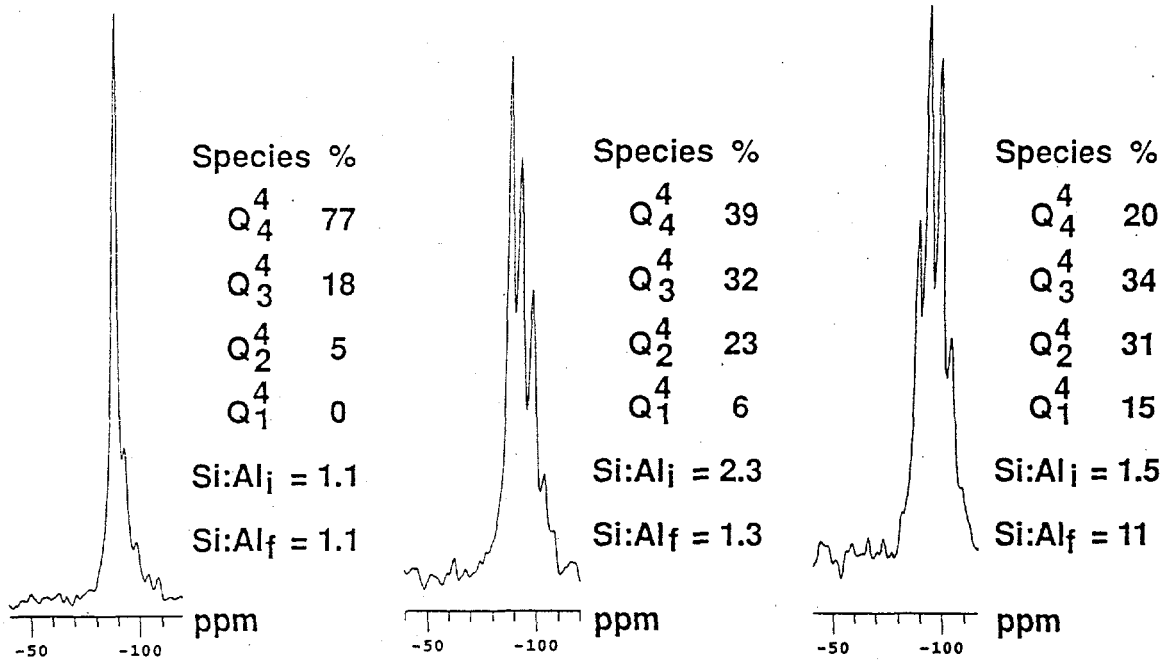

Figure 7.6. Silicon NMR Spectra of Aluminosilicate Crystals. Changing the Si:Al ratio in solution ($Si:Al_i$) changes the atomic structure and composition of aluminosilicate precipitates ($Si:Al_f$).

produced. The NMR results indicate that Si:Al in the zeolitic materials formed corresponds to 1.1, 1.3, and 1.5 for solutions with initial Si:Al = 1.1, 2.3, and 11, respectively. While this range in Si:Al for the solid phases seems somewhat insignificant, the range of compositions described above is sufficient to change the initial dissolution kinetics by a factor of over 1000 (Figure 7.2). A comparison between Series 1 and Series 2 also suggests that the Si:Al ratio in the solid will continue to become more sensitive to Si:Al in solution as the salt content is lowered. Perhaps, at low salt content, Si:Al in the solid may approach that seen in solution for all Si:Al ratios.

Other samples examined to date [Series 3 (pH 12.5, "low" concentration) and Series 4 (pH 13.5, "high concentration")] have not produced pure-phase crystalline solids. Instead, amorphous gel phases form that are transformed into hard, cement-like materials as a function of time. In all cases, consumption of hydroxide via dissolution of the starting silica and boehmite particles lowers the pH to the point where the boehmite no longer dissolves. The resulting solutions contain relatively high concentrations of polymeric species that react with each other to form cement rather than completely reacting with dissolved aluminum species. ^{27}Al NMR spectra show the fraction of boehmite that has dissolved and show that the dissolved aluminum is incorporated into amorphous aluminosilicate phases as tetrahedral aluminum. ^{29}Si spectra show that the amorphous silicate matrix contains large concentrations of non-bridging oxygens in addition to Si-O-Si and Si-O-Al bonds. X-ray analyses reveal the presence of unreacted boehmite, $NaNO_3$, and (for Series 3) cancrinite encapsulated in the amorphous cement. In some instances, the resulting materials was hard enough that a hammer was required to break the samples down for analysis.

A direct comparison between aluminosilicate formation in tank wastes and in the simple solutions reported here is not yet possible. However, the TEM results reported in Section 4.0 suggest that phases similar to the materials reported above are seen in tank sludges. Cancrinite has been observed in B-111 and possibly in BX-107 sludges. Amorphous cement-like material with Si:Al = 2 is also seen in BX-107 sludge. An unknown crystalline aluminosilicate with Si:Al = 1.7 has been seen in T-104 sludge. Composition analyses indicate that all of the above tanks contain lower free silicon concentrations and lower pH values than the samples examined to date via NMR. Based on what has been observed to date, B-111 sludge is predicted to contain cancrinite as the major aluminosilicate. For the other two tanks, the pH is sufficiently low to inhibit gibbsite and boehmite dissolution, resulting in incomplete reaction as is observed. The few known results suggest that the above methodology will be of use in determining the nature of aluminosilicate formation in tank sludges.

7.2 Sedimentation Models

Extensive data have been collected during the past two quarters regarding the sedimentation behavior of single-component systems including boehmite (AlOOH), iron hydroxide [$Fe(OH)_3$], and gibbsite [$Al(OH)_3$]. This quarter, sedimentation models have been developed to describe existing data. The models show great promise for allowing engineers to predict both sedimentation rates and final sediment densities as a function of parameters such as solids loading and the size of the sedimentation container. The general features of the model are provided below with examples of how the model can be used to understand and predict sludge behavior as a function of processing conditions.

Earlier work on sedimentation indicates that two types of sedimentation behavior are observed that correspond to solids loadings above and below the gel point for a given set of agglomerated sludge particles. Below the gel point, each agglomerate acts as an independent unit. Each unit falls at a rate determined by its size and density, resulting in a gradual buildup of sediment from the container bottom and gradual depletion of particles from solution, starting with the largest particles. At the gel point, the aggregates become interconnected throughout the container and form a network that can support a load. However, forces exerted on the gel network, such as applied pressure or the weight of overlying sediment, can deform the network, promoting hindered settling of the entire gel mass. Here, a sharp interface is observed between clear supernatant liquids and a sediment layer which gradually settles. Above the gel point, higher solids loadings result in more interconnected structures and form gels that are more resistant to collapse or deformation.

The rheological property that describes the resistance of the gel network to irreversible deformation is the compressive yield stress, $P_y(\Phi)$. The compressive yield stress is a function of many variables, including the size, shape, composition, and density of the primary particles and agglomerates in the system. However, literature results indicate that the compressive yield stress can be accurately described by the power law expression depicted in Figure 7.7, in which the constant c (which represents how resistant the network is to compression) has units of pressure (psi); Φ is the volume fraction of solids; Φ_g is the volume fraction of solids corresponding to the gel point; and m is a constant that can vary between 4 and 10 but is typically 4 for fractal agglomerates. The parameters for the power law curves may be determined using equilibrium sediment height data obtained from at least three different sediment heights. Such data have been obtained for the suspensions shown in Figure 7.7 and have been used to calculate values for both c and Φ_g.

Sediment Compression Model

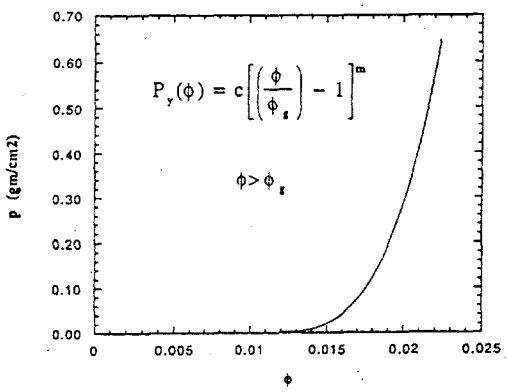

Reference Pressures

Condition	Pressure (psi)
10 cm lab test	0.6 psi
normal filtration	14 psi
10 ft tank sediment	36 psi
centrifugation (20,000 G)	200 psi
pressure filtration	20-5400 psi

Compression Model Results

System	Salt	Gel Point (vol%)	C (psi)	Sediment Density at Pressure P = 0.6 psi	P = 14 psi	P = 36 psi
$Fe(OH)_3$, pH 12	none	0.95%	0.40	4 wt%	13 wt%	16 wt%
" "	1 M	0.64%	0.02	9 wt%	16 wt%	19 wt%
$Al(OH)_3$, pH 13 (1 um)	0.1 M	6.7%	326	21 wt%	26 wt%	29 wt%

Figure 7.7. Sediment Compression Model Results. Gel point and yield stress parameters extracted from power law fit are consistent with known agglomerate interactions.

Compressive yield curves provide practical engineering information regarding sedimentation as well as providing insight into the parameters that control sediment densities. First, the curves can be used to calculate approximate sediment densities as a function of the level of pressure applied to the sediment. Figure 7.7 shows reference pressures for a wide range of different processing or experimental configurations. For typical sedimentation experiments in the lab, where the initial sediment column is 10 cm high, the pressure on the sediment from the weight of the solids in the system is on the order of 0.5 psi. However, in a 1 x 10^6 gal tank, the sediment layer could be over 10 ft tall and result in pressures on the sediment almost 100 times greater. The compressive yield curve shows that the equilibrium sediment densities expected during in-tank processing could be substantially higher than the densities measured in laboratory-scale experiments, e.g., 16 wt% vs. 4 wt% for $Fe(OH)_3$ suspensions. However, laboratory tests performed on limited quantities of actual sludge can provide values for c and Φ_g that allow for calculation of sediment densities for in-tank processing or for other unit operations such as filtration.

The values of the parameters c and Φ_g provide insight into some of the factors that control sludge densities. The gel point, Φ_g, is a reflection of the nature of the fractal agglomerates present in the system. Fractal agglomerates composed of small primary particles will exhibit a lower gel point than sludges containing larger primary particles. Many of the components expected to be present in sludge contain primary particles as small as 10 nm and exhibit gel points that can be below 1 vol% [compared with over 6 vol% for 1 μm $Al(OH)_3$]. Factors promoting agglomeration (such as increased salt) should lead to more open structures and lower gel points as is observed for $Fe(OH)_3$. The constant c relates to how difficult it is to deform a given gel. Again, the trends seen to date in c are consistent with expectations. Networks containing large primary particles have a high gel point, but are more difficult to deform (are not as compressible) as networks containing small primaries. The drop in c from 0.4 psi

to 0.02 psi with increasing salt seen for $Fe(OH)_3$ is consistent with literature results and indicates that adsorbed salts can function as "lubricating" agents between particles. In any case, extraction of values for c and Φ_g from sedimentation experiments can show whether gel formation is being promoted or inhibited and whether processing conditions lead to the formation of particle networks that are easy or difficult to compress.

The compressive yield curves have been incorporated into more elaborate transient sedimentation models that allow the kinetics of sedimentation to be calculated. Figure 7.8 shows that by determining compressive yield curves and agglomerate structures appropriate to describe sedimentation behavior at one solids loading, it is possible to determine sedimentation rates for a wide range of different solids loadings. The models can also be performed as a function of the size of the sedimentation container. Figure 7.9 shows the sedimentation curve calculated for a 4 wt% $Fe(OH)_3$ suspension in a settling tank with an initial sediment height of 10 m. The calculations indicate that sediment levels should drop by 2 m in 1 month, that complete settling could take over 3 months, and that the final sediment density should be about 16 wt% $Fe(OH)_3$. The calculations can be utilized to determine how to control processing parameters to meet processing goals. For example, if complete sedimentation of $Fe(OH)_3$ "sludge" in 1 month is desired, the calculations indicate that the initial solids loading should be lowered from 4 wt% to about 2 wt%.

7.3 Colloidal Mixtures and Agglomeration vs. Processing

Work in previous quarters on single-component simulants has shown that most of the physical properties of interest in sludge processing are controlled by the distribution of agglomerate structures for the insoluble components. Parameters required to characterize the agglomerate structure are the size of the primary particles, which for most sludges ranges from 1 μm to below 10 nm; agglomerate sizes, which for basic sludge suspensions ranges from a minimum of approximately 1 μm to millimeters; and the fractal dimension (related to the density of the colloidal aggregate), which ranges from a low of 1.8 for diffusion-limited aggregates to a maximum about 2.5 for compacted agglomerates. Work in previous quarters addressed how solution conditions such as pH, ionic strength, and shear influence agglomerate structures. In this quarter, the work has progressed to studies of how processing parameters, such as heating and stirring, influence agglomeration. Work also has progressed to studies of two-component particulate systems. As will be shown below, the presence of one particle type can dramatically influence the physical properties of suspensions of another particle type by changing agglomeration behavior. While several mixtures have been studied, the emphasis has been on mixtures of large and small particles (1-μm gibbsite and 50-nm boehmite) of similar surface chemistry, and on mixtures of charged and near-neutral particles {boehmite and apatite [$Ca_5(PO_4)_3OH$]}.

Two examples illustrate how viscosity can be modified in particle mixtures. Boehmite, containing 50-nm primary particles, forms low-density fractal agglomerates that can be highly viscous at low solids loadings. At pH 11 and a shear rate of 115 s^{-1}, viscosities can exceed 3000 cp for an 8 vol% suspension. Suspensions containing 1-μm gibbsite particles exhibit much lower viscosities (47 cp) under the same solution conditions because the larger primary particles form agglomerates that contain more mass per unit volume (and occupy less space at the same solids loading). Based on the properties of the individual components, the addition of small boehmite particles to the larger gibbsite would be expected to increase the viscosity of the gibbsite slurry. Viscosity measurements (Figure 7.10) show that while this expectation is observed at relatively high boehmite concentrations, initial additions of small quantities of boehmite (1 part boehmite to 99 parts gibbsite) are sufficient to lower the slurry

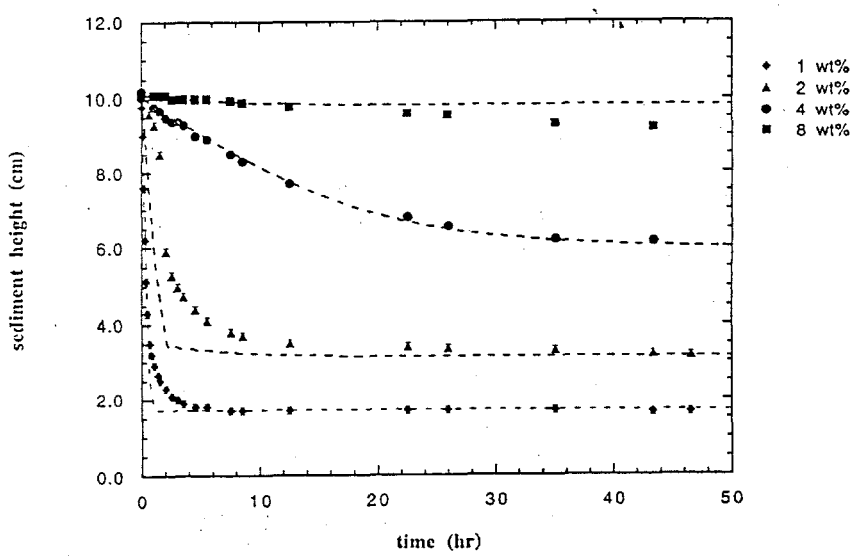

Figure 7.8. Predicted Sedimentation Velocities and Sediment Densities. Sedimentation can be calculated for any solids loading above the gel point. Results can be extrapolated up to full-scale sedimentation in tanks.

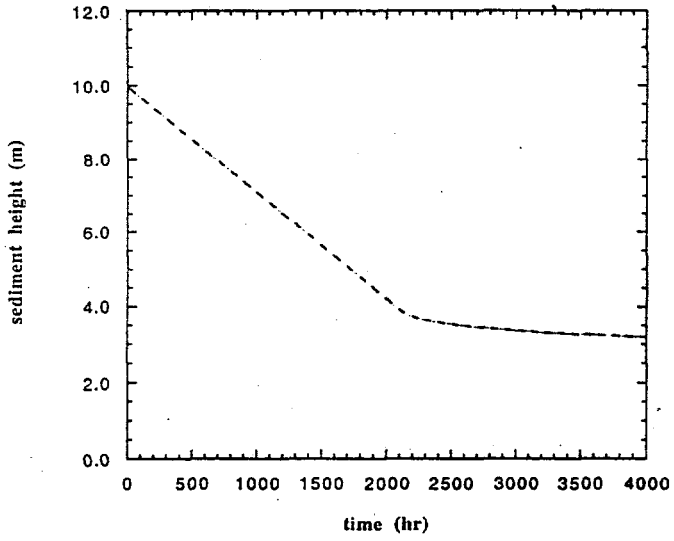

Figure 7.9. Predicted Sedimentation Velocity [4 wt% $Fe(OH)_3$, pH 12]. Calculation indicates that 4 wt% suspension requires 100 days to settle. Lowering initial solids to 2 wt% may provide complete settling in 30 days.

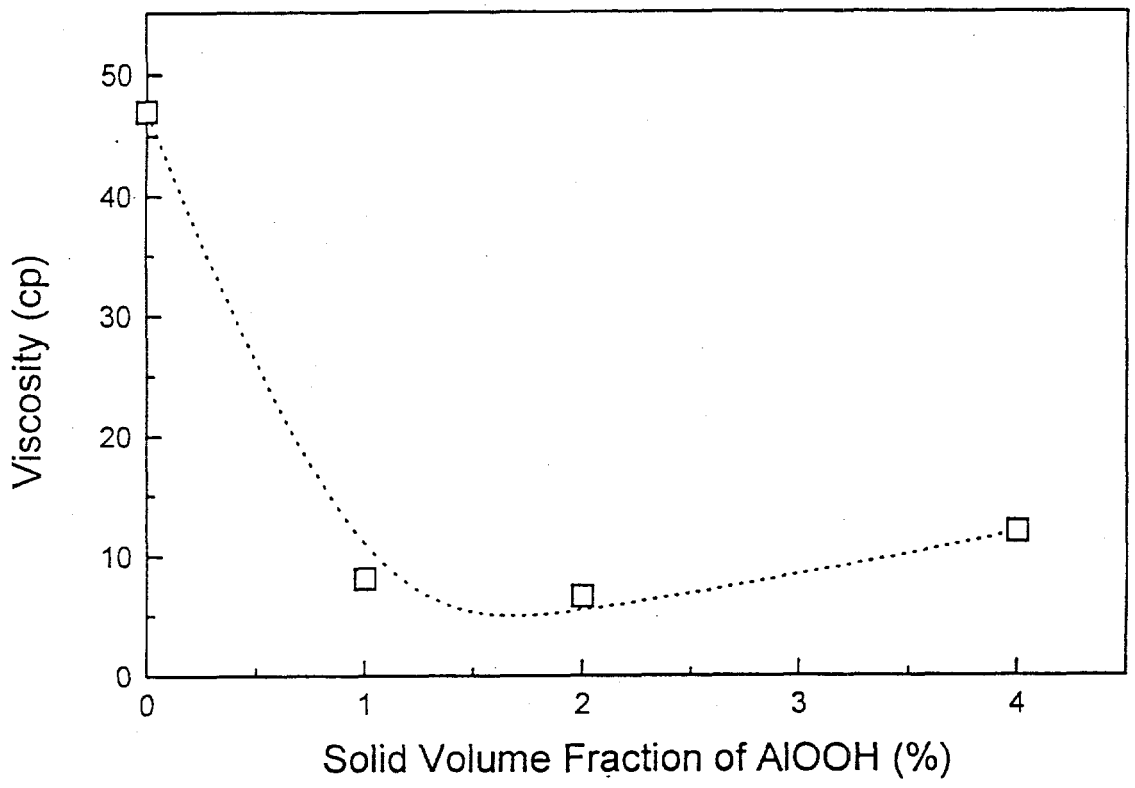

Figure 7.10. Viscosity of 8 vol% Gibbsite (1 μm) as a Function of Solid Volume Fraction of Boehmite at pH 11 with 0.1 M $NaNO_3$ (shear rate = 115 s^{-1})

viscosity by a factor of 4. It appears that at low boehmite concentrations, the boehmite agglomerates provide small particles (see also Figure 7.13) that act as "ball bearings" to disrupt interactions between the larger gibbsite particles.

Surface chemistry, as well as size, appears to influence the viscosity of mixed systems. Addition of 4 wt% apatite (HAP) particles to a suspension of 3 vol% (9 wt%) boehmite decreases the viscosity by about a factor of 4 (Figure 7.11), even though the total solids loading increases from 9 wt% to 13 wt%. Although this work shows that apatite promotes agglomeration of boehmite, it appears that apatite does not stick to boehmite as strongly as boehmite sticks to itself, resulting in less viscous suspensions. (This lowering of interparticle interactions is also apparent in sedimentation results discussed below.)

Sedimentation data on the same mixed particle systems allow us to probe different aspects of the same agglomeration behavior noted in viscosity measurements. Sedimentation studies have been performed to investigate how gibbsite-boehmite mixtures behave after heating and mixing. The work was motivated by concerns about how the simulant S-3 (which is a gibbsite-boehmite mix) might behave during shipping and handling. This simulant is being used for vendor evaluations of the Initial Pretreatment Module. More importantly, most in-tank processing steps, such as washing and leaching,

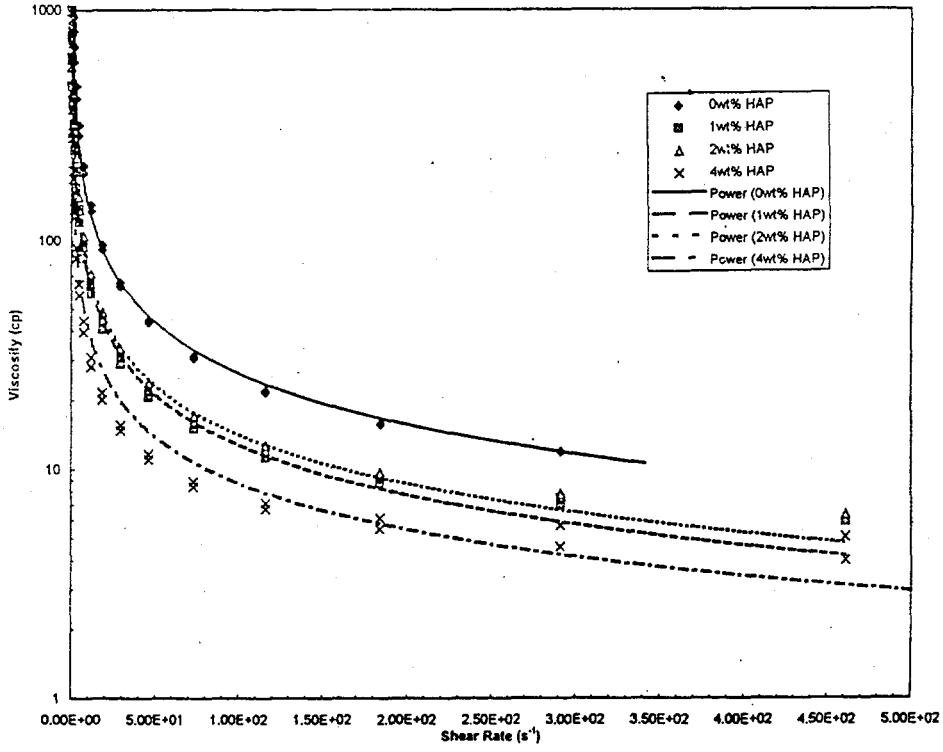

Figure 7.11. Viscosity vs. Shear Rate and $Ca_5(PO_4)_3OH$ (HAP) Concentration for the 3 vol% AlOOH Sample with 0.01 M $NaNO_3$. HAP additions lower viscosities even though total solids loading increases from 9 wt% (AlOOH alone) to 13 wt%.

involve heating to 100°C with agitation. It is important to understand how such processing parameters might influence sedimentation behavior.

At room temperature, pure suspensions of 1-μm gibbsite particles settle to produce sediments with a solids loading as high as 25 wt%. Pure boehmite suspensions exhibit much lower sediment densities (3 wt%) under similar conditions. This behavior is expected based on the small primary particle size (50 nm). At room temperature, boehmite-gibbsite mixtures of 9:1 and 1:9 both exhibit behavior resembling that of gibbsite, with sediment densities of near 20 wt% and 25 wt%, respectively (Figure 7.12). However, on heating (boiling for 3 days), the 9:1 boehmite-gibbsite mixture gels and does not settle at all, while the 1:9 boehmite-gibbsite mix actually settles more rapidly to form a sediment with a density of nearly 40 wt% (Figure 7.12). Similar effects are observed after 3 days of agitation in a shaker, although the effects are less pronounced.

The behavior described can be rationalized by assuming that heating and/or agitation has the net effect of disrupting the original agglomerate structures present in all suspensions (Figure 7.13). If an excess of gibbsite particles is present, most of the small particles generated by agglomerate breakdown are scavenged by the larger gibbsite particles to produce mixed agglomerates in which the large particles are coated by the smaller particles. The new agglomerate structure forms denser sediments because 1) the small particles fill in voids between the large particles, and 2) the small particles make the gibbsite sediment more compressible via the same "ball-bearings" mechanism mentioned in the

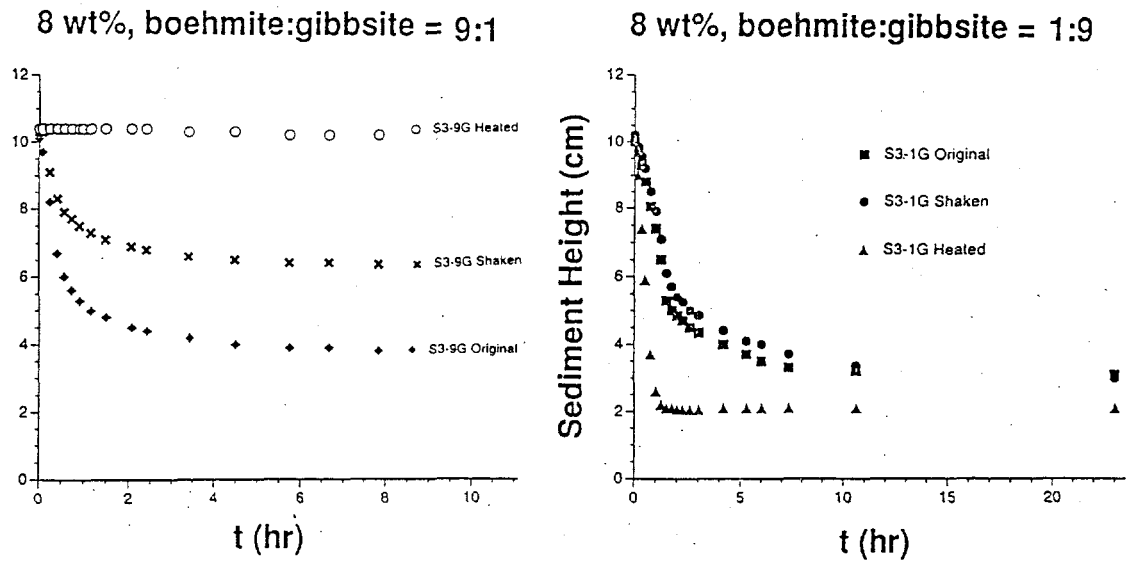

Figure 7.12. Sedimentation Velocity as a Function of Heating and Shaking (8 wt%, Boehmite-to-Gibbsite Ratios of 9:1 and 1:9). When gibbsite predominates, heating promotes sedimentation. When boehmite predominates, heating inhibits sedimentation.

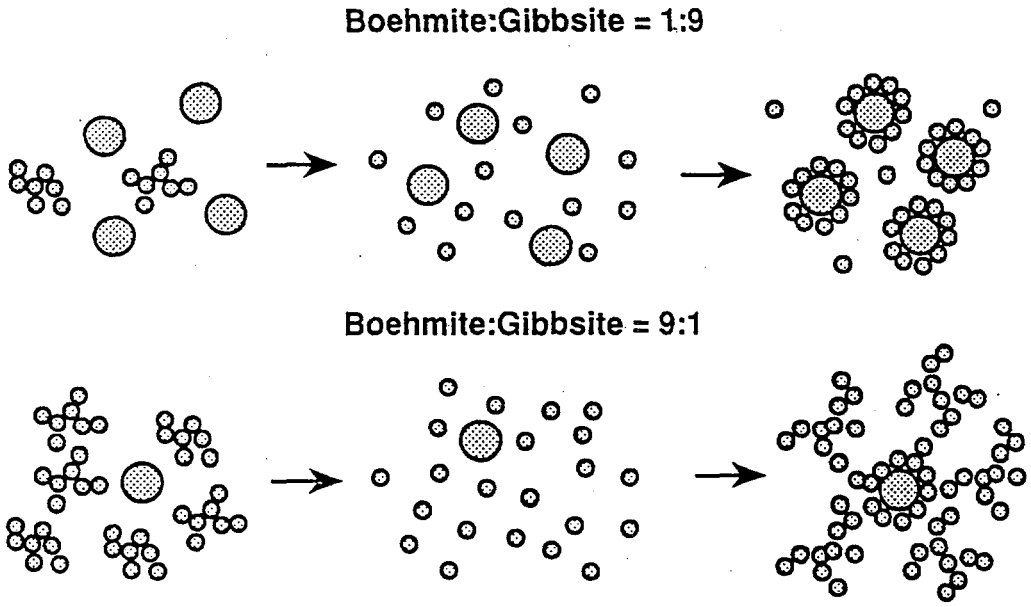

Figure 7.13. Boehmite and Gibbsite Agglomerate Structures (Boehmite-to-Gibbsite Ratios of 1:9 and 9:1)

discussion of viscosity. When an excess of the smaller boehmite is initially present, the initial agglomerates are again broken down. However, there are insufficient large particles to scavenge the small fragments, so the small particles reagglomerate. The resulting sediment occupies more volume (has a lower gel point) because the agglomerates reform to produce agglomerates with a lower fractal dimension (probably around the diffusion-limited aggregation value of 1.8) than were present in the original material (probably near 2.5).

Sedimentation results on boehmite-apatite mixtures mirror property changes observed in viscosity measurements. A 5:1 mixture of boehmite-apatite settles faster than pure boehmite and forms a denser sediment (Figure 7.14). As for the viscosity measurements, the main difference between the two suspension types appears to be that interparticle interactions are weaker with apatite present, resulting in more compressible sediments.

While much of the above discussion on sedimentation is speculative, the general observations that sludges can either expand or contract depending on processing conditions and the mix of particles present in actual sludges must be taken into account to optimize sludge processing. It appears that if small primary particles are present (representative of most actual sludges examined to date), heating will tend to produce a volume expansion. However, it appears that phosphate particles, such as apatite,

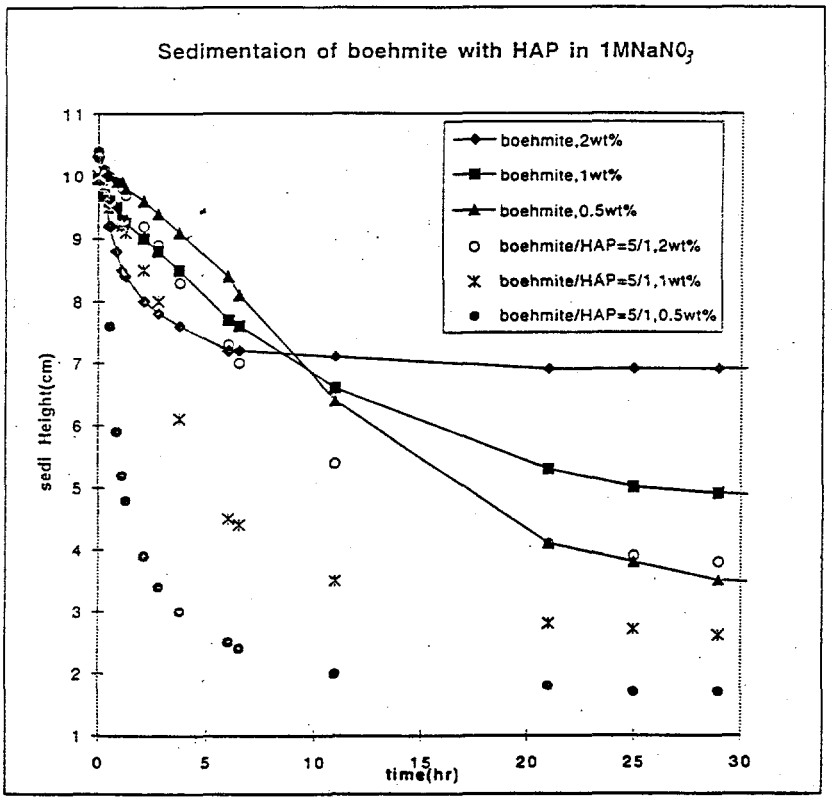

Figure 7.14. Sedimentation of Boehmite with $Ca_5(PO_4)_3OH$ (HAP) in 1 M $NaNO_3$. At high ionic strength, HAP changes agglomerate structures, resulting in enhanced sedimentation rates and denser sediments.

can weaken interparticle networks of oxide or hydroxide particles and result in slurries that will exhibit lower viscosities, higher sedimentation velocities, and higher sediment densities. This result is not only significant in terms of predicting sludge behavior (see Section 7.4), but suggests that addition of low concentrations of certain particle types might represent a processing aid that could be added to problem sludges. However, alternatives to phosphates that do not interfere with subsequent glass formation must be identified for this strategy to be viable.

The final property investigated for mixed suspensions is filtration behavior. There has been speculation that since large primary particles form more permeable filter cakes than agglomerates of fine primary particles, mixtures of large and small primary particles should be easier to filter than fine-particle agglomerates alone. Permeability measurements made on filter cakes of gibbsite-boehmite mixtures (Figure 7.15) show that large particles do not really promote filtration. Addition of even 1 part boehmite to 99 parts gibbsite is sufficient to lower the filter cake permeability by a factor of 3. If more than 10% of the solids present are boehmite (90% gibbsite), the permeability becomes indistinguishable from that of pure boehmite. The results show that the permeability of large and small particles is controlled by the pore distributions generated by the small particles once a sufficient number of small particles are present to fill the voids in the matrix created by the large particles. The only potential advantage of having large particles present might be in cross-flow filtration, where the large particles might assist in scouring filter cakes from filtration media.

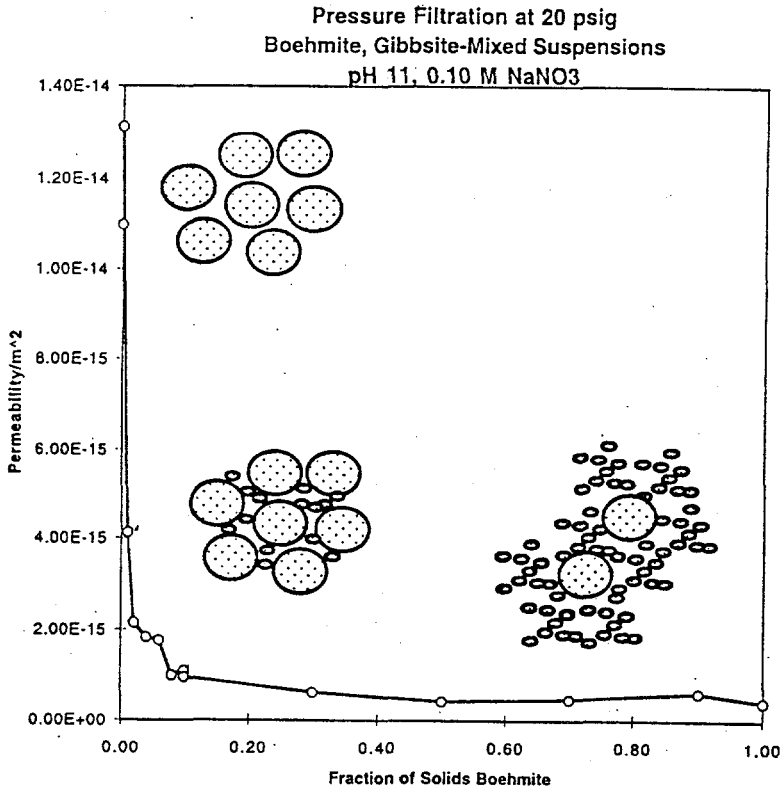

Figure 7.15. Pressure Filtration at 20 psig, Boehmite-Gibbsite Mixed Suspensions at pH 11, 0.1 M $NaNO_3$

7.4 Behavior of Actual Tank Wastes

Recently, sedimentation data were obtained on sludge from Tanks S-104, T-111, BX-107, T-104, and B-111. These data are being used to investigate how these sludges behave under standard washing and leaching procedures. Solutions used in the sedimentation studies correspond to retrieval wash (2.3 wt% solids in 0.01 M NaOH and $NaNO_3$ at 100°C for 1 hr), caustic leaching (8 wt% solids in 3 M NaOH at 100°C for 5 hr), and final washing (8 wt% solids in 0.01 M NaOH and $NaNO_3$ at 25°C for 0.5 hr).

The sedimentation results obtained at 8 wt% solids loadings (for the caustic leach and final wash) are indicative of hindered settling above the gel point for all sludges examined to date. No sedimentation is observed at all for B-111, T-111, and S-104 sludges, while T-104 and BX-107 sludges exhibit slight compaction. At 2.3 wt% (retrieval wash conditions), significant sedimentation is observed for all samples. Observed initial sedimentation velocities range from a maximum of 3.2 cm/hr for T-104 sludge to a minimum of 0.2 cm/hr for S-104 sludge. Final sediment densities range from 3.4 wt% for S-104 to 12 wt% for T-104.

It is interesting to compare the sedimentation results observed for actual tank sludges with the behavior of simple simulants. TEM and elemental analyses show that Tank S-104 sludge consists largely of boehmite. The primary particle size of the boehmite is approximately 0.1 μm, which is only twice as large as the 0.05-μm particles found for the commercial boehmite used in the sedimentation studies. In terms of final sediment density, S-104 sludge is comparable to boehmite under similar sedimentation conditions (3.4 wt% for S-104 compared with 2.9 wt% for commercial boehmite). The slight increase in sediment density for S-104 sludge is consistent with the slightly larger primary particle size. In terms of sedimentation rate, 2 wt% commercial boehmite settles at a rate of about 0.5 cm/hr compared with 0.2 cm/hr for S-104 sludge. Again, the laboratory tests on single-component boehmite come close to replicating the behavior of tank sludges that contain similar particles.

TEM results show that Tanks T-111 and B-111 contain sludges consisting primarily of the bismuth-iron-silicate phase. High resolution images suggest that this phase closely resembles commercial $Fe(OH)_3$ both in terms of its primary particle (sub-μm) and agglomerate distributions. Sediment densities for T-111 and B-111 sludges in laboratory-scale tests of 6.2 wt% and 5.9 wt%, respectively, are close to the equilibrium sediment densities measured for $Fe(OH)_3$ of 6.7 wt%. Initial sedimentation velocities of 2.8 and 1.2 cm/hr for T-111 and B-111 sludges, respectively, are comparable to the value of about 2 cm/hr measured for $Fe(OH)_3$ at 2 wt% solids.

The two tank wastes that exhibit the highest sediment densities and most rapid sedimentation rates observed to date are T-104 and BX-107. The retrieval wash sediments exhibit densities of 11.5 wt% and 9.5 wt%, respectively, and sedimentation rates of 2 to 3 cm/hr. Both wastes contain bismuth-iron-silicate as the major phase, and both tanks also contain significant concentrations of aluminum phosphate (30% to 40%). It may be that the near-neutral phosphates in these sludges are promoting agglomeration in the same way that apatite promotes agglomeration of boehmite in the two-component laboratory experiments. In any case, it appears that tests performed on simple simulants can be used to help predict and rationalize the behavior of tank sludges if the simulants contain particles that are similar, in terms of primary particle and agglomerate structures, to particles identified in tank sludges.

Distribution

No. of Copies

Offsite

Dennis Wynne
EM-361, Trevion II
U.S. Department of Energy
12800 Middlebrook Road
Germantown, MD 20874

Robert King
Washington Department of Ecology
P.O. Box 47600
Olympia, WA 98594-7600

Donald Temer
Los Alamos National Laboratory
P.O. Box 1663
MS: G740
Los Alamos, NM 87545

Steven Agnew
Los Alamos National Laboratory
P.O. Box 1663
MS: J586
Los Alamos, NM 87545

Phil McGinnis
Oak Ridge National Laboratory
P.O. Box 2008
Oak Ridge, TN 37831-6273

Zane Egan
Oak Ridge National Laboratory
P.O. Box 2008
Oak Ridge, TN 37831-6273

Samuel D. Fink
Bldg. 773-A Rm. B-112
Westinghouse Savannah River Company
P.O. Box 616
Aiken, SC 29802

No. of Copies

Denis Strachan
Argonne National Laboratory
9700 S. Cass Avenue
Argonne, Il 60439

Ed Beahm
Oak Ridge National Laboratory
P.O. Box 2008
Oak Ridge, TN 37831-6223

Steve Conradson
Los Alamos National Laboratory
P.O. Box 1663
MS: D429
Los Alamos, NM 87545

Onsite

3 **DOE Richland Operations Office**

S. T. Burnum
P. E. Lamont
C. S. Louie

15 **Westinghouse Hanford Company**

J. N. Appel
H. Babad
G. R. Bloom
A. L. Boldt
S. J. Eberlein
K. A. Gasper
M. J. Kupfer
S. L. Lambert
G. T. MacLean
R. M. Orme
I. E. Reep
D. A. Reynolds
B. C. Simpson
J. P. Sloughter
D. J. Washenfelder

56 **Pacific Northwest Laboratory**

G. S. Anderson
E. G. Baker
D.L. Blanchard
K. P. Brooks
P. J. Bruinsma
B. C. Bunker
N. G. Colton (5)
J. L. Cox
J. Craig Hutton
T. H. Dunning
A. R. Felmy
S. R. Gano
R. L. Gordon
G. L. Graff
N. J. Hess
L. K. Holton (5)
E. A. Jenne
D. E. Kurath
J. P. LaFemina (5)
M. M. Lamoureux
J. Liu
G. J. Lumetta
R. K. Quinn
B. M. Rapko
D. R. Rector
B. A. Reynolds
R. D. Scheele
L. J. Sealock, Jr.
G. J. Sevigny
P. A. Smith
L. Song
D. L. Styris
L. E. Thomas
J. M. Tingey
A. J. Villegas
M. J. Wagner
Y. Wang
Information Release (7)